

## REPORT DOCUMENTATION PAGE

The public reporting burden for this collection of information is estimated to average 1 hour per response, including the time for reviewing instructions, searching existing data sources, gathering and maintaining the data needed, and completing and reviewing the collection of information. Send comments regarding this burden estimate or any other aspect of this collection of information, including suggestions for reducing the burden, to the Department of Defense, Executive Service and Communications Directorate (0704-0188). Respondents should be aware that notwithstanding any other provision of law, no person shall be subject to any penalty for failing to comply with a collection of information if it does not display a currently valid OMB control number.

PLEASE DO NOT RETURN YOUR FORM TO THE ABOVE ORGANIZATION.

1. REPORT DATE (DD-MM-YYYY) 20-01-2010		2. REPORT TYPE Final Performance Report		3. DATES COVERED (From - To) 1 November, 2006 - 31 October, 2009	
4. TITLE AND SUBTITLE Research Studies on Electromagnetically Induced Transparency				5a. CONTRACT NUMBER FA9550-07-1-0009	
				5b. GRANT NUMBER	
				5c. PROGRAM ELEMENT NUMBER	
6. AUTHOR(S) S. E. Harris				5d. PROJECT NUMBER	
				5a. TASK NUMBER	
				5f. WORK UNIT NUMBER	
7. PERFORMING ORGANIZATION NAME(S) AND ADDRESS(ES) Leland Stanford Junior University 651 Serra Street Stanford, CA 94305-6215				8. PERFORMING ORGANIZATION REPORT NUMBER	
9. SPONSORING/MONITORING AGENCY NAME(S) AND ADDRESS(ES) AF Office of Scientific Research (AFOSR) 875 North Randolph Street Arlington, VA 22203-1768				10. SPONSOR/MONITOR'S ACRONYM(S)	
				11. SPONSOR/MONITOR'S REPORT NUMBER(S)	
12. DISTRIBUTION/AVAILABILITY STATEMENT Unlimited.					
13. SUPPLEMENTARY NOTES					
<div style="text-align: right; font-size: 2em; font-weight: bold;">20100303211</div>					
14. ABSTRACT The overall theme of this work has been the development and utilization of new sources of radiation that produce time energy entangled biphotons that are both much longer and much shorter than those that now exist. We have learned to produce biphotons with temporal lengths greater than 500 ns and linewidths smaller than the natural linewidth of target atoms. We have demonstrated the use of telecommunication light modulators to modulate single photons and also a novel technique for measuring the temporal length of biphoton wave packets. The technique is based on the use of synchronously driven fast modulators and slow detectors. By measuring the coincidence count rate between single photon counting modules as a function of the sinusoidal modulation frequency we obtain the Fourier transform of the biphoton wave function. Accomplishments in the area of ultra-short biphotons include the suggestion for using the method of chirp and compress at the single photon level, and the first demonstration of resonance sum frequency generation with paired photons. We have demonstrated a new quantum effect that we term as nonlocal modulation were phase modulators at distant locations, acting on the photons of an entangled pair, interfere to determine the apparent depth of modulation.					
15. SUBJECT TERMS electromagnetically induced transparency, photon interactions with atoms, nonclassical states of the electromagnetic field, including entangled photon states, quantum engineering and measurements, parametric down conversion and production of entangled photons.					
16. SECURITY CLASSIFICATION OF:			17. LIMITATION OF ABSTRACT	18. NUMBER OF PAGES 93	19a. NAME OF RESPONSIBLE PERSON
a. REPORT	b. ABSTRACT	c. THIS PAGE			19b. TELEPHONE NUMBER (Include area code)

**Final Performance Report**

**RESEARCH STUDIES ON ELECTROMAGNETICALLY INDUCED  
TRANSPARENCY**

**Grant AFOSR FA9550-07-1-0009**

**Prepared for**

**AIR FORCE OFFICE OF SCIENTIFIC RESEARCH  
and  
ARMY RESEARCH OFFICE**

**For the Period**

**November 1, 2007 to October 31, 2009**

**Submitted by**

**S. E. Harris<sup>1</sup>, Principal Investigator**

**Edward L. Ginzton Laboratory  
Stanford University**

<sup>1</sup>seharris@stanford.edu

# Contents

1	EXECUTIVE SUMMARY	2
2	Subnatural Linewidth Biphoton Generation with 2-D MOT	5
3	Theory of EIT- based Paired Photon Generation	10
4	Electro-Optic Modulation of Single Photons	11
5	Modulation and Measurement of Time-Energy Entangled Photons	16
6	Resonator Sum Frequency Generation with Time- Energy Entangled Photons	22
7	Observation of Nonlocal Modulation with Entangled Photons	29
8	Chirp and Compress with Biphotons	37
9	Nonlinear Optics at X-Ray Wavelengths	43
10	Joint Support	53
	APPENDIX	54
A	Publications During Grant Period	54
B	Chirped Crystal Simulation Code	56
C	Chapter 4 of Kolchin's Dissertation	64

# 1 EXECUTIVE SUMMARY

Our work during this contract period began with emphasis on electromagnetically induced transparency, slow light, and its application to making ultra-long biphotons. As the program evolved, we increased emphasis on novel techniques to produce, measure, and utilize both long and short biphotons.

We begin by summarizing the key property of time-energy entangled biphotons. This is: if an observer at point A chooses to measure the frequency of an arriving photon he will then know to high accuracy the frequency of the photon which will be measured by an observer at point B. But instead, if the observer at point A chooses to measure the time of arrival of a photon at his location, he will then know, again to high accuracy, the time of arrival of the photon at point B. The accuracy of these measurements is not limited by the Heisenberg uncertainty principle.

We turn next to what is meant by long and short. Typical biphotons as generated by nonlinear optical crystals have temporal lengths in the range of between 0.1 ps and 10 ps. Such photons are not resolvable by presently existing photo detectors. These detectors, measure whether or not a photon is present, but may not be used to examine the functional form of the photonic wave packet.

By using the techniques of slow light and working under AFOSR-ARO and DARPA support, in 2005 our group demonstrated the first method of generating temporally long biphotons. The length of these photons is controlled by the group delay in the nonlinear

media and in early experiments resulted in photons with a length of about 40 ns. A key accomplishment of the present program was the extension of this length to photons whose length could be continuously varied from 50 to 900 ns. Of importance, the line width of these photons was less than the natural linewidth of the rubidium vapor that was used to produce them. This is important because optical nonlinearities when produced using electromagnetically induced transparency continue to increase in the subnatural linewidth regime and in the absence of dephasing may be made arbitrarily large. This should soon allow the demonstration of nonlinear optics with single photons.

We mention a surprise that occurred during this work. In the course of observing long biphotons with a length determined by the slow optical group velocities, we found that the photonic wave packets had a sharp leading edge spike on their front edge. Following a suggestion by Dan Gauthier we recognized that this front edge spike is a Sommerfeld-Brillouin precursor. This observation is important because it clarifies, for both slow light and fast light, that information will always be transmitted at the speed of light in vacuum.

In January 2008 we recognized that we had the capability to modulate single photons for the first time. To do this we used the Stokes photon of a biphoton pair to set the time origin for electro-optic modulation of the wave function of the anti-stokes photon. With the time origin determined, the modulator could arbitrarily modulate either the amplitude or phase of the anti-stokes photon. The technique therefore provides the technology for studying the response of atoms to shaped single-photon waveforms on a time scale comparable to the natural linewidth of target atoms.

The next step in our work in modulating biphotons was the development of a method for measuring their length using slow detectors. The essential idea is that modulation in the time domain followed by slow integration constitutes a Fourier transformation. The experimental technique is to measure the coincidence count rate between single photon counting modules as a function of an applied sinusoidal frequency. The inverse Fourier transform of the data then yields the biphoton waveform. Though this experiment was a proof of principle experiment, ultimately it could be used to measure wavepacket profile of biphotons when sufficiently fast photo detectors are not available.



We are now working on an important extension of our work on modulating single photons. This is the application of spread spectrum techniques at the single photon level. Spread spectrum is well known in the communications industry as a technique for avoiding interference and jamming, and at times increasing information capacity. Our work is the first demonstration of this technique to single photons.

We turn next to our work on short biphotons. Our first contribution was a PRL entitled Chirp and Compress : Toward Single-Cycle Biphotons. In this work we described a method for generating time-energy entangled photons with a spectral width that exceeds an octave, and of compressing their spectrum to produce biphotons whose temporal length is a single optical cycle. The elements of the technique are the suggestion for using parametric down conversion in a periodically poled material to spontaneously generate pairs of entangled photons whose instantaneous frequencies are chirped in opposite directions and the use of the non-local nature of entangled photons to allow the dispersion, as experienced by one photon, to cancel out the dispersion of the second photon and to compress the biphoton wave packet.

Our first experimental work in this area was the development of a novel resonant sum frequency generation technique (PRL February 2009). This work demonstrates a rather amazing effect where we take two single photons that each have a broad spectral linewidth and sum them. We find that though each photon has a broad linewidth, the linewidth of the sum frequency photon is as narrow as that of the pumping laser. Also, the output (sum) power is linear rather than quadratic in input power. These effects both derive from the quantum behavior of single photons.

In the course of studying nonlocal dispersion compensation as described above, we recognized that there should be a new quantum effect that we have termed as nonlocal modulation. Assume that single and idler photons pass through sinusoidal phase modulators located at different locations. These modulators are driven at the same modulation frequency and are connected by cable such that their relative phase may be varied. After passing through the modulators the single and idler photons are dispersed, for example by a prism, and the relative positions of the single and idler photons are correlated. We find : When the

modulators are run with the same phase the modulation depths add; when they are run in phase opposition the modulation depths subtract. Two distant modulators with the same modulation depth and opposite phase therefore have the same frequency correlation as when both modulators are absent. This effect is entirely quantum mechanical. Mathematically it results because, quantum mechanically, one adds probability amplitudes before squaring, while classically one squares before adding.

As this contract ends, we are beginning work in the area on nonlinear and quantum optics at x-ray wavelengths. To a great extent we are motivated by the new 1.5 Angstrom free electron laser that is now operating at Stanford. We anticipate experiments to demonstrate frequency doubling of this laser with the further objective of using SHG as a correlator and diagnostic for the laser itself.

## 2 Subnatural Linewidth Biphoton Generation with 2-D MOT

The most significant experimental advance in cold atom EIT research project during performance period is that we observed subnatural linewidth biphotons with our MOT generation II, which is our new platform for biphoton generation in a series of modulation studies at single photon level. Figure 1 shows both experimental configuration (geometry) and mechanism of parametric paired-photon generation. In contrast to previous MOT constructed in early grant period (W911NF-04-1-0105), the new 2-D  $^{85}\text{Rb}$  MOT has a cigar shaped atom cloud ( $\sim 1.7$  cm long and an aspect ratio of 25) and consequently a large optical depth in the

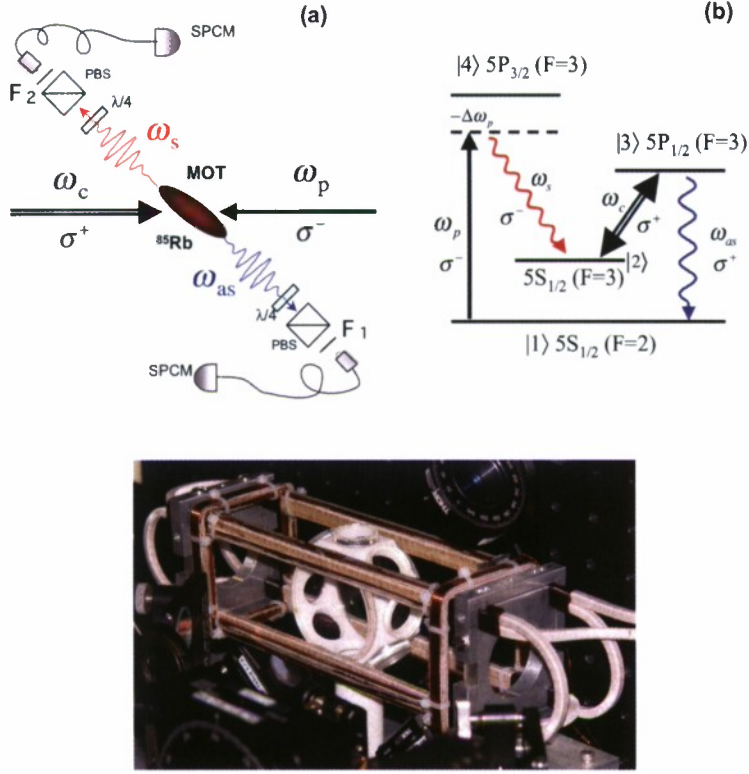


Figure 1: **Upper:** Biphoton generation in a double- $\Lambda$  system. (a) Experimental configuration.  $F_1$  and  $F_2$  are narrow-band optical frequency filters. (b)  $^{85}\text{Rb}$  energy level diagram. In the presence of counter-propagating pump ( $\omega_p$ ) and coupling ( $\omega_c$ ) beams, Stokes ( $\omega_s$ ) and anti-Stokes, ( $\omega_{as}$ ) photons are generated into opposing single-mode fibers. **Lower:** 2-D MOT apparatus. The vacuum cell is 6 cm size ceramic structured octagon. The cell is located in the middle of water cooled trapping coil(racetrack-shaped cage).

longitudinal direction; moreover, its cylindrical quadrupole trapping field results in minimal longitudinal magnetic field gradient and hence greatly reduces the inhomogeneous Zeeman broadening of the m-states of the  $5S_{1/2}$  level. The experimental cycle comprises 4.5 ms of trapping time and 0.5 ms paired photon generation window. At the end of the trapping cycle, the rubidium cloud is prepared in  $5S_{1/2}$  level by turning off the repumping laser 0.3 ms before turning off the trapping laser; counter-propagating, circularly polarized, cw pump ( $\omega_p$ ) and coupling ( $\omega_c$ ) lasers are subsequently turned on and phase-matched, paired Stokes ( $\omega_s$ ) and anti-Stokes ( $\omega_{as}$ ) photons are spontaneously generated and propagate in opposite directions as shown in the figure.



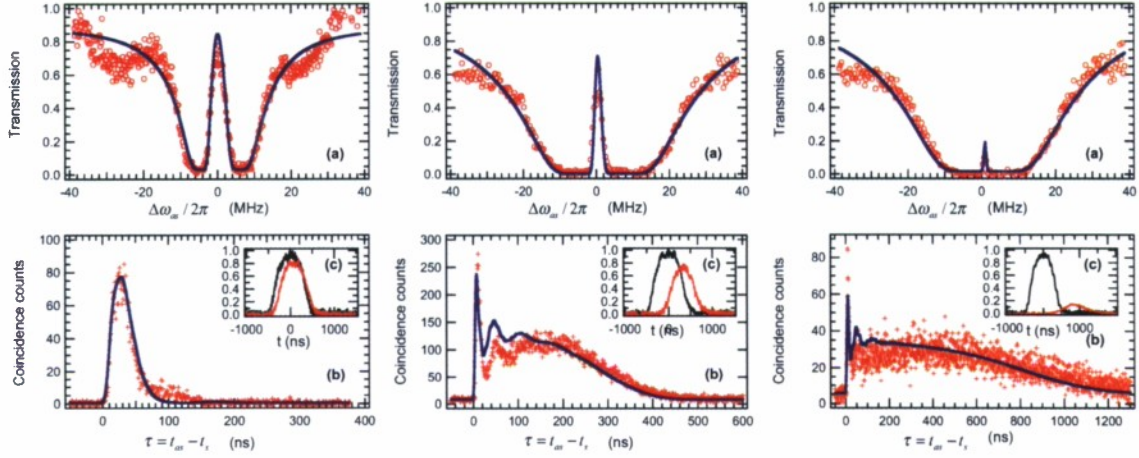


Figure 2: Biphoton wave packet data for three slow group delay cases. The upper row plots are anti-Stokes EIT scan data( $\circ$ ) and EIT fit(blue curve), the lower row plots are paired-photon coincidence count data( $+$ ) and predicted wave packet shape with time bin width of 1 ns for 800 s(lower row). Propagation delay of anti-Stokes pulse(red traces in inserts of lower row plots) are also presented for three slow group delay( $\tau_g$ ) cases. Experimental parameters are: **Left:** ( $\tau_g \sim 50\text{ ns}$ )  $\text{OD}=7$ ,  $\Omega_c = 4.20\gamma_{13}$ ,  $\Omega_p = 1.16\gamma_{13}$ , and  $\Delta_p = 48.67\gamma_{13}$ . **Middle:** ( $\tau_g \sim 320\text{ ns}$ )  $\text{OD}=53$ ,  $\Omega_c = 4.20\gamma_{13}$ ,  $\Omega_p = 1.16\gamma_{13}$ , and  $\Delta_p = 48.67\gamma_{13}$ . **Right:** ( $\tau_g \sim 900\text{ ns}$ )  $\text{OD}=53$ ,  $\Omega_c = 2.35\gamma_{13}$ ,  $\Omega_p = 1.16\gamma_{13}$ , and  $\Delta_p = 48.67\gamma_{13}$ .

The optical depth of the 2-D  $^{85}\text{Rb}$  MOT can be varied up to 62, which gives us enough parameter space to verify the relation between the optical group delay and the length of the biphoton waveform. Figure 2 shows sets of anti-Stokes EIT scan and paired-photon coincidence counts for three anti-Stokes EIT group delay cases, which is controlled by varying the optical depth and the coupling laser power( $\tau_g \simeq (2\gamma_{13}/|\Omega_c|^2)N\sigma L$ , where  $N\sigma L$  is the optical depth and  $\gamma_{13}$  is the dephasing rate of level  $|3\rangle$ ). The trapping laser used for these experimental runs has a power of 160 mW, a beam diameter of 2 cm, and is red detuned by 20 MHz from the  $|5S_{1/2}, F=3\rangle \rightarrow |5P_{3/2}, F=4\rangle$  transition. A repumping laser is locked to the  $|5S_{1/2}, F=2\rangle \rightarrow |5P_{3/2}, F=2\rangle$  transition, has a power of 80 mW, and overlaps one of six trapping beams. The pump laser is circularly polarized ( $\sigma^-$ ), has a  $1/e^2$  diameter of 1.46 mm, and is blue detuned from the  $|1\rangle \rightarrow |4\rangle$  transition by 146 MHz, i.e.  $\Delta_p = 48.67\gamma_{13}$ . The coupling laser is circularly polarized ( $\sigma^+$ ), has a  $1/e^2$  beam diameter of 1.63 mm and is on resonance with the  $|2\rangle \rightarrow |3\rangle$  transition. The counter-propagating pump and coupling

beams are collinear and set at a 2 degree angle from the longitudinal axis of the MOT. The Stokes ( $\sigma^-$ ) and anti-Stokes ( $\sigma^+$ ) photons are coupled into opposing single mode fibers after passage through  $\lambda/4$  wave plates and polarization beam splitters (PBS). The Stokes and anti-Stokes fiber coupling efficiency is 70% and the  $1/e^2$  waist diameter of their foci is 220  $\mu m$ .

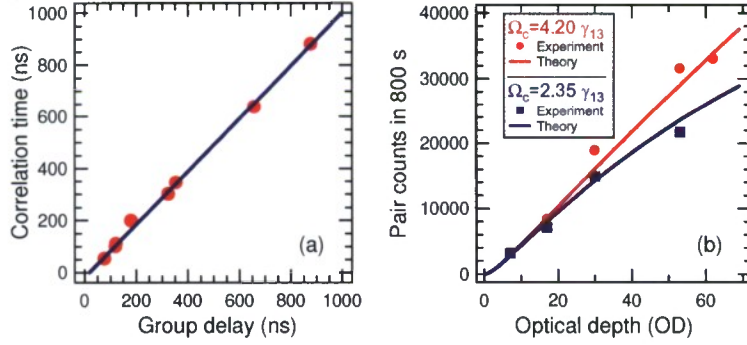


Figure 3: (a) Measured correlation time vs measured anti-Stokes group delay. The solid line is a linear least squares fit. (b) Paired counts in a 1 ns bin in 800 s as a function of the optical depth.

As shown in Fig. 2, the temporal length of biphoton wavepacket generated in high OD case are much longer (by more than one order) than previously reported in our phase I research. It also means that the generated biphoton has much narrowed bandwidth. The predicted biphoton packet waveforms in lower row plots of Fig. 2 are computed with all parameters obtained from the EIT measurements and vertically scaled to fit the experimental data. The calculated biphoton linewidths are 9.66, 2.36 and 0.75 MHz respectively. These linewidths are comparable to the measured EIT bandwidths and in the latter two cases are less than the 6 MHz natural linewidth of Rb D line. Thanks to the 2-D MOT, which is designed to have increase in OD and decreases in dephasing, the biphoton generation now is in the linear group delay regime where  $\tau_g > \tau_r$  and the correlation width directly follows group delay time as shown in data plot of Fig. 3(a).

Having taken into account the filter and etalon transmissions, the fiber to fiber coupling efficiency, the detector quantum efficiencies and the duty cycle. for the conditions of Fig. 2, we observe a total of 3213, 31674, and 22000 paired counts in 800 seconds, which correspond

to generation rates of 1275, 12569, and 8730 pair/s, respectively. Higher generation rates can be achieved by increasing the pump laser power. With  $\Omega_p = 6.88\gamma_{13}$ , the paired photon generation rates are  $4.0 \times 10^4$  and  $9.0 \times 10^4$  pair/s at OD=17 and 30, respectively. Figure 3(b) shows that the number of paired counts varies linearly with the optical depth. Though the generation rate per spectral bandwidth varies as the square of the optical depth, the bandwidth reduces linearly with this depth leading to the linear dependence. Experimentally, under optimum conditions, we observe 74% of the Stokes photons to be paired. We also observe that all of the correlation data violate the Cauchy-Schwarz inequality by as much as a factor of 11600.

It is noticeable that there is a sharp peak at the leading edge of the correlation data generated for high optical depth case as shown in lower plots in middle and right column of Fig. 2. This feature is Sommerfeld-Brillouin precursor type as in the case for propagating classical wave packets. The physical picture is the following: the detectors register biphoton coincidence counts versus the time  $\tau = t_{as} - t_s$ ; the earliest portion of the biphoton wave packet comes from the high frequency portion of the spectrum, which is not in the range of large group delay, and is thought of as the Sommerfeld precursor. At slightly later times the low frequency Brillouin components arrive at the detector and beat with the simultaneously arriving high frequency components. Though precursors are now understood in the optical region and have even been observed long ago with correlated gamma-ray photons, our work reports the first observation of precursors as measured by single photon correlation.

The 2D MOT we have developed is likely to allow immediate improvements in single photon read-write techniques, in EIT-based quantum memory, and in nonlinear optics with cold atoms. Each of these areas requires the same ingredients as demonstrated here; i.e., low dephasing rate, subnatural linewidth, and high optical depth. For example, the efficiency of a nonlinear process continues to improve as the photon linewidth is reduced below the natural linewidth, and is ultimately limited by the dephasing rate of the non-allowed transition.

For more details please see: 1) Shengwang Du, Pavel Kolchin, Chinmay Belthangady, G. Y. Yin, and S. E. Harris, "Subnatural Linewidth Biphotons with Controllable Temporal Length," *Phys. Rev. Lett.* **100**, 183603 (May, 2008); 2) Shengwang Du, Pavel Kolchin,

Chinmay Belthangady, G. Y. Yin, and S. E. Harris, "Observation of Optical Precursors at the Biphoton Level," *Optics Letters* **33**, 2149 (September, 2008).

### 3 Theory of EIT- based Paired Photon Generation

Our theoretical model is highlighted on paired photon generation in the double-lambda atomic system. We first reexamine the conditions required for the system to operate in the group delay regime. We find that the optical depth of the atomic system has to be sufficiently high in order to avoid the filtering of the generation bandwidth of paired photons by the transparency window. Second, we have extended the theoretical treatment beyond the ground state approximation. This allows us to properly include and analyze the effect of Langevin noise fluctuation on the atomic system and solve the problem of its return to the ground state after the emission of Stokes and anti-Stokes photon pairs. We also addressed the important questions: 1) "What are the effects of the optical thickness of the atomic sample on paired and single photon generation?" 2) "Does every Stokes photon have its paired anti-Stokes photon?"

With low parametric gain and high optical depth we show that the system can produce highly correlated photon pairs. The shape of the intensity correlation function and the emission bandwidth depend on the coupling laser Rabi frequency and the optical depth of the atomic sample. Compared to SPDC, paired photon generation in the double-lambda atomic system is affected by Raman gain in the Stokes channel and EIT in the anti-Stokes channel. EIT, through the absorption at the poles, cuts the emission bandwidth. In order to enter a regime where the EIT window is sufficiently large and therefore the emission bandwidth is controlled to a large extent by the phase-matching process in the presence of large group delay, the optical depth of the atomic sample has to be larger than 10. High optical depth



substantially reduces the influence of Langevin noise fluctuations and Raman scattering on paired photon generation so that the Stokes and anti-Stokes photons are generated mostly in pairs. We therefore suggest the use of a cigar shaped atomic cloud with high optical depth in the longitudinal direction.

For more details please see: P. Kolchin, “Electromagnetically-Induced-Transparency-Based Paired Photon Generation,” Phys. Rev. A 75, 033814 (March 2007). Kolchin’s dissertation chapter 4 “Theory of EIT based Paired Photon Generation” is included in this report as Appendix C.

## 4 Electro-Optic Modulation of Single Photons

We have demonstrated conditional shaping of single photon waveforms using electro-optic modulators. We use the Stokes photon of a biphoton pair to set the time origin for electro-optic modulation of the wave function of the anti-Stokes photon. This technique allows arbitrary control of both phase and amplitude of single photons. A key requirement for this modulation scheme is that the temporal length of biphoton wavepacket, which is represented by correlation time in experiment, is much longer than modulation response time designed for experiment. The subnatural linewidth biphoton source described in the previous section producing biphotons with correlation times adjustable in the 50-900 ns range is ideally suited for this application. Our single photon counting modules (about 350 ps of timing resolution) and data system has fast enough temporal resolution to observe AM modulation in this work.

Figure 4 shows the schematic of the experiment. We use counterpropagating cw pump and coupling lasers to generate time-energy entangled pairs of Stokes and anti-Stokes photons which propagate in opposite directions and are collected into single mode fibers as described



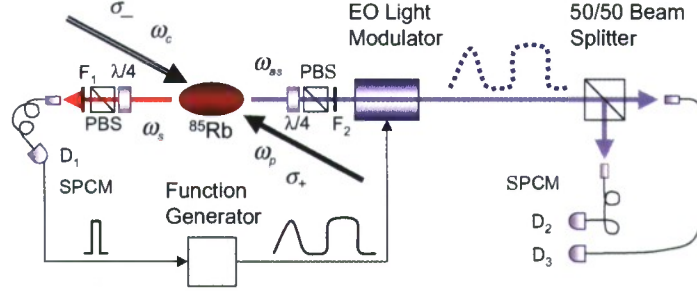


Figure 4: Schematic of paired photon generation and conditional modulation. A Stokes photon detected by an SPCM sets the time origin for shaping the anti-Stokes photon with an electro-optic modulator. To within the accuracy of the SPCM, this allows shaping of both the amplitude and phase of the anti-Stokes photon.

in section A. The detection of the Stokes photon at D1 sets the time origin for firing the function generator that drives the electro-optic modulator which in turn modulates the anti-Stokes photon. Verification of the single photon nature of the modulated anti-Stokes photon is done using a 50-50 beam splitter and detectors D2 and D3. Their coincidence data  $G_{23}^{(2)}(\tau)$  is expected to show a dip at  $\tau = 0$  proving nonclassical nature of modulated anti-Stokes signal.

The electro-optic amplitude modulator consists of phase modulators in both arms of a Mach-Zehnder (MZ) interferometer. The degree of phase control in both arms depends on the type of the modulator. We use a z-cut modulator that requires  $V_\pi = 1.75$  volts to cause the  $\pi$  phase shift required to go from minimum to maximum transmission and can be operated at a maximum frequency of 10 GHz. One port of the output beam splitter of the MZ interferometer is terminated so that the portion of the photon wave function that is not transmitted is lost. In general, if a Stokes photon is detected at time  $t_1$ , and the modulator is activated conditioned on this detection then, in the Heisenberg picture, the anti-Stokes operator at the output of the modulator is related to the input operator by  $\hat{a}_{out}(t_2) = \int g(t_2, t'_2) \hat{a}_{in}(t'_2) dt'_2$ . If there are no dispersive elements, then to within an unimportant phase factor we may write  $\hat{a}_{out}(t_2) = m(\tau) \hat{a}_{in}(t_2)$ . The correlation function in the presence of the modulator is related to that in the absence of the modulator by

$$G_m^{(2)}(\tau) = |m(\tau)|^2 G^{(2)}(\tau) \quad (4.1)$$

With the biphoton wavefunction given by  $\Psi(t_1, t_1 + \tau)$  the modulated (conditional) single photon wavefunction is  $m(\tau)\Psi(t_1, t_1 + \tau)$ . We adjust the bias voltage at the input of modulator so that the output of the modulator  $m(\tau)$  is related to the input voltage  $V(\tau)$  by  $m(\tau) = \sin[\phi(\tau)] \exp[i\alpha\phi(\tau)]$ , where  $\phi(\tau) = \pi V(\tau)/(2V_\pi)$ , and  $\alpha$  is a phase modulation parameter. For a z-cut amplitude modulator as used here  $\alpha = 0.75$ , but may be eliminated by using an x-cut modulator.

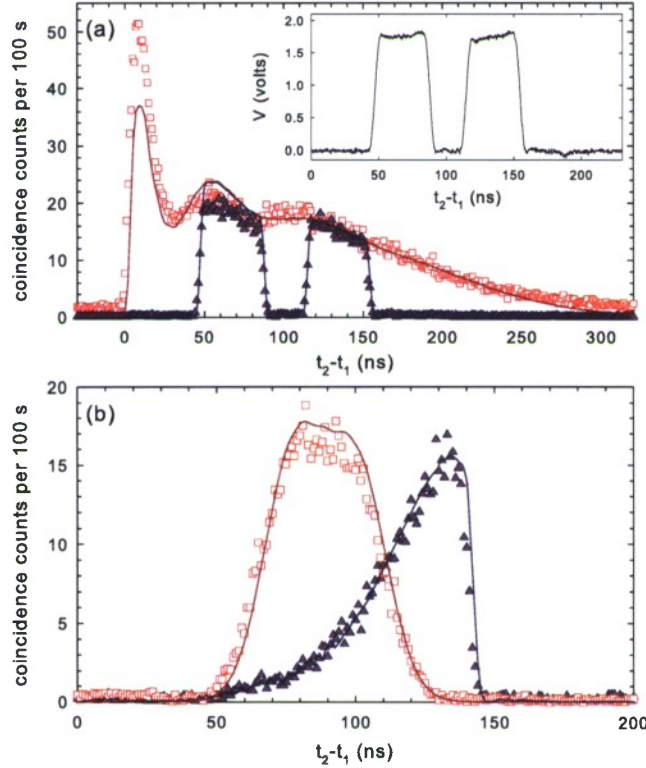


Figure 5:  $D_1$ - $D_2$  coincidence counts in a 1 ns bin as a function of the delay between Stokes and anti-Stokes photons. (a) Modulated ( $\blacktriangle$ ) and unmodulated ( $\square$ ) waveforms. (b) Waveforms with Gaussian ( $\square$ ) and rising exponential ( $\blacktriangle$ ) shapes. The experimental data ( $\square$ ,  $\blacktriangle$ ) were collected over 2000 s. The solid curves for cases (a) and (b) are plotted from theory. The inset in part (a) is the scope trace of the output voltage of the function generator.

The principal experimental results of this work are shown in Figure 5. In part (a), the modulation signal, shown as an inset, is a set of two square pulses. Of importance, there is no vertical scaling between the modulated and non-modulated waveforms. In Fig. 5(b), we show photons modulated with two different waveforms. In the first case the modulator

is driven with a gaussian pulse. In the second case we design the function generator output so as to compensate for the nonlinear distortion of the modulator in such a way that the output of the modulator is an exact rising exponential.

We define the retrieval efficiency,  $\mathcal{E}_R$  of a paired photon source as the probability to generate a single anti-Stokes photon on the condition that its paired Stokes photon is detected. For the non-modulated photon we measure  $\mathcal{E}_R = 3.5\%$ . When losses at the beamsplitter, modulator, filters, fiber to fiber coupling and detector efficiency are backed out, this corresponds to a retrieval efficiency of 55%. For the modulated photons the measured retrieval efficiencies of the two square pulses, the rising exponential and gaussian waveforms are  $\mathcal{E}_R = 1.3\%, 0.61\%$  and  $0.9\%$  respectively. With losses backed out these efficiencies are 21%, 9.4% and 11.2% respectively.

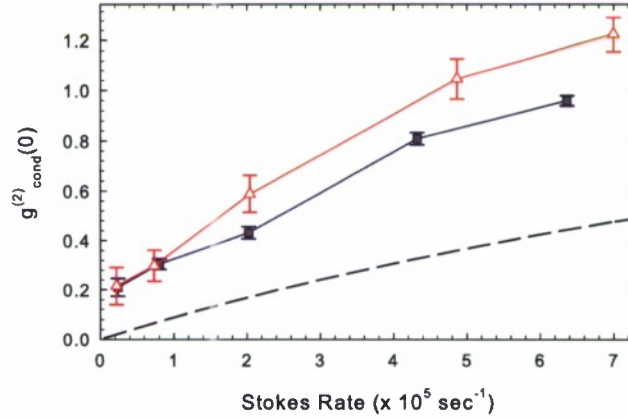


Figure 6: (color online) Conditional three-fold correlation function  $g_{\text{cond}}^{(2)}(0)$  as a function of the Stokes rate for unmodulated ( $\square$ ) and modulated ( $\triangle$ ) single-photon generation. The dashed curve shows the theoretical limit for  $g_{\text{cond}}^{(2)}(0)$  in the absence of excess light scattering (see text).

Since single photons incident on a beamsplitter must go into one output port or the other, in the ideal case where there are no two-photon events and there is no excess scattered light, we would expect no three-fold coincidences at the detectors. A measure of the quality of heralded single photons that quantifies suppression of two photon events is given by the

conditional correlation function:

$$g_{cond}^{(2)}(0) = \frac{N_{123}N_1}{N_{12}N_{13}}. \quad (4.2)$$

Here  $N_1$  is the number of the Stokes counts at  $D_1$ ,  $N_{12}$ , and  $N_{13}$  are the number of two-fold coincidence counts within a time window  $T_c$  at detectors  $D_1, D_2$  and  $D_1, D_3$ ; and  $N_{123}$  is the number of three-fold coincidence counts within this same time window.

In Figure 6 triangles and squares show measured  $g_{cond}^{(2)}(0)$  versus Stokes rate with and without modulation. The modulation is done with the same signal as in Fig. 5(a). We set  $T_c$  equal to the nominal length of the unmodulated biphoton (285 ns). At a Stokes rate of  $2.2 \times 10^4 \text{ sec}^{-1}$  which corresponds to  $\Omega_p = 0.26 \Gamma_3$ , we obtain  $g_{cond}^{(2)}(0) = 0.2 \pm 0.04$  and  $g_{cond}^{(2)}(0) = 0.21 \pm 0.07$  for the unmodulated and modulated waveforms respectively. The fact that the measured  $g_{cond}^{(2)}(0)$  is less than 0.5, (the limiting value for a two photon Fock state), is indicative of the near-single photon character of the light source.

Because there is a small probability for the parametric down conversion process to generate multiple pairs of biphotons, even in the absence of spurious light scattering, the conditional correlation function is not zero. The dashed curve In Fig. 6 shows the theoretical prediction for the conditional correlation function that results from such multiple scattering events. Because of light scattering from both the pump and coupling lasers, the experimental curves lie above this limiting value.

We perform two control experiments: In the first we remove the 30 m long optical fiber so as to modulate the uncorrelated background noise in the tail of the correlation function. Here, we measure  $g_{cond}^{(2)}(0) = 1.2$ . In the second experiment we apply modulation at random times, using an external 10 MHz digital signal as a trigger for the function generator. As expected, we observe a reduced rate of paired counts and no change in the shape of the correlation function.

The method demonstrated in this work might be used to optimally load a single photon into an optical cavity, or instead, to study the transient response of atoms to different single photon waveforms. In the context of light-matter interfaces, it may improve the efficiency of storage and retrieval of single photons in atomic ensembles. For quantum information



applications, both amplitude and phase modulators could be used to allow full control over the single photon waveforms. For example, one could construct a single photon waveform that is a train of identical pulses with information encoded into the relative phase difference between consecutive pulses. The importance of the electro-optic method is its speed and ability to modulate phase as well as amplitude. The technique provides the technology for studying the response of atoms to shaped single photon waveforms on a time-scale comparable to the natural linewidth.

For more details please see: P. Kolchin, Chinmay Belthangady, Shengwang Du, G.Y. Yin, and S.E. Harris, “Electro-Optic Modulation of Single Photons,” *Phys. Rev. Lett.* **101**, 103601 (September, 2008).

## 5 Modulation and Measurement of Time-Energy Entangled Photons

In 2008 we reported the demonstration of conditional temporal shaping of single photon waveforms using electro-optic modulators. In this report, we extend this work to the modulation of biphotons. A highlight is the invention and first experimental demonstration of a Fourier technique that allows the measurement of fast biphotons using slow detectors. Figure 1 shows (a) the schematic of our proof-of-principle experiment and (b) the laser/rubidium-atom interaction diagram for paired photon generation. Parametrically down-converted spontaneous signal and idler photons, or as in the experiment of this work, Stokes and anti-Stokes photons, are incident on synchronously driven sinusoidal amplitude modulators. Without any modulation, in general, the setup will directly yield the Glauber correlation function  $G^{(2)}(\tau)$ , where  $\tau$  is the relative arrival time of the signal and idler photons, with its time resolution limited by the speed of photon detector (SPCM) and TDC system. As shown below, our



new method, by adding AM photon modulation, will give temporal biphoton correlation measurement with time resolution beyond the SPCM-TDC limit.

When amplitude modulators  $m_1(t)$  and  $m_2(t)$  are introduced between the down conversion source and the detectors, the modulated correlation function is then written as

$$G_M^{(2)}(t, t + \tau) = |m_1(t)|^2 |m_2(t + \tau)|^2 G_0^{(2)}(\tau) \quad (5.1)$$

where the subscripts  $M$  and  $0$  indicate cases of modulation on or off. In real experiments, photons arrive at a random time  $t$  which is averaged out over the data collection period  $T$ :

$$\begin{aligned} \overline{G_M^{(2)}(\tau)} &= \mathcal{M}(\tau) G_0^{(2)}(\tau), \\ \mathcal{M}(\tau) &= \frac{1}{T} \int_0^T |m_1(t)|^2 |m_2(t + \tau)|^2 dt, \end{aligned} \quad (5.2)$$

where  $\mathcal{M}(\tau)$  is the intensity correlation function of the modulators in the signal and idler channels. If both channels are modulated by sinusoidal amplitude modulators with frequency  $\omega$  and a common phase  $\varphi$ , that is by modulators  $m_1(t) = m_2(t) = \cos(\omega t + \varphi)$ , then, irrespective of this phase,  $\mathcal{M}(\tau) = 1/4 + 1/8 \cos(2\omega\tau)$ .

If the detectors are slow in the sense that they integrate over the length of the biphoton wave packet, but short as compared to the inverse rate of biphoton generation, the measurement becomes an integral

$$\int_0^\infty \overline{G_M^{(2)}(\tau, \omega)} d\tau = 1/8 \int_0^\infty [2 + \cos(2\omega\tau)] G_0^{(2)}(\tau) d\tau. \quad (5.3)$$

We neglect the DC term and normalize to obtain the Fourier cosine transform pair

$$\begin{aligned} F(2\omega) &= \sqrt{\frac{2}{\pi}} \int_0^\infty G_0^{(2)}(\tau) \cos(2\omega\tau) d\tau, \\ G_0^{(2)}(\tau) &= \sqrt{\frac{2}{\pi}} \int_0^\infty F(2\omega) \cos(2\omega\tau) d\omega. \end{aligned} \quad (5.4)$$

In the measurement procedure,  $F(2\omega)$  is the measured coincidence count rate between low speed single photon counting modules (SPCMs) as a function of the sinusoidal modulation frequency  $\omega$ . The slow detection system (SPCM+TDC) means that hardware integrates signals over  $\tau$ , which is the relative arrival time of the signal and idler photons. We then

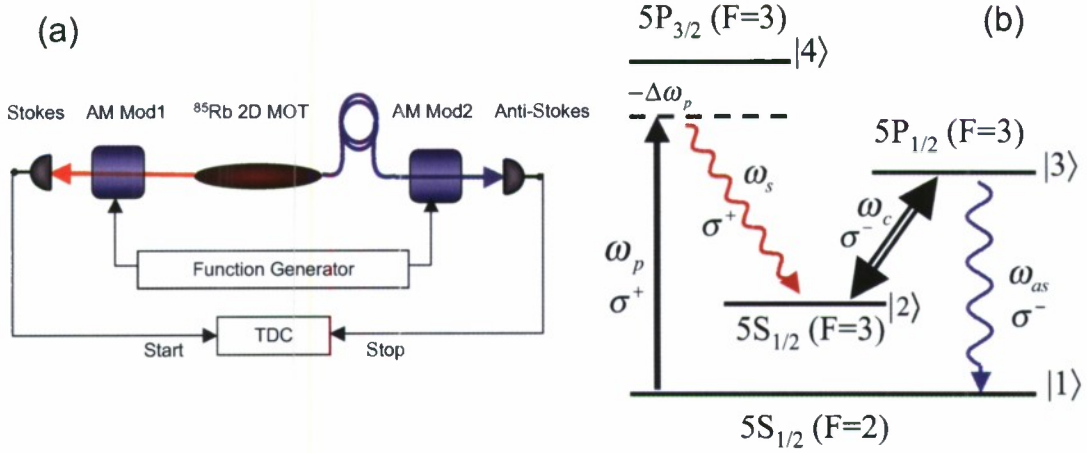


Figure 7: (a) Schematic of experiment. Long biphotons are generated in the cold-atom Rb cell. Using an optical fiber, the anti-Stokes photon is delayed by 175 ns, and the photons are modulated by synchronously-driven sinusoidal modulators before correlation detection with a time-to-digital converter. (b) Energy level diagram for paired photon generation in Rb.

apply the above inverse Fourier cosine transform to yield the Glauber correlation function  $G_0^{(2)}(\tau)$  and therefore the square of the absolute value of the biphoton wavefunction.

Our experiment makes use of long biphotons that are produced using the techniques of electromagnetically induced transparency and slow light. The use of long biphotons allows us to compare the correlation function measured by our Fourier transform technique with a direct measurement using fast detectors and a TDC. The experimental configuration is shown in Fig. 7(a). Paired photons are generated with cold Rb atoms using the method of Balic et al. We apply strong counterpropagating pump and coupling lasers (not shown) to produce phase matched counter-propagating pairs of time-energy entangled Stokes and anti-Stokes photons. We use a  $^{85}\text{Rb}$  two-dimensional magneto-optic trap with an optical depth which can be varied between 10 to 60 to generate biphotons with temporal lengths between 50 and 900 ns. The inset in Fig. 8(a) shows the biphoton wavefunction obtained at an optical depth of 35 as directly measured using a TDC. Two features are of interest. First, the width of the wavefunction is determined by the slow group velocity of the anti-Stokes photon and varies linearly with the optical depth. Second, the distinctive sharp feature at the leading edge is a Sommerfeld-Brillouin precursor that ensures that the earliest signal reaches a detector at the speed of light in vacuum.

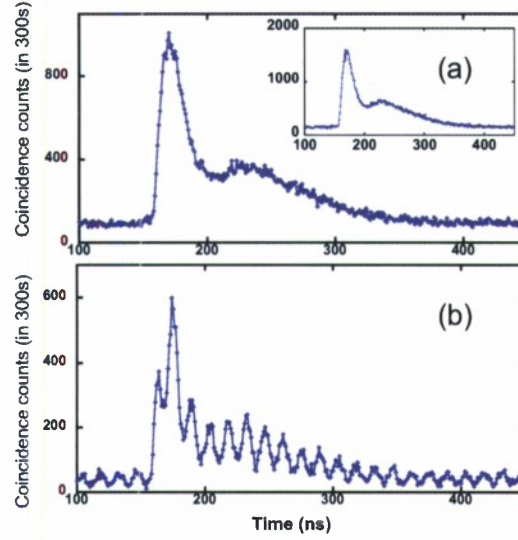


Figure 8: (color online) Modulation of the biphoton correlation function. (a)  $m_1(t) = 1$  and  $m_2(t) = \cos(\omega t + \varphi)$ . The inset in (a) shows the correlation function with both modulators open. (b)  $m_1(t) = m_2(t) = \cos(\omega t + \varphi)$ . Here  $\omega = 2\pi \times 35 \times 10^6$ .

The generated Stokes and anti-Stokes photons are transmitted through 10 GHz electro-optic amplitude modulators (Eospace Inc.) with a half-wave voltage,  $V_\pi$  of 1.3V. To obtain a perfectly sinusoidal output, the modulators are biased at maximum transmission and the input voltage is varied linearly using a triangular waveform that varies between  $-V_\pi$  and  $+V_\pi$ . This waveform is generated by a fast function generator (Tektronics AFG3252) with two output channels whose frequencies and phases can be varied independently. The modulated photons are then sent to SPCMs (Perkin Elmer SPCM-AQR-13), which are connected to the start and stop inputs of a TDC (Fast-Comtec TDC 7886S). Coincidence counts are binned into histograms and plotted as a function of the time difference between the detection of a Stokes and an anti-Stokes photon.

In Fig. 8 (color online) we demonstrate the modulation of a biphoton wavefunction. The data are recoded by binning coincidence counts versus time into 1 ns bins. In Fig. 8(a), the Stokes modulator is turned off and is biased at maximum transmission; and the anti-Stokes modulator is driven at 35 MHz. In agreement with theory, the biphoton wavefunction is not modulated. In Fig. 8(b), both modulators are modulated at 35 MHz with the same, but arbitrary, phase. The correlation function is now modulated at twice the applied frequency, i.e.

at 70 MHz. When driven by non-sinusoidal waveforms, the correlation function is modulated by the cross-correlation of the two modulating signals. In agreement with Eq. (5.2), we have verified that when the two modulating signals are square waves with the same frequency, the correlation function is modulated by a triangular function.

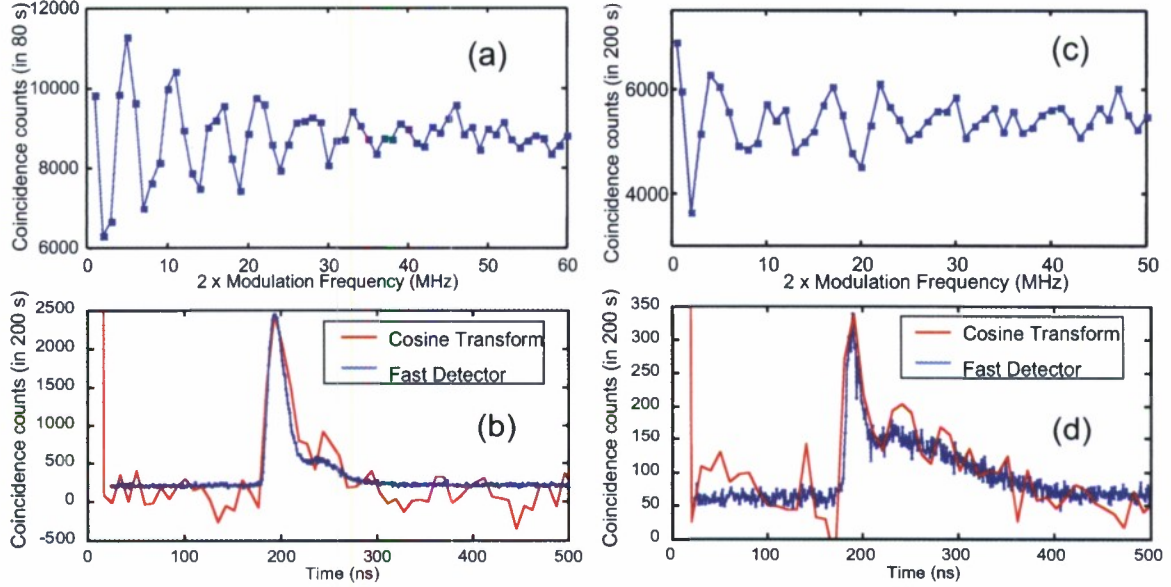


Figure 9: Fourier Transform measurement technique at an optical depth of 15(Left) and 35(Right). **Upper:** Frequency domain data, **Lower:** Fourier Cosine transforms (red) of corresponding frequency domain data, and real-time fast direct temporal correlation data (blue). The term modulation frequency on the x-axis of (a) and (c) refers to the applied frequency. The observed modulation frequency [Eq. (5.4)] is a factor of 2 higher.

We next demonstrate the Fourier measurement technique. A 35 m long polarization-maintaining fiber is used to delay the anti-Stokes photon by 175 ns in the experiment. The modulators are driven synchronously at frequencies between 0 and 30 MHz. To simulate slow detectors, we bin coincidences into  $1 \mu\text{s}$  bins, and since the temporal extent of the waveform is less than  $1 \mu\text{s}$ , the entire biphoton is contained within the first time bin. From the Fourier transform property that delay in the time domain corresponds to oscillation in the frequency domain, the plot of coincidence counts versus modulation frequency shows ripples with a frequency (5.7 MHz) equal to the inverse of the time delay. We show two



data sets in Fig. 9 for optical depth of 15 (left) and 35 (right), for relatively short and long biphoton wave packets, respectively. In Figs. 9(b) and (d), we compare the biphoton wavefunction as directly measured with 1 ns bins (blue line) to the Fourier cosine transform of the traces in Figs. 9(a) and (c), (red line), vertically scaled to match the peak value. We find reasonable agreement between the two methods. We note that the sharp spike in the temporal trace near  $t = 0$  results from the DC component in the frequency domain trace.

We have shown how biphotons may be modulated, and how this modulation may be used to measure the magnitude of the biphoton wavefunction. Though we have used long biphotons and low modulation frequencies, we believe that this technique should be extendable to short biphotons. A commercially available telecommunication modulator driven at a frequency of 60 GHz and therefore modulating at 120 GHz will allow measurement of biphotons with a minimum length of about 8 picoseconds. This is about a factor of five faster than state-of-the-art commercial SPCMs. If the comparison is made on the basis of state-of-the-art polymer light modulators operating at 200 GHz and therefore modulating at 400 GHz, then the Fourier technique, will allow measurement down to about 2.5 ps. This is about eight times faster than the fastest reported superconducting detector. Looking further to the future, all-optical light modulators have been demonstrated at frequencies greater than 1 THz; thereby in principle allowing measurement of photons on femtosecond time scales. We note that an advantage of the Fourier technique as compared to either sum frequency correlation or Hong-Ou-Mandel interference is that the signal and idler photons may be correlated at distant detectors and do not need to be brought together at a summing crystal or at a beam splitter.

For more details please see: Chinmay Belthangady, Shengwang Du, Chih-Sung Chuu, G.Y. Yin, and S.E. Harris, “Modulation and measurement of time-energy entangled photons”, *Phys. Rev. A, Rapid Communications*, **80**, 031803 (September 2009).



## 6 Resonator Sum Frequency Generation with Time-Energy Entangled Photons

We recently developed a technique for enhancing the quantum component of sum frequency radiation that is obtained by summing pairs of signal and idler photons. By resonating the sum frequency we observe generation that varies linearly with input power and is increased by a factor of twelve. The essence of the technique is similar to the Purcell effect where the work done by a generated dipole moment, in this case monochromatic, against an electric field at its own frequency is increased by the presence of the resonator. Of importance, this resonance enhancement occurs pair by pair, thus resulting in the linear dependence of generated sum power on the incident biphoton rate.

The technique of resonant enhancement is shown in Fig. 10. Time-energy entangled photons termed as the signal and idler are generated by a parametric down-converter (not shown) with a monochromatic pump so that the pump frequency  $\omega_p$  equals the sum of the signal and idler frequencies. These photons are summed in a nonlinear crystal placed inside a one-sided cavity whose  $q^{th}$  longitudinal mode at frequency  $\omega_q$  is detuned from the pump frequency by  $\delta\omega_q = \omega_p - \omega_q$ .

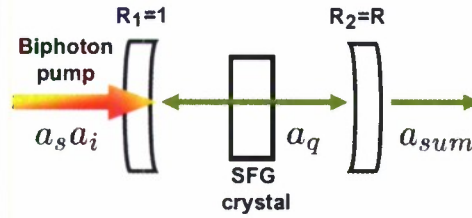


Figure 10: Resonant enhancement technique.

The SFG rate consists of two terms, a term due to quantum SFG, and a term due to classical SFG. It can be shown that the quantum term is monochromatic and varies linearly with input power, while the classical term has a lineshape equal to the convolution of the signal and idler spectra and varies quadratically with input power. Similarly, the SFG rate of the traveling wave case (without cavity) also consists of a quantum term that varies linearly with input power and a classical term that varies quadratically.

The quantum SFG rate is enhanced by the presence of the cavity by an amount equal to the ratio of the quantum terms for the two cases. When the cavity is tuned to resonate the pump frequency ( $\delta\omega_q = 0$ ), the enhancement is

$$cavity/traveling = \frac{4(1 - R)}{[(1 - R) + 2\xi]^2}$$

The largest quantum SFG enhancement is obtained for  $R = 1 - 2\xi$ ; for this reflectivity the enhancement ratio is equal to the inverse of the round trip power loss,  $1/(2\xi)$ .

Of importance, assuming that the signal and idler bandwidths are large as compared to the cavity free spectral range  $\Delta$ , enhancement by the use of a resonant cavity is only possible in the quantum and not in the classical regime. By using the resonance technique described here, both the quantum SFG rate and the ratio of the quantum to classical term may be improved. Our proof-of-principal-experiment configuration is shown in Fig. 11. Frequency-

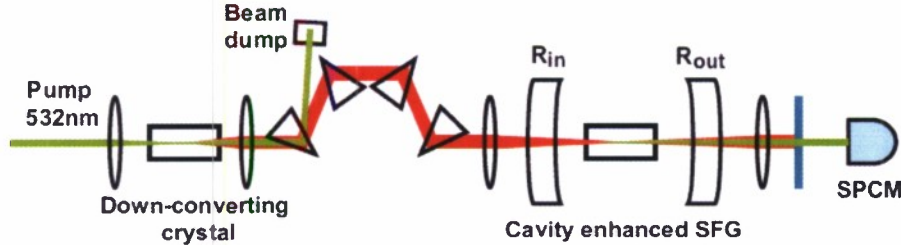


Figure 11: Schematic of experiment.

degenerate biphotons, with a calculated bandwidth of 32 nm, are generated by spontaneous parametric down-conversion in a 20 mm long periodically-poled, magnesium oxide-doped, stoichiometric lithium tantalate crystal (MgO:PPSLT) pumped by an 8 W, CW laser at 532 nm. A four-prism setup is used to filter out the strong pump and to provide dispersion compensation for the down-converted biphotons. SFG of these biphotons occurs inside a cavity that is reflecting at 532 nm and transparent at 1064 nm.

The SFG crystal is a 20 mm long MgO:PPSLT crystal anti-reflection coated at 1064 nm and 532 nm. The confocal cavity consists of two 20 mm radius of curvature spherical mirrors, one of which is mounted onto a piezoelectric crystal. The input mirror has a reflectance of  $R_{in} > 99.5\%$ , and the output mirror has a reflectance of  $R_{out} = 95.5\%$ . (The measured

single-pass crystal loss is  $\xi \sim 2\%$ , and the optimum reflectivity of the output mirror is  $R_{out} = 1 - 2\xi \sim 96\%$ ). The SFG signal is filtered, then collected into multimode fiber and detected with a single photon counting module.

A typical scan of the cavity over a free spectral range is shown in Fig. 12(A). The resonant behavior of the SFG process is clearly observed, with peak generation rates on resonance that are significantly higher than the traveling wave rate of 3200 counts/s. While the cavity is passively stabilized to within a fraction of a free spectral range during the scan period, temperature instability and air currents cause the peak measured SFG rate to fluctuate by an amount that is 6 times larger than the shot noise.

To better quantify the enhancement, we measure the resonantly-enhanced SFG rate at various down-converted infrared (IR) input powers. Figure 12(B) shows the averages and standard deviations of the peak SFG rates at each input power. Also shown is the traveling-wave SFG rate obtained by removing the out-coupling mirror. The linear fits to the data in Fig. 12(B) demonstrate two results. First, the ratio of their slopes gives the SFG enhancement ratio of 12. Second, the linear dependence of the SFG rate on input power, in both cases, shows that it is the quantum SFG term that is enhanced. The enhancement is a factor of two less than the theoretical prediction. The discrepancy may be due to imperfect mode matching or cavity instability.

In addition to demonstrating the effect experimentally, we have also developed a theory for resonantly-enhanced quantum SFG. We work in the Heisenberg picture with traveling wave signal and idler beams denoted by the annihilation operators  $a_s(t, z) = \tilde{a}_s(t, z) \exp[-i(\omega_s t - k_s z)]$  and  $a_i(t, z) = \tilde{a}_i(t, z) \exp[-i(\omega_i t - k_i z)]$ , where operators with a tilde vary slowly with time and distance. We use a slowly varying envelope formalism with the standing-wave cavity mode operator written as  $a_q(t, z) = \tilde{a}_q(t) \exp(-i\omega_q t) \sin(k_q z)$ , where  $k_q = q\pi/L$ . We project the broadband generated dipole moment operator, proportional to  $\tilde{a}_s(t, z)\tilde{a}_i(t, z)$ , against the cavity mode. With the traveling wave SFG field emitted from mode  $q$  denoted by  $a_{sum}(t, z) = \tilde{a}_{sum}(t) \exp[-i(\omega_p t - k_p z)]$ , the equation for the evolution of  $\tilde{a}_q(t)$  and its relation to the SFG field is:

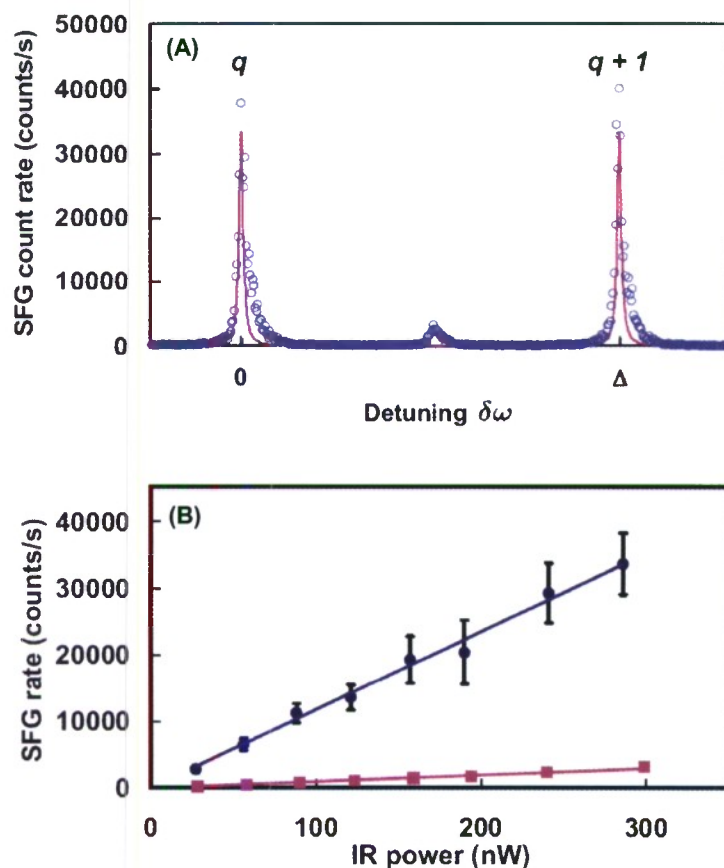


Figure 12: (A) The cavity is scanned over a free spectral range, thereby demonstrating the SFG resonance effect. The pink solid line is the theoretical plot of the quantum term normalized to the average peak rate. Blue circles are experimental data. (B) SFG rate for cavity and traveling wave experiments. Circles are resonant SFG rates averaged over 20-25 peaks obtained in slow cavity scans. Squares are traveling-wave SFG rates averaged over 60-second intervals.

$$\begin{aligned}
\frac{\partial \tilde{a}_q(t)}{\partial t} + \frac{\Gamma}{2} \tilde{a}_q(t) &= \tilde{P}_q(t) \exp(-i\delta\omega t) + \tilde{\mathcal{F}}(t) \\
\tilde{P}_q(t) &= i\kappa_c \frac{2}{L} \int_0^L \tilde{a}_s(t, z) \tilde{a}_i(t, z) \exp(ik_p z) \sin\left(\frac{q\pi z}{L}\right) dz \\
\tilde{a}_{sum}(t) &= \sqrt{\gamma} \tilde{a}_q(t).
\end{aligned} \tag{6.1}$$

Denoting the spacing of the cavity modes at the sum frequency by  $\Delta = c/(2Ln)$ , the decay rate  $\Gamma$  of photons in the cavity is determined by the mirror reflectivity  $R$  and the single pass power loss  $\xi$ . With the output coupling rate  $\gamma = \Delta(1 - R)$ , the total (power) decay rate is  $\Gamma = 2\xi\Delta + \gamma$ . We take all fields to be plane waves with cross sectional area  $A$  and take the refractive index  $n$  and nonlinearity  $d$  to be independent of frequency. With the cavity and summing crystal of the same length, the coupling constant  $\kappa_c = (d/n^2)(\mu_0\hbar\omega_p\omega_s\omega_i L/A)^{1/2}$ . The quantity  $\tilde{\mathcal{F}}(t)$  is a Langevin noise operator that has contributions from an incoming wave at the right hand mirror (not shown) and a macroscopic loss term. Both are negligible at room temperature. The normalization is such that  $\langle \tilde{a}_q^\dagger(t) \tilde{a}_q(t) \rangle$  is the total number of photons in the cavity mode, and  $\langle a_{sum}^\dagger(t) a_{sum}(t) \rangle$  is the rate of sum photons exiting the cavity.

The solution of Eqs. (1) for the SFG field operator is

$$\tilde{a}_{sum}(t) = \sqrt{\gamma} \exp\left(-\frac{\Gamma}{2}t\right) \int_{-\infty}^t \exp\left(\frac{\Gamma}{2}t'\right) \tilde{P}_q(t') \exp(-i\delta\omega t') dt'. \tag{6.2}$$

We assume that the signal and idler fields are not depleted in the summing crystal and transform to the frequency domain using  $a_s(t, z) = \int a_s(\omega, z) \exp(-i\omega t) d\omega$  and  $a_i(t, z) = \int a_i(\omega, z) \exp(-i\omega t) d\omega$ .  $\tilde{P}_q(t)$  becomes

$$\begin{aligned}
\tilde{P}_q(t) &= -\kappa_c \int_{-\infty}^{\infty} \int_{-\infty}^{\infty} \Phi(\omega_1, \omega_2) a_s(\omega_1) a_i(\omega_2) \\
&\quad \times \exp[-i(\omega_1 + \omega_2 - \omega_p)t] d\omega_1 d\omega_2 \\
\Phi(\omega_1, \omega_2) &= \exp\left[-i\frac{\Delta k(\omega_1, \omega_2)L}{2}\right] \text{sinc}\left[\frac{\Delta k(\omega_1, \omega_2)L}{2}\right],
\end{aligned} \tag{6.3}$$



where  $\Phi(\omega_1, \omega_2)$  is a phase matching factor with  $\text{sinc}(x) = \sin(x)/x$  and  $\Delta k(\omega_1, \omega_2) = k_q - [k(\omega_1) + k(\omega_2)]$ . Equation (6.3) is substituted into Eq. (6.2) to obtain the SFG output field:

$$\begin{aligned} \tilde{a}_{sum}(t) = & -\kappa_c \int_{-\infty}^{\infty} \int_{-\infty}^{\infty} \frac{\sqrt{\gamma} \Phi(\omega_1, \omega_2) a_s(\omega_1) a_i(\omega_2)}{\Gamma/2 - i(\omega_1 + \omega_2 - \omega_p + \delta\omega)} \\ & \times \exp[-i(\omega_1 + \omega_2 - \omega_p + \delta\omega)t] d\omega_1 d\omega_2. \end{aligned} \quad (6.4)$$

For monochromatically-pumped down conversion, the down-converted signal and idler fields at the input of the summing crystal,  $a_s(\omega)$  and  $a_i(\omega')$ , where  $\omega' = \omega_p - \omega$ , can be described in terms of initial vacuum fields  $a_{s0}(\omega)$  and  $a_{i0}(\omega')$  as

$$\begin{aligned} a_s(\omega) &= A(\omega) a_{s0}(\omega) + B(\omega) a_{i0}^\dagger(\omega') \\ a_i^\dagger(\omega') &= C(\omega) a_{s0}(\omega) + D(\omega) a_{i0}^\dagger(\omega'). \end{aligned} \quad (6.5)$$

Substituting Eqs. (6.5) into Eq. (6.4) and noting the commutator  $[a_{i0}(\omega_1), a_{j0}^\dagger(\omega_2)] = (1/2\pi)\delta_{ij}\delta(\omega_1 - \omega_2)$ , we evaluate  $\langle a_{sum}^\dagger(t) a_{sum}(t) \rangle$  and find the rate of SFG photons in mode  $q$  exiting the cavity to be

$$\mathcal{R}_{cav} = \left(\frac{\kappa_c}{\pi}\right)^2 \int_{-\infty}^{\infty} \left[ \frac{\gamma}{\Gamma^2 + 4\delta\omega^2} f(\omega) + \frac{\gamma}{\Gamma^2 + 4(\omega - \omega_q)^2} g(\omega) \right] d\omega, \quad (6.6)$$

where  $f(\omega)$  and  $g(\omega)$  are

$$\begin{aligned} f(\omega) &= \left| \int_{-\infty}^{\infty} A(\Omega) C^*(\Omega) \Phi(\Omega, \omega_p - \Omega) d\Omega \right|^2 \delta(\omega - \omega_p) \\ g(\omega) &= \int_{-\infty}^{\infty} |B(\Omega)|^2 |C(\Omega - \omega + \omega_p)|^2 |\Phi(\Omega, \omega - \Omega)|^2 d\Omega. \end{aligned} \quad (6.7)$$

The SFG rate in Eq. (6.6) consists of a quantum term containing the function  $f(\omega)$  and a classical term containing the function  $g(\omega)$ . The quantum term is the result of generation with correlated photons; it may be shown to scale linearly with input power and has a monochromatic spectrum. The classical term comes from SFG with uncorrelated photons

and varies quadratically with input power. Its spectrum is proportional to the convolution of the signal and idler spectra, multiplied by the cavity lineshape.

In order to normalize the improvement that results from the use of a cavity, we write the SFG rate for the traveling wave case with no cavity present. This rate is

$$\mathcal{R}_{tw} = \left( \frac{\kappa_{tw}}{2\pi} \right)^2 \int_{-\infty}^{\infty} [f(\omega) + g(\omega)] d\omega, \quad (6.8)$$

where  $\kappa_{tw} = \kappa_c/\Delta^{1/2}$ , and  $k_q$  in the function  $\Phi(\omega_1, \omega_2)$  becomes  $k(\omega_1 + \omega_2)$ . As in the cavity case, the SFG rate consists of a quantum term that varies linearly with input power and a classical term that varies quadratically.

The quantum SFG rate is enhanced by the presence of the cavity by an amount equal to the ratio of the terms containing  $f(\omega)$  in Eqs. (6.6) and (6.8). When the cavity is tuned to resonate the pump frequency ( $\delta\omega = 0$ ), the quantum SFG enhancement ratio is

$$\eta_q = \frac{4(1-R)}{[(1-R) + 2\xi]^2}. \quad (6.9)$$

Maximizing with respect to  $R$ , the largest quantum SFG enhancement is obtained for  $R = 1 - 2\xi$ ; for this reflectivity the enhancement ratio is equal to the inverse of the round trip power loss,  $1/(2\xi)$ .

To study the effect of the cavity on the classical component of SFG, we assume that the signal and idler spectra are sufficiently broadband that the dipole moment at the sum frequency is constant over many cavity modes. In this case,  $g(\omega)$  is a constant, and the generated SFG spectrum is periodic with resonant peaks separated from each other by the cavity free spectral range. To obtain the net enhancement of the classical term, we integrate over a single free spectral range centered at  $\omega_q$ . The resulting classical SFG enhancement ratio is then

$$\eta_c = \frac{2}{\pi} \int_{\omega_q - \pi\Delta}^{\omega_q + \pi\Delta} \frac{\gamma}{\Gamma^2 + 4(\omega - \omega_q)^2} d\omega \cong \frac{\gamma}{\Gamma} = \frac{1-R}{(1-R) + 2\xi}, \quad (6.10)$$

where the second equality follows for sufficiently high finesse that  $\tan^{-1}(2\pi\Delta/\Gamma) \rightarrow \pi/2$ . If the cavity is lossless,  $\eta_c = 1$ . Though generation at resonance is enhanced, generation off-resonance is suppressed so that the integrated classical SFG enhancement ratio is unity.

Equations (6.9) and (6.10) show how resonating the SFG field enhances the efficiency of quantum SFG while leaving classical SFG unchanged. The enhancement of quantum SFG may find use in correlation experiments that measure the lengths of biphoton wavefunctions which are too short to be measured with time-resolved detectors. In such experiments, the SFG crystal must be very short to have a sufficiently large acceptance bandwidth for the biphotons, and the SFG signal may be small as a result. A resonator could enhance the signal to measurable levels.

## 7 Observation of Nonlocal Modulation with Entangled Photons

The idea of what we term here as nonlocal modulation was published about one year ago; i.e., S. E. Harris, “Nonlocal Modulation of Entangled Photons,” *Phys. Rev. A* **78**, 021807(R) (2008). This section of the report describes the first experimental observation of this effect.

When the photons of a time-energy entangled pair are sent through different channels having arbitrary dispersions, the dispersion in one channel may be negated by dispersion of the opposite sign in the other channel. This effect results from a quantum mechanical interference and has no classical analog. This is now termed as nonlocal dispersion compensation. We report the first observation of a time-frequency analog to nonlocal dispersion cancellation and term this effect as nonlocal modulation. Consider a simplified concept system as shown in left portion of Fig. 13, where a monochromatic pump generates non-degenerate time-energy entangled photon pairs. The signal and idler photons (Channels 1 and 2) pass through sinusoidal phase modulators. These modulators are driven at the same modulation

frequency, and their relative phase may be varied. After passing through the modulators, the signal and idler photons are dispersed, for example, by a prism, and the relative positions (frequencies) of the signal and idler photons are correlated. When the modulation frequency is small as compared to the spectral bandwidth of the signal or idler, we find a consequence of time-energy entanglement that we term as nonlocal modulation. Specifically, these distant modulators act cumulatively to determine the apparent modulation depth. If the two identical modulators have opposite phase, they negate each other and act as if neither modulator were present. Conversely, if operated with the same phase, they produce the same correlation as does a single modulator with twice the modulation depth acting on only one of the photons.

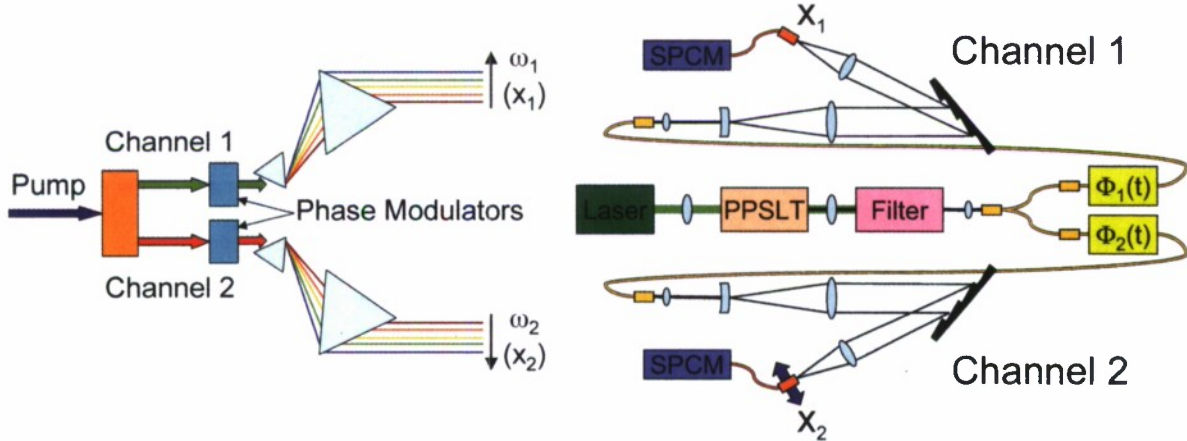


Figure 13: Nonlocal modulation. Signal and idler photons are phase modulated at the same frequency and with controllable phase. The signal and idler beams are frequency-dispersed, and the positions (frequencies) of the detected photons on the photodetectors are correlated. **Left:** simplified concept diagram. **Right:** experimental configuration.

If the resolution of the frequency correlator of Fig. 13 (left) is infinite, the resulting correlation traces for phased and anti-phased modulators may look something like Fig. 14. Since the pump laser which generates the entangled photons is monochromatic, they are delta-function correlated in frequency before any modulation occurs. The modulators act on this delta function correlation by generating sidebands whose distribution depends on the amplitude of the sinusoidal driving signal. If the modulators are run in phase with each other, the distribution of sidebands resembles that of a single modulator with twice



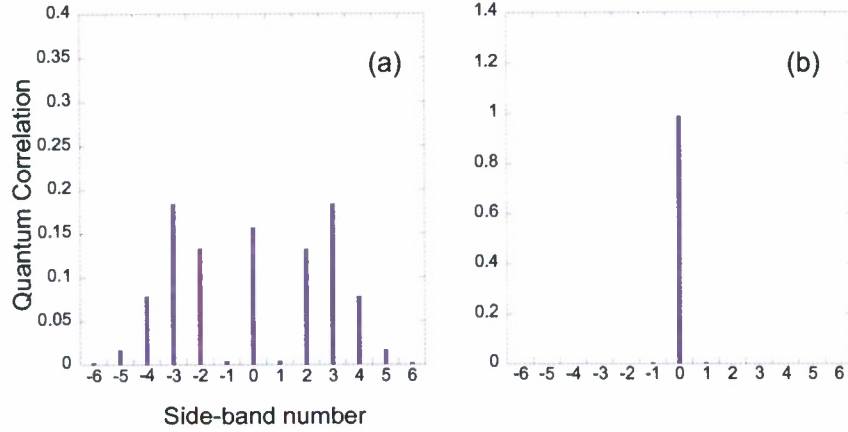


Figure 14: Example frequency correlation function with (a) phased and (b) anti-phased sinusoidal modulators. Because the modulators have the same amplitude, cumulative modulation results in either (a) doubling of modulation depth or (b) cancellation of modulation in the spectral correlation.

the driving amplitude [Fig. 14(a)]. If run with opposite phase, the modulators cancel each other, and a single delta function is present in the correlation, as if neither modulator were present [Fig. 14(b)].

The more detailed experimental configuration is shown in right part of Fig. 13. We pump a 20 mm long, periodically-poled, magnesium oxide-doped stoichiometric lithium tantalate crystal (PPSLT) with 0.8 W from a 532 nm cw laser. The nonlinear crystal is phase matched to produce 32 nm bandwidth, degenerate photon pairs at 1064 nm. All fields are polarized along the extraordinary axis of the crystal. The generated photons are filtered from the strong 532 nm pumping beam using a four-prism setup and are then coupled into a polarization-maintaining fused-fiber beam splitter which diverts the photons into Channels 1 and 2 with equal probability. The photons are passed through identical sinusoidal phase modulators (EOSPACE) which are driven at 30 GHz with modulation depths of about 1.5 radians. The relative phase between the modulators is controlled using a calibrated phase trimmer. The photons then pass through identical monochromators, each having a linear dispersion of 210 GHz/mm and a Gaussian instrument response function with a FWHM of 8.5 GHz. To obtain frequency domain correlation curves, we fix the output slit in Channel 1 at  $x_1$  and scan the position  $x_2$  in Channel 2. The photons that are transmitted through

the monochromator slits are coupled into multimode fibers and detected with time-resolved single photon counting modules (SPCMs, id Quantique id400 and PerkinElmer SPCM-AQR-16-FC).

The primary experimental results of this work are shown in Fig. 15. For each case, we set the monochromator slit in Channel 1 at an arbitrary position  $x_1$  that is near the center of the generated 32 nm spectrum and leave the position of this slit fixed thereafter. The slit in Channel 2 is scanned over positions  $x_2$ , and the coincidence rate of the two detectors (with gate width  $T = 1.25$  ns) is recorded as a function of this position. For each position, the rate is averaged for 20 s.

With the pump frequency defined as  $\omega_p$ , and the position  $x_2$  proportional to the frequency  $\omega_2$ , we express the coincidence rate as a function of relative frequency  $\Delta \equiv \omega_2 - (\omega_p - \omega_1)$ . The scale of the frequency axis is calibrated by measuring the sideband spacing of a single-mode 1064 nm laser modulated at 30 GHz, with the zero position chosen (at the start of the experiment) as the location of the correlation peak for unmodulated photon pairs.

The upper portion of Fig. 15 shows the experimental results without modulation and with modulation in a single channel. In Fig. 15(a) (upper), both modulators are turned off by disconnecting their 30 GHz drive signals. As expected by energy conservation, a single correlation peak is observed. In Fig. 15(b) (upper), Channel 1 is phase modulated as  $\exp[i\delta \sin(\omega_m t)]$  with a modulation depth of  $\delta = 1.5$ , and Channel 2 is not modulated. The frequency correlation is now distributed over a set of sidebands, having Bessel function amplitudes  $J_n^2(\delta)$ , whose total area is equal to that of upper (a) of Fig. 15.

In Fig. 15(a) (lower), both modulators are turned on at a modulation depth of  $\delta = 1.5$ , and the cable length is adjusted so that they have the same phase. They now act cumulatively (constructively interfere) to produce a set of sidebands having a Bessel function distribution  $J_n^2(2\delta)$ . The frequency-domain correlation function of two distant modulators is therefore the same as that which would be obtained by correlating an unmodulated photon with a photon modulated at twice the modulation depth.

In Fig. 15(b) (lower), the modulators are run at the same depth as in the previous paragraph, but now the relative cable length is adjusted so that the modulators are run in phase opposition. The modulators now destructively interfere, and no sidebands are visible.

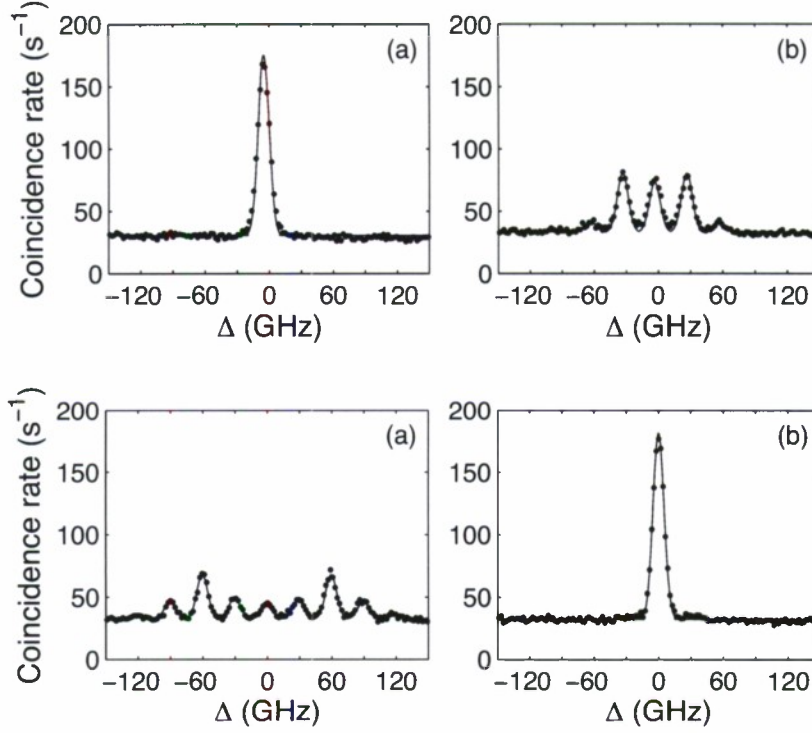


Figure 15: Frequency correlation measurements. The horizontal axes measure relative frequency changes as slit position  $x_2$  is scanned. **Upper:** (a) both modulators turned off and (b) the modulator in Channel 1 running at a modulation depth of 1.5. **Lower:** both modulators running (a) with the same phase and (b) with opposite phase. The modulation depth for both modulators is 1.5. Circles are data; curves are theoretical fits (see text).

The striking difference between Figs. 14 and 15 is that the sidebands are not delta functions but have widths determined by the resolution of the frequency correlator in Fig. 13 (right). We have developed a theory to predict the measured correlation functions with finite-resolution monochromators as used in our experiment. The following describes this theory, which is used to produce the solid curves in Fig. 15.

Working in the Heisenberg picture, a nonlinear crystal of length  $L$  is pumped by a monochromatic laser at frequency  $\omega_p$ . A positive-frequency field operator  $a(\omega, z)$ , representing entangled photons, evolves inside the crystal and may be written in terms of an envelope  $b(\omega, z)$  which varies slowly along the propagation direction:  $a(\omega, z) = b(\omega, z) \exp[ik(\omega)z]$ . The propagation equations describing entangled photon generation are

$$\begin{aligned}
\frac{\partial b(\omega, z)}{\partial z} &= i\kappa(\omega)b^\dagger(\omega_p - \omega, z) \exp[i\Delta k(\omega)z], \\
\frac{\partial b^\dagger(\omega, z)}{\partial z} &= -i\kappa^*(\omega)b(\omega_p - \omega, z) \exp[-i\Delta k(\omega)z].
\end{aligned} \tag{7.1}$$

where  $\kappa(\omega)$  and  $\Delta k(\omega)$  are the coupling factor and wave-vector mismatch, respectively. The solution for the output field at  $z = L$ , expressed in terms of the vacuum field  $a_{\text{vac}}(\omega)$  at the input of the crystal, is

$$a_{\text{out}}(\omega) = A(\omega)a_{\text{vac}}(\omega) + B(\omega)a_{\text{vac}}^\dagger(\omega_p - \omega), \tag{7.2}$$

where, to preserve the commutation relations, the functions  $A(\omega)$  and  $B(\omega)$  satisfy  $|A(\omega)|^2 - |B(\omega)|^2 = 1$  and  $A(\omega)B(\omega_p - \omega) = B(\omega)A(\omega_p - \omega)$ .

The time-domain output field operator is related to its frequency-domain counterpart [Eq. (7.2)] by the inverse Fourier transform,  $a_{\text{out}}(t) = \int_{-\infty}^{\infty} a_{\text{out}}(\omega) \exp(-i\omega t) d\omega$ , and is normalized so that the total rate of generated photons exiting the crystal is  $R_{\text{out}} = \langle a_{\text{out}}^\dagger(t)a_{\text{out}}(t) \rangle$ . The generated photons are separated into two channels, denoted as Channel 1 and Channel 2, using a 50/50 beam splitter. The field operators at the outputs of the beam splitter are  $a_1(t) = a_2(t) = \frac{1}{\sqrt{2}}a_{\text{out}}(t)$ . The photons are modulated by periodic phase modulators whose time-domain, Fourier-series transfer functions are  $m_1(t) = \sum_k q_k \exp(-ik\omega_m t)$  in Channel 1 and  $m_2(t) = \sum_l r_l \exp(-il\omega_m t)$  in Channel 2, with Fourier transforms  $m_1(\omega) = \sum_k q_k \delta(\omega - k\omega_m)$  and  $m_2(\omega) = \sum_l r_l \delta(\omega - l\omega_m)$ , respectively. With the  $*$  symbol denoting convolution, the frequency-domain modulated fields are  $\tilde{a}_1(\omega) = a_1(\omega) * m_1(\omega)$  and  $\tilde{a}_2(\omega) = a_2(\omega) * m_2(\omega)$ . Substituting  $a_1(\omega)$ ,  $a_2(\omega)$ ,  $m_1(\omega)$ , and  $m_2(\omega)$  into the expressions for  $\tilde{a}_1(\omega)$  and  $\tilde{a}_2(\omega)$  yields

$$\begin{aligned}
\tilde{a}_1(\omega) &= \frac{1}{\sqrt{2}} \sum_{k=-\infty}^{\infty} q_k [A(\omega - k\omega_m)a_{\text{vac}}(\omega - k\omega_m) \\
&\quad + B(\omega - k\omega_m)a_{\text{vac}}^\dagger(\omega_p - \omega + k\omega_m)], \\
\tilde{a}_2(\omega) &= \frac{1}{\sqrt{2}} \sum_{l=-\infty}^{\infty} r_l [A(\omega - l\omega_m)a_{\text{vac}}(\omega - l\omega_m) \\
&\quad + B(\omega - l\omega_m)a_{\text{vac}}^\dagger(\omega_p - \omega + l\omega_m)].
\end{aligned} \tag{7.3}$$



The modulated photons are frequency correlated by passing each through identical monochromators whose output slits may be translated to select frequencies  $\omega_1 = \beta x_1$  in Channel 1 and  $\omega_2 = \beta x_2$  in Channel 2, where the constant  $\beta$  is the linear dispersion of the grating systems. The monochromators (spectral filters) have field transmission functions  $H_1(\omega - \beta x_1)$  and  $H_2(\omega - \beta x_2)$ . The filtered field operators in Channels 1 and 2 are  $\tilde{a}_{1f}(\omega, x_1) = \tilde{a}_1(\omega)H_1(\omega - \beta x_1)$  and  $\tilde{a}_{2f}(\omega, x_2) = \tilde{a}_2(\omega)H_2(\omega - \beta x_2)$ , respectively. The count rates at the outputs of the monochromators are given by  $R_1(x_1) = \langle \tilde{a}_{1f}^\dagger(t, x_1)\tilde{a}_{1f}(t, x_1) \rangle$  and  $R_2(x_2) = \langle \tilde{a}_{2f}^\dagger(t, x_2)\tilde{a}_{2f}(t, x_2) \rangle$ . These rates are

$$\begin{aligned} R_1(x_1) &= \frac{1}{4\pi} \sum_{k=-\infty}^{\infty} |q_k|^2 \int_0^{\infty} |B(\omega - k\omega_m)|^2 |H_1(\omega - \beta x_1)|^2 d\omega, \\ R_2(x_2) &= \frac{1}{4\pi} \sum_{l=-\infty}^{\infty} |r_l|^2 \int_0^{\infty} |B(\omega - l\omega_m)|^2 |H_2(\omega - \beta x_2)|^2 d\omega. \end{aligned} \quad (7.4)$$

Assuming a gate width  $T$ , the coincidence rate for the two detectors is related to the second-order Glauber correlation function  $G^{(2)}(t_1, x_1, t_2, x_2) = \langle \tilde{a}_{2f}^\dagger(t_2, x_2)\tilde{a}_{1f}^\dagger(t_1, x_1)\tilde{a}_{1f}(t_1, x_1)\tilde{a}_{2f}(t_2, x_2) \rangle$ . With the assumption that the resolution of the monochromators is high, or equivalently that the filter widths are small (as compared to the modulation frequency  $\omega_m$ ), it can be shown that the correlation function depends only on the difference of the arrival times  $\tau = t_2 - t_1$ , and the coincidence rate is

$$R_c(x_1, x_2) = \int_{-T/2}^{T/2} G^{(2)}(\tau, x_1, x_2) d\tau. \quad (7.5)$$

Equation (7.5) may be expanded using Wick's theorem and shown to be given by

$$R_c(x_1, x_2) = R_1(x_1)R_2(x_2)T + \int_{-\infty}^{\infty} \left| \sum_{k=-\infty}^{\infty} q_k r_{n-k} F_k(\tau, x_1, x_2) \right|^2 d\tau, \quad (7.6)$$

where  $\Delta = \beta(x_1 + x_2) - \omega_p$ ,  $n = \lfloor \Delta/\omega_m + \frac{1}{2} \rfloor$ , and

$$\begin{aligned} F_k(\tau, x_1, x_2) &= \frac{1}{4\pi} \int_0^{\infty} A(\omega - k\omega_m) B(\omega_p - \omega + k\omega_m) \\ &\quad \times H_1(\omega - \beta x_1) H_2(\omega_p - \omega - \beta x_2 + n\omega_m) \exp(i\omega\tau) d\omega. \end{aligned} \quad (7.7)$$

The first term in Eq. (7.6) is the result of accidental coincidences between unpaired photons in a gate width  $T$ . The second term is the coincidence rate between paired photons and captures the modulation effects described in this section. To obtain Eqs. (7.4)–(7.7), we have assumed that the transmission widths of the monochromators are small as compared to the modulation frequency and large as compared to the inverse of the temporal gate width  $T$ . In our experiment these assumptions are satisfied by factors of 3.5 and 11, respectively.

If we further assume that  $A(\omega)$  and  $B(\omega_p - \omega)$  are constant in the vicinity ( $\pm 150$  GHz in Fig. 15) of  $\omega = \beta x_1$  and are equal to  $A_0$  and  $B_0$ , respectively, then Eq. (7.6) becomes

$$R_c(\Delta) = R_1 R_2 T + c_n H^{(2)}(n\omega_m - \Delta), \quad (7.8)$$

where  $H^{(2)}(\omega) = |H_1(\omega)|^2 * |H_2(\omega)|^2$ , and

$$R_1 = \frac{1}{4\pi} |B_0|^2 \int_{-\infty}^{\infty} |H_1(\omega)|^2 d\omega, \quad (7.8a)$$

$$R_2 = \frac{1}{4\pi} |B_0|^2 \int_{-\infty}^{\infty} |H_2(\omega)|^2 d\omega, \quad (7.8b)$$

$$c_n = \frac{1}{8\pi} \left| A_0 B_0 \sum_{k=-\infty}^{\infty} q_k r_{n-k} \right|^2. \quad (7.8c)$$

The solid curves in Fig. 15 are theoretical fits to the data using Eq. (7.8) shifted horizontally so as to match center. The Fourier series coefficients for sinusoidal phase modulators are Bessel functions with  $q_k = J_k(-\delta_1)$  and  $r_l = J_l(-\delta_2)$ , where  $\delta_1$  and  $\delta_2$  are the modulation depths in Channels 1 and 2, respectively ( $|\delta_1| = |\delta_2| = 1.5$  in our experiment). We model the monochromator response functions in Channels 1 and 2 as Gaussians with FWHM bandwidths  $\Gamma$ :  $H_1(\omega) = \alpha_1 \exp[-2 \ln(2) \omega^2 / \Gamma^2]$  and  $H_2(\omega) = \alpha_2 \exp[-2 \ln(2) \omega^2 / \Gamma^2]$ . (The monochromator in Channel 1 is the mirror image of the one in Channel 2 which has a measured FWHM bandwidth of 8.5 GHz.) The transfer functions include fitting parameters  $\alpha_1$  and  $\alpha_2$  used in Fig. 15 to account for transmission losses and the difference in detection efficiencies of the photon counters.

To obtain the constants  $A_0$  and  $B_0$ , for each case in Fig. 15, we measure the average value of  $R_2$  and use Eq. (7.8b) to calculate  $|B_0|$ . We obtain  $|A_0|$  from the commutator-preserving condition  $|A_0|^2 - |B_0|^2 = 1$ . For all curves, the fitting parameters are taken as  $\alpha_1^2 = 1.20 \times 10^{-2}$  and  $\alpha_2^2 = 5.59 \times 10^{-4}$ . These values are in good agreement with loss measurements and estimates of the photon counter detection efficiency, where we note that the id400 detector in Channel 1 has a detection efficiency an order of magnitude larger than the SPCM-AQR-16-FC detector in Channel 2.

## 8 Chirp and Compress with Biphotons

### Background

When the bandwidth of an optical pulse is equal to, or greater than, its central frequency and when all of its spectral components are in phase, the pulse develops a characteristic waveform that is termed as single cycle. A chirped, quasi phase matched nonlinear crystal is a technique for generating nonclassical pairs of photons (biphotons) whose characteristic coincidence time, as measured at distant detectors, is a single optical cycle. The elements of the technique are (1) the suggestion for using parametric down conversion to spontaneously generate pairs of entangled photons whose instantaneous frequencies are chirped in opposite directions, and (2) the use of the nonlocal nature of entangled photons to allow the dispersion, as experienced by one photon, to cancel out the dispersion of the second photon and to compress the biphoton wave packet.

A key motivation for the study of single-cycle biphotons is their potential application to nonlinear optical processes with nonclassical fields. One example is the use of sum frequency generation (SFG) as an ultrafast correlator of biphotons. The efficiency for generating sum

frequency photons varies inversely with the width of the incoming biphoton; i.e., single-cycle biphotons behave as if they have an effective power equal to their energy divided by their temporal width. Similarly, in the absence of intermediate resonances, single-cycle biphotons maximize the two photon transition probability. Other uses for ultra-wideband biphotons include nonclassical metrology and large bandwidth quantum information processing.

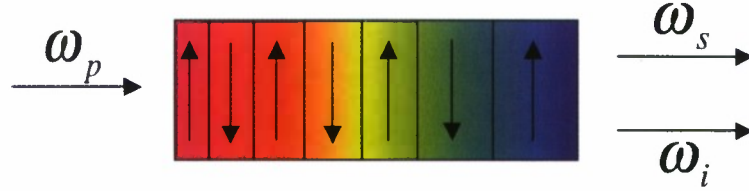


Figure 16: Chirped-poled nonlinear crystal. Arrows indicate the sign of the nonlinear coefficient.

As shown in Fig. 16, we make use of a quasi-phase-matched (QPM) periodically poled crystal. The up-down arrows show the sign of the nonlinear coefficient in each domain of the crystal. These domains are reversed with a period such that the corresponding spatial frequency,  $2\pi/\Lambda$ , is linearly chirped. The poling period is chosen so that the signal frequency is phase matched for red emission at the left end of the crystal and for blue emission at the right end of the crystal. Paired photons that are emitted from the right end arrive at their respective photodetectors at the same time. Paired photons that are emitted from the left end of the crystal arrive at the photodetector with a time difference determined by their group velocities. In the ideal case where there is no group velocity dispersion, the biphoton wave packet is (exactly) linearly chirped. Figure 17 shows the near-white light spectrum of a 2 cm long QPM crystal of  $\text{LiNbO}_3$  pumped with a monochromatic laser at a wavelength of  $0.420 \mu\text{m}$ . Here, the spatial frequency of the domain reversals varies linearly with distance and is chosen so that the crystal is phase matched at a signal wavelength of  $0.750 \mu\text{m}$  at the left end and  $0.464 \mu\text{m}$  at the right end. This corresponds to a poling period of  $3.11 \mu\text{m}$  at the left end and  $7.02 \mu\text{m}$  at the right end of the crystal. When compressed, this spectrum corresponds to a biphoton with a temporal length that is nearly a single optical cycle at the degenerate wavelength of  $0.840 \mu\text{m}$ . The refractive index as a function of frequency, for this figure, is  $n_e(\omega)$  and is obtained from the Sellmeier equation for e-polarized light in  $\text{LiNbO}_3$ .



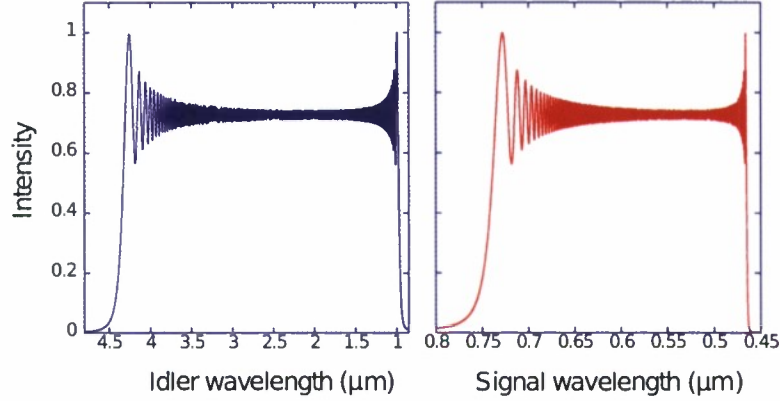


Figure 17: Calculated spectrum of spontaneously generated chirped photons for a 2 cm long QPM crystal of  $\text{LiNbO}_3$  pumped at  $0.420 \mu\text{m}$ .

## Theoretical Work

We have developed a strong understanding of the physics of nonlinear optics with biphotons, specifically sum frequency generation, and now have a well-understood theory to solve other linear and nonlinear quantum optical processes using down-converted photons. We have developed equations and numerical codes which allow us to simulate down conversion in periodically- and chirped-poled nonlinear crystals. Of particular importance are codes which simulate biphoton generation in poled crystals with arbitrary domain patterns, leading to new ideas for obtaining very short biphotons (e.g. using a nonlinearly-chirped crystal to compensate for dispersion). Our numerical tools also demonstrate the effects of the rather large (and unavoidable) poling errors present in real crystals and have lead to a particularly interesting discovery that the chirp/compress strategy for generating single-cycle biphotons is very robust to these errors. As an example showing the usefulness of our code, we apply it to an experiment in progress. We are currently setting up an ultrafast correlator to measure the width of a modestly-chirped biphoton. We are using a chirped-poled crystal from HC Photonics which has a linear k-vector chirp. The crystal is magnesium oxide-doped stoichiometric lithium tantalate ( $\text{MgO:SLT}$ ), with a poling period which varies from  $8.0481$  to  $8.0223 \mu\text{m}$  over its 2 cm length from input to output. Our numerical code computes the theoretical biphoton wavefunction generated by the crystal, as shown in Fig. 18.

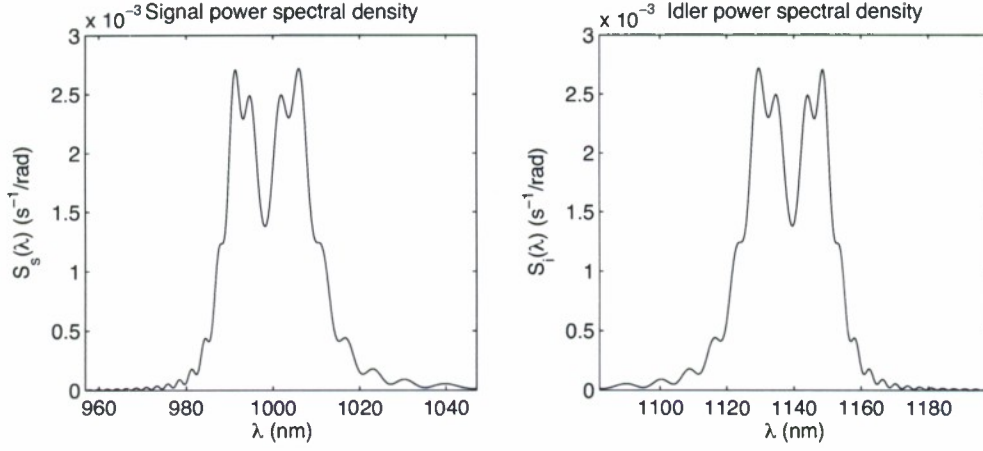


Figure 18: Numerical simulation computing the output of a chirped nonlinear crystal (2 cm long MgO:SLT). Calculated spectrum of the signal (left) and idler (right) photons.

As a check to our theory, we have measured the spectra of the signal and idler photons generated by the MgO:SLT crystal, shown in Fig. 19. The measurements were made with a Jarrell Ash MonoSpec 27 CCD spectrograph. The bandwidth appears to be accurate, and some of the features (e.g. lobes) predicted by the numerical code can be seen in the spectra.

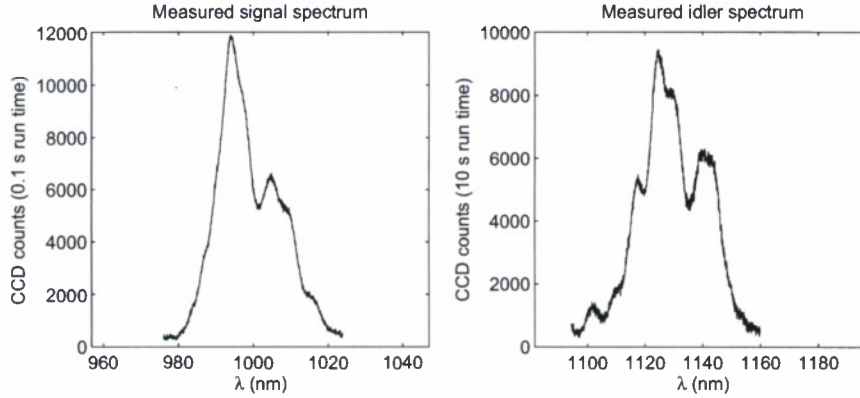


Figure 19: Measured spectra of the signal and idler photons generated by a chirped nonlinear crystal (2 cm long MgO:SLT).

To measure the correlation function for the biphotons generated in the chirped crystal, we plan to use a 1 mm LiNbO<sub>3</sub> crystal to generate 532 nm SFG from the biphotons as we vary the delay between them (more details will be discussed in the experimental section).

The numerical code also predicts the SFG correlation curves for such an experiment, which are shown in Fig. 20 for the chirped (left) and compressed (right) biphotons. The simulation which produced Figs. 18 and 20 did not include poling errors, but they are easily simulated with the same code.

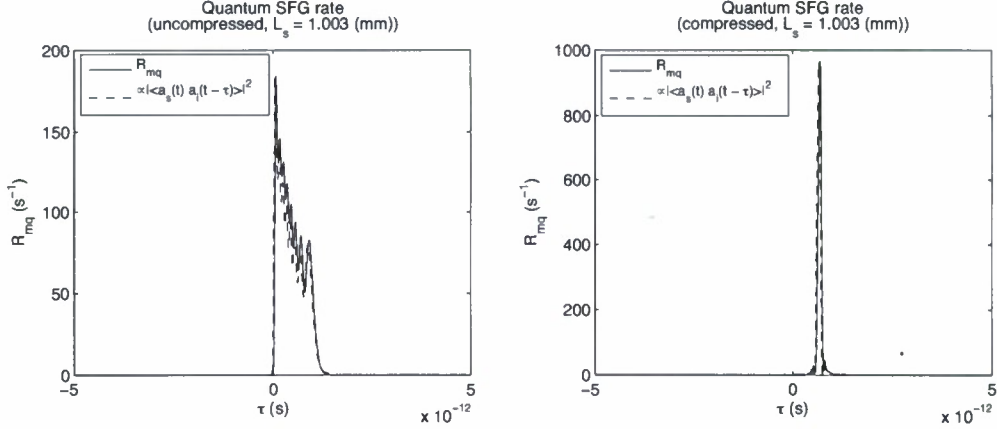


Figure 20: Numerical calculation of expected SFG correlation measurement. **Left:** correlation function of the chirped biphoton. **Right:** correlation function for the biphoton after compression.

In addition to the theoretical work directly related to our chirp and compress experiment, we have also studied other problems related to broadband biphotons. We have introduced a new form of spectroscopy, called Quantum Fourier Transform Spectroscopy (QFTS), which allows determination of the complex refractive index of an unknown material using a narrowband detector. The technique relies on sum frequency generation of biphotons and homodyning the coherent output with a local oscillator; it cannot be done with classical light sources. By working in the Heisenberg picture, our theory has made it especially straightforward to simulate parametric down conversion in the high gain regime, allowing the same simple equations to be used to simulate nonlinear and quantum optics with the N-photon states generated in this regime. One interesting result of this analysis is that nonlocal cancellation of dispersion (a property which allows biphotons to be compressed by acting on only one photon of the pair) is observable at classically high power levels. Our theory has also led us to predict Hong-Ou-Mandel interference with chirped biphotons. In the case of

ideal linear chirps (no matter how large), the shortest possible HOM dip can be achieved with zero dispersion compensation. This makes broadband biphotons generated by chirped crystals attractive for experiments which utilize narrow HOM dips (such as quantum optical coherence tomography).

## Experimental Work

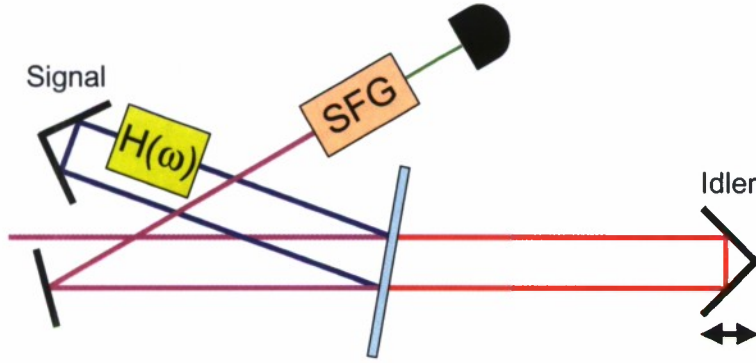


Figure 21: Sum frequency generation correlator setup using a dichroic mirror to separate signal and idler photons. The biphoton is compressed in the signal channel, and the idler photon is delayed for correlation.

We are currently in the process of setting up a proof-of-principle experiment to demonstrate the idea of chirping and subsequently compressing biphotons to achieve narrow correlation widths and increased efficiency of a nonlinear process. The basic correlation setup is shown in Fig. 21. The biphotons, incident from the left, separate into signal and idler photons at a dichroic beam splitter. The beam splitter is a long-pass edge filter (Semrock LP02-1064RS-25) with a very sharp transition edge that can be angle tuned to 1064 nm, the wavelength separating our photons (see Fig. 18). The idler photon passes through the filter and is retroreflected back through the filter. The retroreflector is mounted on an automated translation stage which can travel up to 24 mm in 10 nm steps (Newport VP-25XL), allowing high-resolution correlation traces. The signal photon is reflected from the filter and passes through a separate arm in the correlator. In the first phase of the experiment, this arm will simply return the photon to be overlapped with the delayed idler photon at the beam



splitter. In the second phase of the experiment, a compressor (custom chirped mirrors from Femtolasers) will be inserted in the signal beam path to compress the biphoton chirp. The recombined signal and (delayed) idler photon are focused into a 1 mm long periodically-poled MgO-doped LiNbO<sub>3</sub> crystal to generate 532 nm SFG. The SFG will be measured by a single photon counting module (PerkinElmer SPCM-AQR-16-FC) and recorded as a function of idler photon delay to measure the correlation function of the biphoton. When the two phases of the experiment are complete, we expect to see compression of the correlation width by a factor of 10, with a corresponding increase in SFG rate (as predicted by Fig. 20).

## 9 Nonlinear Optics at X-Ray Wavelengths

Our motivation for this work is the construction of the new LCLS (Linac Coherent Light Source) at Stanford. This source will use about 1/3 of the present SLAC accelerator and will produce FEL radiation at wavelengths as short as 1.5 Angstroms. The projected operating parameters for this light source are: average power=  $10^{14}$  photons per second; pulse duration= 2 fs; photons per pulse= $1.1 \times 10^{12}$ ; repetition rate =100 Hz; angular divergence= $0.8 \times 10^{-6}$  radians. Taken together these parameters should allow the first demonstration of new types of nonlinear x-ray effects.

We anticipate LCLS experiments in the following areas: 1) The demonstration of second harmonic generation in its own right and for application to the measurement of the temporal structure of the LCLS femtosecond time scale laser pulses. As in the visible region of the spectrum these experiments will be done by splitting the x-ray beam and temporally delaying one portion relative to the other, thereby allowing the use of a slow detector. 2) The demonstration of mixing of a fs time scale visible laser with the LCLS beam. We have found that the conversion efficiency for this latter process is about four orders of magnitude larger

than for x-ray frequency doubling, and it is therefore likely that this effect will allow the development of practical correlation with a resolution of the shortest available Ti:Sapphire lasers. 3) Because this type of non-linear x-ray-visible process is dependent on the locations of the valence electrons it is possible that it can be developed into a method for the studying the shape of chemical bonds. 4) Experiments on parametric down conversion: These experiments would first be aimed at studying the basic process, for example the correlated count rate as a function of angle, position, and frequency. 5) More advanced experiments will be aimed at measuring the temporal length of the generated correlated biphotons. Of importance our calculations show that these photons are born with a length of less than  $10^{-17}$  sec. It may therefore be surprising easy to generate photons allowing measurement of atomic scale distances. 6) It is likely that the LCLS will lead to a variety of experiments which make use of entanglement at x-ray wavelengths. These include studies of effects such as ghost imaging and Hong-Ou-Mandel beam splitter experiments on ultrashort x-ray correlation

In the following we summarize our theoretical study and describe our proposed experiments.

## X-Ray Nonlinearites

The central concept pointed out in the earlier papers of Freund and Levine (*Phys. Rev. Lett.* **23**, 854, 1969) and Eisenberger (*Phys. Rev. Lett.* **26**, 684, 1971) is that, since X-ray photons have energies that are large as compared to the electron binding energy of light elements, but still small as compared to the electron rest mass, that the nonlinearity of an element such as diamond may be calculated by treating all of the electrons in the atom as free particles; and therefore representing the nonlinear medium as a very dense, (on order of  $10^{24}$  electrons per cubic centimeter) cold plasma. Of most importance, the periodic lattice structure causes the plasma to be periodic. In a homogeneous plasma the projection of the nonlinear current density against the driving fields is zero and the effective second order nonlinearity is zero. The charge density of this effective plasma is determined by the reciprocal lattice k-vectors, weighted by the appropriate structure and form factors. (Note that this is different from

conventional nonlinear optics in a periodically poled medium where the nonlinearity exists irrespective of the poling period.)

The nonlinearity of this dense plasma is determined by, at first, seemingly different physical processes. These are a) the Lorentz-force, b) convection, as determined by the spatial variation of velocity, and c) a current density caused by the spatial variation of the time-varying charge times the first order velocity. In recent work, we have shown that the plasma nonlinearity will satisfy detailed balance and the Manley Rowe relations. This is at first not-obvious; for example one may show that the Lorentz-force term, when taken separately from the other terms does not satisfy the Manley-Rowe relation and would not, in its own right produce correlated photons. But by taking the sum of the Lorentz term, the convection term, and the second order current term, all on an equal footing, detailed balance is regained.

It should perhaps be noted that though the nonlinear coefficients at x-ray frequencies are much smaller than those at optical wavelengths, this is offset by the the ability to focus the driving beams much more tightly. Also, in the case of parametric down conversion, though the conversion efficiency from the vacuum field is reduced, the number of modes in k-space is greatly increased.

We noted that the second order nonlinear effects we discuss here can be considered as as a combination of an electric quadrupole-type and a magnetic dipole-type nonlinearities. As was shown by P. S. Pershan (Phys. Rev. 130, 919 (1963)) these type of nonlinearities are not zero in materials having a center of inversion; i.e. second order nonlinear x- ray processes may occur in materials possessing inversion symmetry.

## SHG at X-Ray frequencies

### 9.0.1 Nonlinearity

For SHG process the nonlinear current density is (Y. R. Shen The Principles of Nonlinear Optics p. 543 )

$$J^{(2\omega)} = \frac{iq^2}{2m^2\omega^3} \left( \frac{\rho_0}{4} \nabla (\vec{E}^\omega \cdot \vec{E}^\omega) + (\nabla \rho_0 \cdot \vec{E}^\omega) \vec{E}^\omega \right) \cdot \hat{e}^{(2\omega)} \quad (9.1)$$

Where  $q, m$  are the electron charge and mass respectively,  $\omega$  is the frequency of the fundamental beam,  $\rho_0$  is electron charge density (in the x-ray regime this is the Fourier component corresponding to the lattice reciprocal vector),  $\vec{E}^\omega$  is the electric field of the fundamental beam, and  $\hat{e}^{(2\omega)}$  is the direction of the electric field of the second harmonic beam.

### 9.0.2 Phase Matching for a Single Pump Beam

The phase matching diagram for the Laue geometry is shown in Fig. 22 With  $\vec{k}_\omega$ , and  $\vec{k}_{2\omega}$ , and  $\vec{Q}$  denoting the k-vectors of the fundamental, second harmonic, and reciprocal lattice vector, the phase matching condition for a second harmonic generation (SHG) process at x-ray wavelengths is  $2\vec{k}_\omega + \vec{Q} = \vec{k}_{2\omega}$ .

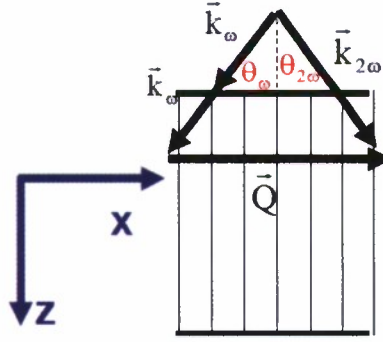


Figure 22: Phase matching diagram for x-ray SHG for a single fundamental beam.  $\vec{k}_\omega$ ,  $\vec{k}_{2\omega}$ , are the wave vectors of the fundamental and second harmonic beams respectively.  $\vec{Q}$  is the reciprocal lattice vector of the diamond crystal

As is shown in Fig. 22, we define  $\theta_\omega$ , and  $\theta_{2\omega}$  as the angles between the atomic planes and the fundamental beam and the second harmonic beam respectively. Ignoring dispersion,  $2\vec{k}_\omega = \vec{k}_{2\omega}$  and the phase matching condition is identical to that of Bragg's law for an x-ray beam at a frequency of  $2\omega$ . However, dispersion does exist and  $\theta_{2\omega}$  and  $\theta_\omega$  have values which are close to but different from the Bragg angle (at  $\theta_{2\omega}$ ). Of importance the SHG and Laue rocking curves do not overlap, thereby avoiding diffraction of the generated second harmonic beam. For the (111) reflection of diamond and for a second harmonic signal at 16

keV, the deviation of  $\theta_{2\omega}$  from the Bragg angle is  $24 \mu$  rad. Using the dynamical theory of x-ray diffraction in the plane wave approximation (Dynamical Theory of X-Ray Diffraction, Andre' Authier, "Oxford Science Publication", New York, 2001), one finds that the Darwin width at 16 keV is  $12 \mu$  rad. Recently, by solving numerically the full coupled equations (including SHG and linear Laue diffraction), we found that for a fundamental spot size of  $2\mu m$  and assuming phase matching for the SHG, less than one percent of the generated second harmonic is linearly diffracted. We therefore neglect the linear diffraction of the second harmonic beam.

### 9.0.3 Beam Profiles and Efficiency

By using the undepleted pump approximation and neglecting the scattering of the generated second harmonic signal, together with the nonlinear susceptibility calculations, we have carried out calculations that predict the SHG efficiency and its dependance on the propagation distance. We also calculated the intensity profile in the transverse plane of the generated second harmonic beam. The slowly varying envelope equation at the second harmonic in the Laue configuration and for coplanar electric fields reads as

$$\begin{aligned} \frac{\lambda}{2\pi} \left( -\sin \theta_B \frac{\partial E^{(2\omega)}}{\partial x} + \cos \theta_B \frac{\partial E^{(2\omega)}}{\partial z} \right) \\ = i\chi^{shg}(E^{(\omega)})^2 + \\ i \left( \chi'(2\omega) - \chi'(\omega) \cos(2\theta_B) + 2 \cos(2\theta_B) \delta\theta_1 + i\chi''(2\omega) \right) E^{(2\omega)} \end{aligned} \quad (9.2)$$

Here  $\chi^{shg} = \frac{\rho_0 q^2 \sin(2\theta_B) (4 \cos(2\theta_B) - 1)}{m^2 \omega^4 \epsilon_0}$  is the nonlinear susceptibility,  $\theta_B$ , is the vacuum Bragg angle at the second harmonic,  $\lambda$  is the vacuum wavelength at the second harmonic,  $\chi'(2\omega)$ ,  $\chi'(\omega)$  are the real parts of linear susceptibilities of the second harmonic and the fundamental respectively.  $\chi''(2\omega)$  is the imaginary part (loss) of the linear susceptibility of the second harmonic beam.  $\delta\theta_1$  is the angular deviation of the pump beam from the vacuum



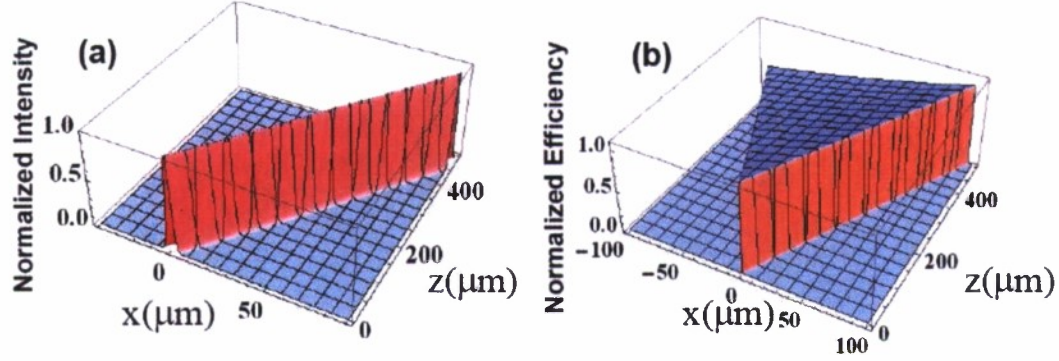


Figure 23: (a) Normalized Intensity of the fundamental vs.  $x$  and  $z$  (b) SHG efficiency vs.  $x$  and  $z$

Bragg angle. The absorption of the pump is introduced by taking the pump field as a decaying exponent.

The efficiency of the SHG process depends linearly on the intensity of the fundamental beam. Therefore we will focus the LCLS beam to a beam spot of a few microns. Though this yields the highest efficiency, it causes the second harmonic beam to be generated at an angle of  $\theta_\omega + \theta_{2\omega}$  with regard to the fundamental driving beam. As a result, the beams overlap in space for a distance which is determined by the spot size of the fundamental beam and the angle between the two beams. For a pumping beam diameter of  $2\mu\text{m}$  at 8 Kev, this distance, which we will refer as the “interaction length”, is  $10\mu\text{m}$ . For transparent crystals which are thicker than interaction length, the SHG efficiency grows as the propagation length, and not as its square, as in conventional nonlinear optics (or in the case where this walk-off effect is negligible). This effect results in a reduction of the power of the generated second harmonic and a spreading of the second harmonic signal in the transverse plane. This effect is shown in Fig. 23. Fig. 23(a) shows the normalized intensity of the fundamental vs.  $x$  (a coordinate parallel to the crystal’s boundary) and  $z$  (a coordinate normal to the boundary). Fig. 23(b) shows the efficiency of the SHG vs.  $x$ ,  $z$  in normalized units.

To estimate the efficiency we assume a fundamental flux of  $4 \times 10^9$  photons per pulse at 8keV, a pulse length of 2fs and beam diameter of 2 microns. We have used the diamond

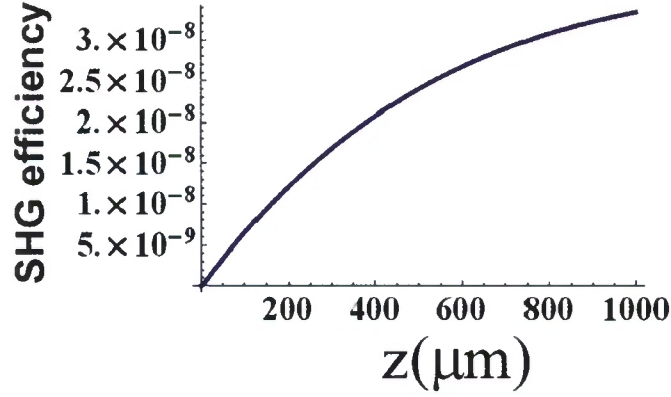


Figure 24: SHG efficiency vs. crystal thickness.

(111) reflection for phase matching the nonlinear medium. Fig. 25 shows the efficiency as function of the diamond thickness. For short crystal thicknesses ( but thicker than the interaction length) the efficiency increases linearly with the thickness, but at larger propagation distances, absorption plays a limiting important role, and the efficiency dependance on the propagation distance becomes sub-linear. The intensity profile for several crystal thickness are shown in Fig 24. One can see very clearly that the intensity profile is broaden with the crystal thickness. While for thickness of  $20\mu m$  the beam diameter is still comparable to the beam diameter of the fundamental, for a thickness of  $100\mu m$  the profile is 5 times broader, and for a  $500\mu m$  the profile is about 100 times broader than the intensity profile of the pump beam.

#### 9.0.4 Experimental Setup

The anticipated second harmonic data rate is on the order of a single to ten photons per pulse when LCLS is operating in short pulse mode and the beam is focused to a 2 micron spot size. The expected signal is extremely small and background levels must be carefully considered. As such, a crystal analyzer will be used to isolate the generated second harmonic photons

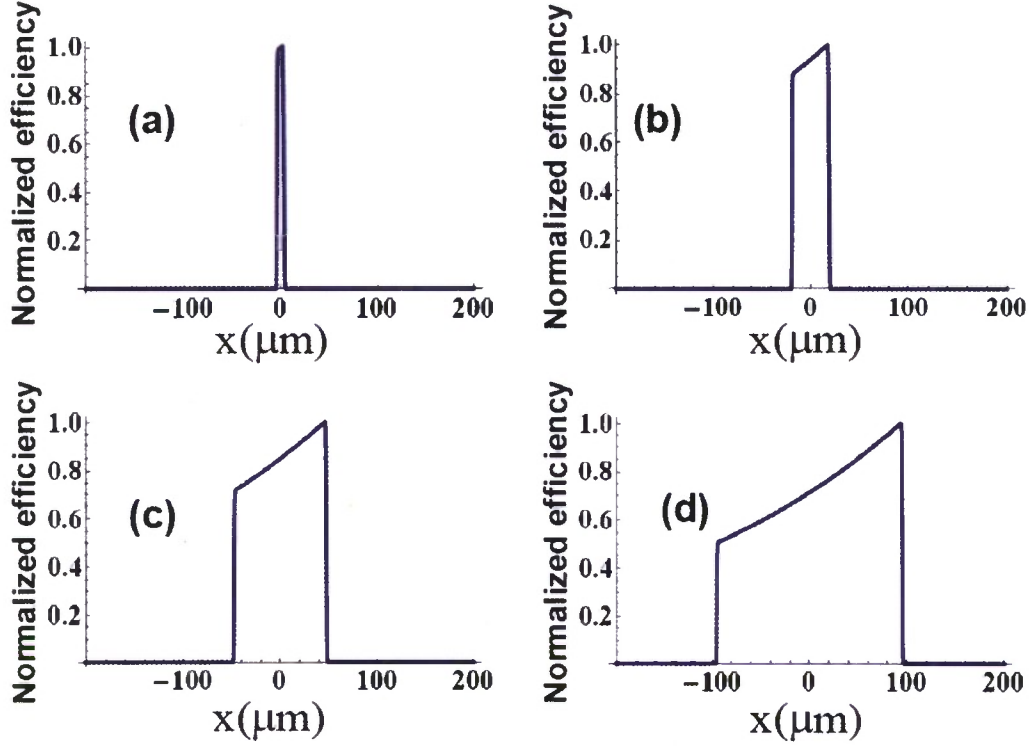


Figure 25: Normalized profile of the SHG efficiency for several crystal thickness (a)  $20\mu m$  (b)  $100\mu m$ , (c)  $250\mu m$ , and (d)  $500\mu m$

from the elastic and inelastic background signal from fundamental and  $3^{rd}$  harmonic photons in the incident beam. A channel cut analyzer is needed to prevent background signal from double scattering events from the sample and first analyzer crystal. However, this scheme is dependent upon an incident beam that is free from  $2^{nd}$  harmonic photons. This is achieved using a combination of a silicon 111 monochromator, harmonic rejection mirror system and the chromaticity of the XPP focusing lens system. This combination of X-ray optics will create a spectrally pure beam of sufficient quality for the proposed experiment. A schematic of the setup, including photon numbers after each optical element, is displayed in upper part of Figure 26.

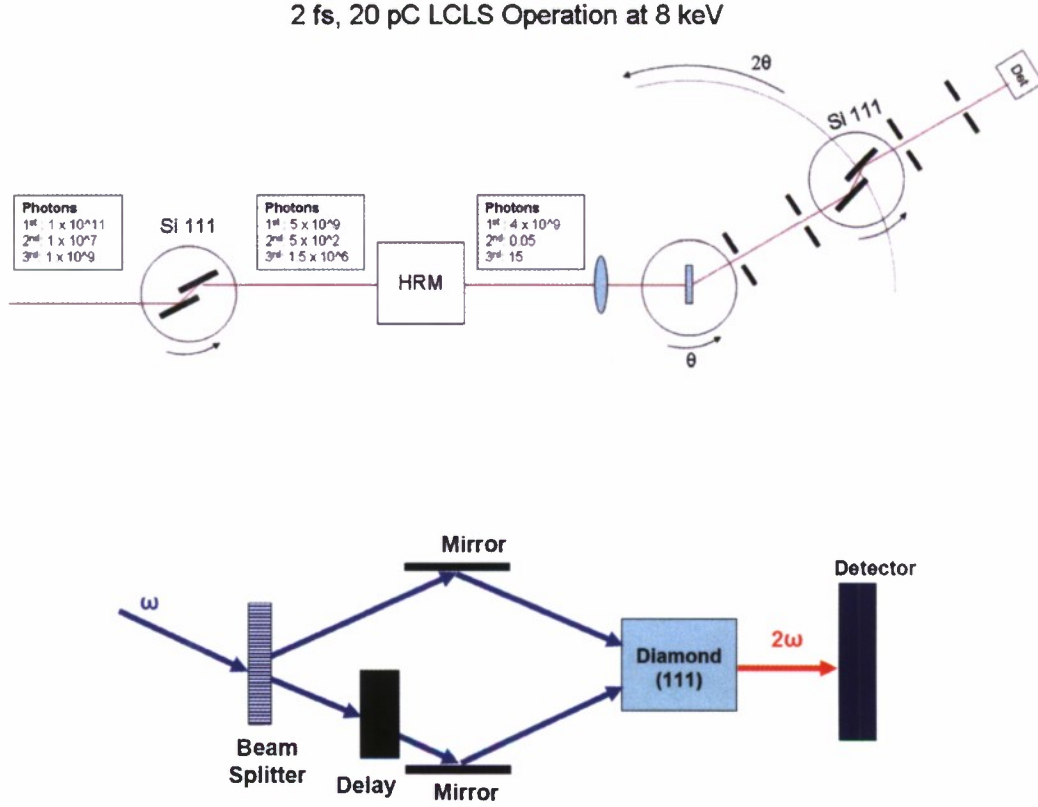


Figure 26: **Upper:** Schematic of the SHG experimental setup. A silicon 111 channel cut monochromator, 2 bounce harmonic rejection mirror system and beryllium compound refractive focusing lens will be used to prepare the incident X-ray beam. The expected photon numbers for the fundamental, 2<sup>nd</sup> and 3<sup>rd</sup> harmonic are displayed before the monochromator, after the monochromator and after the Harmonic Rejection Mirror system. A silicon 111 analyzer crystal and photodiode will be used, with apertures, to detect the generated second harmonic signal. **Lower:** Schematic diagram for x-ray intensity correlation.

### 9.0.5 Correlation of the X-Ray Free Electron Laser (XFEL)

The LCLS is expected to deliver femtosecond pulses with the high powers that are sufficiently high to allow observation of SHG. In the optical regime, SHG is now widely used in autocorrelators for measuring the pulse duration of sub 100 femtosecond pulses. It is therefore reasonable to believe that a similar technique may be established in the x-ray region. Lower part of Fig. 26 shows a possible scheme for autocorrelation measurement. The beam from the LCLS will be split into two portions. One portion of the beam will propagate through a delay line and then the two portions of beam will recombined at the nonlinear material. A second harmonic beam, proportional to the product of the intensities of two portion of the fundamental beam will be generated. The slow detector will integrate the intensity with respect to the time . By varying the delay time between the two portion of the beam, one can obtain the autocorrelation function of the beam intensity.



## 10 Joint Support

The work described in this report was jointly supported by the U.S. Air Force Office of Scientific Research, the Defense Advanced Research Projects Agency, and the U.S. Army Research Office. This joint support was essential for all aspects of this project.

## APPENDIX:

### A Publications During Grant Period

- (1) S. E. Harris, “Chirp and Compress: Toward Single-Cycle Biphotons,” *Phys. Rev. Lett.* **98**, 063602 (February 2007).
- (2) S. Du, J. Wen, M. H. Rubin, and G. Y. Yin, “Four-Wave Mixing and Biphoton Generation in a Two-Level System,” *Phys. Rev. Lett.* **98**, 053601 (2007).
- (3) Jianming Wen, Shengwang Du, and Morton H. Rubin, “Biphoton Generation in a Two Level Atomic Ensemble,” *Phys. Rev.* **A75**, 033809 (2007).
- (4) P. Kolchin, “Electromagnetically-Induced-Transparency-Based Paired Photon Generation,” *Phys. Rev.* **A75**, 033814 (2007).
- (5) S. E. Harris and S. Sensarn, “Toward Single-Cycle Biphotons,” in Coherence and Quantum Optics IX: Proceedings of the Ninth Rochester Conference on Coherence and Quantum Optics, edited by N.P. Bigelow, J.H. Eberly, and R. Stroud, Jr. University of Rochester, Rochester, NY., 65-71, (June 10-13, 2007).
- (6) Shengwang Du, Eun Oh, Jianming Wen, and Morton H. Rubin, “Four-wave Mixing in three-level Systems: Interference and Entanglement,” *Phys. Rev. A* **76**, 013803 (2007).
- (7) Jianming Wen, Shengwang Du, and Morton H. Rubin, “Spontaneous Parametric Down-Conversion in a Three-Level System,” *Phys. Rev.* **A76**, 013825 (2007).
- (8) S. N. Goda, S. Sensarn, M. Y. Shverdin, and G. Y. Yin, “Coherent Control of Molecular Modulation,” *App. Phys. Lett.* **91**, 241101 (2007).
- (9) Shengwang Du, Pavel Kolchin, Chinmay Belthangady, G.Y. Yin, S.E. Harris, “Subnatural Linewidth Biphotons with Controllable Temporal Length,” *Phys. Rev. Lett.* **100**, 183603 (May 2008).
- (10) S. E. Harris, “Nonlocal Modulation of Entangled Photons,” *Phys. Rev.* **A78**, 021807 (August 2008).

- (11) Pavel Kolchin, Chinmay Belthangady, Shengwang Du, G.Y. Yin, and S.E. Harris, “Electro-Optic Modulation of Single Photons,” *Phys. Rev. Lett.* **101**, 103601 (2008).
- (12) Shengwang Du, Chinmay Belthangady, Pavel Kolchin, G.Y. Yin, and S.E. Harris, “Observation of Optical precursors at the Biphoton Level,” *Opt Lett*, **33**, 2149 (2008).
- (13) S. Sensarn, Irfan Ali-Khan, G.Y. Yin, and S.E. Harris, “Resonant Sum Frequency Generation with Time-Energy Entangled Photons,” *Phys. Rev. Lett.* **102**, 053602 (2009).
- (14) Chinmay Belthangady, Shengwang Du, Chih-Sung Chuu, G.Y. Yin, and S. E. Harris, “Modulation and Measurement of Time-Energy Entangled Photons,” *Phys. Rev. A* **80**, 031803(R) (2009)
- (15) S. Sensarn, G.Y. Yin, and S.E. Harris, “Observation of Nonlocal Modulation with Entangled Photons,” *Phys. Rev. Lett.* **103**, 163601 (October, 2009).

## B Chirped Crystal Simulation Code

```

clear all;

tic;

format long;
set(0,'defaultaxesfontsize',12);
set(0,'defaulttextfontsize',12);

% Constante
c = 3e8;
hb = 6.83e-34/(2*pi);
eps0 = 1e-9/(36*pi);
ete0 = 377;

% Number of dete points for frequency variable
NW = 1001;

% Define number of points per 2*pi/dw for time domain
NT = 10;

% Temporel limits for plotting correlations
teu1 = -6e-12;
teu2 = 5e-12;
teuh1 = -5e-12;
teuh2 = 5e-12;

% Refractive index of SLT et 40 C (Bruner)
ne_elt = inline(['sqrt(4.502483 + (0.007294 + 3.483933e-8*(40 + 273.15)^2)/((2*pi*3e8./w*1e6).^2 - (0.185087 + 1.607839e-8*(40 + 273.15)^2)^2) + ' ...
'0.073423./((2*pi*3e6./w*1e8).^2 - 0.199595^2) + 0.001./((2*pi*3e8./w*1e8).^2 - 7.99724^2) - 0.02357*(2*pi*3e8./w*1e6).^2'] , 'w');

% Refractive index of CLN et 21 C (Dieter Jundt, JOSAB 14, 3319) 0.4-5 um
no_ln = inline(['sqrt(1 + 2.9804*(2*pi*3e8./w/1e-8).^2./((2*pi*3e8./w/1e-6).^2 - 0.02047) + 0.5961*(2*pi*3e8./w/1e-6).^2./ ' ...
'((2*pi*3e8./w/1e-6).^2 - 0.0666) + 8.9543*(2*pi*3e8./w/1e-8).^2./((2*pi*3e8./w/1e-6).^2 - 416.08))'] , 'w');
no_ln = inline(['sqrt(1 + 2.6734*(2*pi*3e6./w/1e-6).^2./((2*pi*3e6./w/1e-6).^2 - 0.01764) + 1.2290*(2*pi*3e8./w/1e-6).^2./ ' ...
'((2*pi*3e8./w/1e-6).^2 - 0.05914) + 12.614*(2*pi*3e8./w/1e-8).^2./((2*pi*3e8./w/1e-6).^2 - 474.6))'] , 'w');

% Refractive index of 5% MgO doped CLN at 21 C (Dieter Jundt, JOSAB 14, 3319) 0.4-5 um
ne_mgo5ln = inline(['sqrt(1 + 2.4272*(2*pi*3e8./w/1e-8).^2./((2*pi*3e8./w/1e-6).^2 - 0.01478) + 1.4617*(2*pi*3e8./w/1e-6).^2./ ' ...
'((2*pi*3e8./w/1e-6).^2 - 0.05612) + 9.6536*(2*pi*3e8./w/1e-8).^2./((2*pi*3e8./w/1e-6).^2 - 371.218))'] , 'w');
no_mgo5ln = inline(['sqrt(1 + 2.2454*(2*pi*3e6./w/1e-6).^2./((2*pi*3e8./w/1e-6).^2 - 0.01242) + 1.3005*(2*pi*3e6./w/1e-6).^2./ ' ...
'((2*pi*3e8./w/1e-6).^2 - 0.05313) + 6.8972*(2*pi*3e8./w/1e-8).^2./((2*pi*3e8./w/1e-6).^2 - 331.33))'] , 'w');

% Refractive index and nonlinear coefficient for generating crystal
np = ne_elt;
ne = ne_elt;
ni = ne_elt;
d = 12.9e-12; % d33 MgO:SLT

% Refractive index and nonlinear coefficient for summing crystal
nps = ne_ln;
nee = ne_ln;
nie = ne_ln;
de = 25.0e-12; % d33 CLN

% Define pump frequency
wp = 2*pi*c/632.10e-9;

% Define pump power
Pp = 6.9;

% Define signal center frequency and bandwidth
we0 = 2*pi*c/1000e-9;
dw = 2*pi*3e10*300;

% Define the QPM order
qpm_order = 1;

% Define average duty cycle
dcycle = 0.5;

% Define domain edge position noise (standard deviation, fraction of Ldnoise)
% dnoise = 1/sqrt(2)*0.375;
dnoise = 0;

% Define domain width to use for domain edge position noise fraction (set
% to zero to use actual domain width
Ldnoise = 3.5e-5;
% Ldnoise = 0;

% Define minimum step size of mask writer
tmask = 0.0e-5;

% Set to 1 to use low gain assumption
low_gain = 0;

% Define crystal length
L = 0.02;

```

```

% Set to 1 for chirped crystal
chirpedgc = 1;

% Define chirp direction (redleft = 1 for red at z = 0, blue at z = L)
redleft = 0;

% Set to 1 to perform phase compensation
phasecomp = 0;

% Set to 1 to apodize
apodize = 0;

% Set to 1 to filter the output spectrum
filter_main_spec = 0;

% Define relevant frequencies
we_high = we0 + dw/2;
we_low = we0 - dw/2;

we_high_limit = 2*pi*c/603.55e-9;
we_low_limit = 2*pi*c/4500e-9;

% Set frequency domain for 3*dw bandwidth centered at we0
% hut additionally bounded by [we_low_limit, we_high_limit]
w1 = we_low - dw;
w2 = we_high + dw;
if(we_high + dw > we_high_limit) w2 = we_high_limit; end;
if(we_low - dw < we_low_limit) w1 = we_low_limit; end;

% Force lower bound at degeneracy (signal: we > wp/2, idler: wp - we)
if(w1 < wp/2)
    w1 = wp/2;
end

we = linspace(w1, w2, NW);
wi = wp - we;

% Define frequency interval of main spectrum
iwlh = min(find(we > we_low)):max(find(we < we_high));

%%%%%%%%%%%%%%%%%%%%%%%%%%%%%%%%%%%%%%%%%%%%%%%%%%%%%%%%%%%%%%%%%%%%%%%%
% Generating Crystal %
%%%%%%%%%%%%%%%%%%%%%%%%%%%%%%%%%%%%%%%%%%%%%%%%%%%%%%%%%%%%%%%%%%%%%%%%

% Compute k vectors
kp = np(wp)*wp/c;
ke = ns(we).*we/c;
ki = ni(wi).*wi/c;

% Compute phase mismatch
Dk = kp - (ke + ki);

if(chirpedgc == 1)
    % Compute chirp rate
    if(redleft == 1)
        Dk0 = epline(we, Dk, we_low);
        DkL = epline(we, Dk, we_high);
    else
        Dk0 = epline(we, Dk, we_high);
        DkL = epline(we, Dk, we_low);
    end
    zeta = -(DkL - Dk0)/L;

    % Compute phase matching positions for linear k-vector chirp
    zpm = L + (DkL - Dk(iwlh))/zeta;
else
    Dk0 = epline(we, Dk, we0);
    zeta = 0;
end

% Generate vector of domain lengths
disp(sprintf('\nGenerating vector of domain lengths (generating crystal)...'));

% Define chirping function (poling period as a function of z)
z0 = linspace(0, L, 1000);

% Calculate group velocities
vgs = der(we, ke, 1);
vgi = der(wi, ki, 1);
vgr = 1./(1./vge - 1./vgi);

if(chirpedgc == 1 && phasecomp == 1)
    % Store uncompensated phase matching position vector
    zpm_orig = zpm;

    % Compute approximate relative (signal - idler) group delay
    dphi_ep = (L - zpm_orig)./vgr(iwlh);

    % Remove third order dispersion
    %P = polyfit(we(iwlh) - we0, dphi_ep, 2);
    %dphi_sp_pc = dphi_ep - P(1)*(we(iwlh) - we0).^2;

```



```

% Remove fifth order dispersion
%P = polyfit(ws(iwlh) - ws0, dphi_sp, 4);
%dphi_sp_pc = dphi_sp - P(1)*(ws(iwlh) - ws0).^4;

% Force linear chirp
%dphi_sp_pc = (dphi_sp(end) - dphi_sp(1))/(ws_high - ws_low)*(ws(iwlh) - ws_low) + dphi_sp(1);

% Force zero 5th and higher order dispersion
%P = polyfit(ws(iwlh) - ws0, dphi_sp, 3);
%dphi_sp_pc = polyval(P, ws(iwlh) - ws0);

% Force zero 3rd and higher order dispersion
%P = polyfit(ws(iwlh) - ws0, dphi_sp, 1);
%dphi_sp_pc = polyval(P, ws(iwlh) - ws0);

% Force zero 4th and higher dispersion and fix T00/G00 ratio
P = polyfit(ws(iwlh) - ws0, dphi_sp, 2);
P(1) = 1/2*(P(2)*359.6/235.8*1e-15); % 2*P(1) = T00, P(2) = G00, ratio used here is for fused silica at 966.2 nm
dphi_sp_pc = polyval(P, ws(iwlh) - ws0);

% Ensure that pairs phase matched at the output of the crystal have zero
% relative group delay (this fixes zpm at L for those pairs)
if(redshift == 1)
    dphi_sp_pc = dphi_sp_pc - spline(ws(iwlh), dphi_sp_pc, ws_high);
else
    dphi_sp_pc = dphi_sp_pc - splines(ws(iwlh), dphi_sp_pc, ws_low);
end

% Compute chirping function
zpm = L - vgr(iwlh).*dphi_sp_pc;
pp = 2*pi./splines(zpm, Dk(iwlh), z0);
else
    pp = 2*pi./(Dk0 - zsta*z0);
end

if(tmask == 0)
    % Ideal mask writer
    Ld = [];
    z = 0;
    while(z < L)
        dz = interp1(z0, pp, z)*qpm_order*dcycle;
        dcycle = 1 - dcycle;
        Ld = [Ld dz];
        z = z + dz;
    end
else
    % Non-ideal mask writer
    z = 0;
    zm = 0;
    zdr = [];
    while(zm < L)
        dz = interp1(z0, pp, z)*qpm_order*dcycle;
        dcycle = 1 - dcycle;
        z = z + dz;
        zm = zm + round(dz/tmask)*tmask;
        if(z - zm > tmask/2)
            zm = zm + tmask;
        else
            if(z - zm < -tmask/2)
                zm = zm - tmask;
            end
        end
        zdr = [zdr zm];
        z = z + dz;
    end
    Ld = diff([0 zdr]);
end

% Add domain noise
% Form a vector of the positions of the right edges of each domain
zdr = cumsum(Ld);
% Perturb these edges
if(Ldnoise == 0)
    for ii = 1:length(Ld)
        zdr(ii) = zdr(ii) + dnoise*Ld(ii)*sqrt(-2*log(rand))*cos(2*pi*rand);
    end
else
    for ii = 1:length(Ld)
        zdr(ii) = zdr(ii) + dnoise*Ldnoise*sqrt(-2*log(rand))*cos(2*pi*rand);
    end
end

% Reconstruct domain length vector
Ld = diff([0 zdr]);

% Fix crystal length
L = sum(Ld);

% Perform apodizing
apodmask = ones(1, length(Ld));
if(chirpedgc == 1 && apodize == 1)

```

```

% Define apodization function in polynomial form
% The apodization function should be the probability that a reversal is
% NOT removed.
% Papod = [-5.069304641499887e-45 2.849462981101168e-29 -5.116363656404832e-14 29.64933346525240];
% fspod = spline(zpm, polyval(Papod, ws), zdr);

% Assume all frequency components confocally focused
Ap = 2*pi*c/wp*L/(4*np(wp));
As = 2*pi*c./ws*L./(4*ns(ws));
Ai = 2*pi*c./wi*L./(4*ni(wi));

etap = ets0/np(wp);
etas = sts0./ns(ws);
stai = sts0./ni(wi);

% Compute gain constant
kappa = eps0*d*sqrt(8*hb*wp*ws.*wi*etap.*etas.*etai*Ap.*As.*Ai ...
    ./ (Ap*As + Ap*Ai + As.*Ai).^2);

fspod = kappa(iwlh(snd))./kappa(iwlh);

% Compute apodization function (probability vs. z that a reversal is
% NOT removed)
fspod = spline(zpm, fspod, zdr);
winf = 3;
win = (1 - cos(2*pi*(1:round(length(fspod)/winf))/(length(fspod)/winf)))/2;
win = [win(1:round(length(win)/2)) ones(1, length(fspod) - length(win)) win(round(length(win)/2)+1:end)];
% fspod = fspod.*win;

% Fix erroneous downturn due to polynomial end behavior
% fspod(find(fspod == max(fspod)):end) = 1;

% Compute target function to compare against when integrating
% normalized nonlinearity
target = cumsimp(zdr, fspod);

% Compute period widths
if(mod(length(Ld), 2) == 0)
    Lp = Ld(1:2:end) + Ld(2:2:end);
else
    Lp = Ld(1:2:end-1) + Ld(2:2:end);
end

% Compute period mask (0 for no reversal, 1 for reversal)
prmask = ones(1, floor(length(Ld)/2));

for ii = 1:length(Lp)
    if(sum(Lp(1:ii).*prmask(1:ii)) > target(ii*2 - 1))
        prmask(ii) = 0;
    end
end

spodmask(2:2:end) = 2*prmask - 1;
end

%%%%%%%%%%%%%%%%%%%%%%%%%%%%%%%%%%%%%%%%%%%%%%%%%%%%%%%%%%%%%%%%%%%%%%%%
% Summing Crystal %
%%%%%%%%%%%%%%%%%%%%%%%%%%%%%%%%%%%%%%%%%%%%%%%%%%%%%%%%%%%%%%%%%%%%%%%%

% Compute k vectors
kps = nps(wp)*wp/c;
kss = nss(ws).*ws/c;
kis = nis(wi).*wi/c;

% Compute phase mismatch
Dks = kps - (kss + kie);

% Compute phase mismatch at center frequency
Dks0 = spline(ws, Dks, ws0);

% Modify crystal length as necessary to achieve a cross match correlation
Ls = is-3;

% Generate vector of domain lengths
disp(sprintf('Generating vector of domain lengths (summing crystal)...'));

% Define chirping function (poling period as a function of z)
z0 = linspace(0, Ls, 1000);
pp = ones(1, length(z0))*2*pi./Dks0;

if(tmask == 0)
    % Ideal mask writer
    Lds = [];
    z = 0;
    while(z < Ls)
        dz = interp1(z0, pp, z)*qpm_order*dcycle;
        dycyls = 1 - dcycle;
        Lds = [Lds dz];
        z = z + dz;
    end
end
slss

```

```

% Non-ideal mask writer
z = 0;
zm = 0;
zdrs = [];
while(zm < Ls)
    dz = interp(z0, pp, z)*qpm_order*dcycle;
    dcycle = 1 - dcycle;
    z = z + dz;
    zm = zm + round(dz/tmask)*tmask;
    if(z - zm > tmask/2)
        zm = zm + tmask;
    else
        if(z - zm < -tmask/2)
            zm = zm - tmask;
        end
    end
    zdrs = [zdrs zm];
end
Lds = diff([0 zdrs]);

% Add domain noise
% Form a vector of the positions of the right edges of each domain
zdrs = cumsum(Lds);
% Perturb these edges
if(Ldnnoise == 0)
    for i1 = 1:length(Lds)
        zdrs(i1) = zdrs(i1) + dnoiee*Lds(i1)*sqrt(-2*log(rand))*cos(2*pi*rand);
    end
else
    for i1 = 1:length(Lds)
        zdrs(i1) = zdrs(i1) + dnoise*Ldnnoise*sqrt(-2*log(rand))*cos(2*pi*rand);
    end
end

% Reconstruct domain length vector
Lds = diff([0 zdrs]);

% Fix crystal length
Ls = sum(Lds);

%%%%%%%%%%%%%%%%%%%%%%%%%%%%%%%%%%%%%%%%%%%%%%%%%%%%%%%%%%%%%%%%%%%%%%%%%%%%%%
% Compute ABCD Matrix: Generating Crystal %
%%%%%%%%%%%%%%%%%%%%%%%%%%%%%%%%%%%%%%%%%%%%%%%%%%%%%%%%%%%%%%%%%%%%%%%%%%%%%%

% Compute eqrt pump photons/s
bp = sqrt(Pp/(hb*wp));

% Assumes all frequency components confocally focused
Ap = 2*pi*c/wp*L/(4*np(wp));
Ae = 2*pi*c/ws*L/(4*ns(ws));
Ai = 2*pi*c/wi*L/(4*ni(wi));

etap = eta0/wp(wp);
etas = eta0/ws(ws);
etei = eta0/wi(wi);

% Compute gain constant
kappa = epa0*sqrt(8*hb*wp*ws.*wi*etap.*etas.*etei*Ap.*Ae.*Ai ...
    ./ (Ap.*Ae + Ap.*Ai + Ae.*Ai).^2);

% Compute overlap factors separately for reference
ge = 2*Ap.*Ai./ (Ap.*Ae + Ap.*Ai + Ae.*Ai);
gi = 2*Ap.*Ae./ (Ap.*Ae + Ap.*Ai + Ae.*Ai);
gp = 2*Ae.*Ai./ (Ap.*Ae + Ap.*Ai + Ae.*Ai);

disp(sprintf('Computing ABCD matrix (generating crystal)...'));

A1 = zeros(1, length(ws));
B1 = zeros(1, length(ws));
C1 = zeros(1, length(ws));
D1 = zeros(1, length(ws));
zdl = cumsum([0 Ld(1:end-1)]);
sgnd = 2*mod(1:length(Ld), 2) - 1;
sgnd = sgnd.*spodmask;
if(low_gain == 1)
    % Low gain assumption: simply integrate signal and idler propagation
    % equations independently
    for i1 = 1:length(ws)
        M12 = sum(sgnd*kappa(i1)*bp/Dk(i1).*(exp(i*Dk(i1)*(zdl + Ld)) - exp(i*Dk(i1)*zdl)));
        A1(i1) = exp(i*ks(i1)*L);
        B1(i1) = M12*exp(i*ks(i1)*L);
        C1(i1) = conj(M12)*exp(-i*ki(i1)*L);
        D1(i1) = exp(-i*ki(i1)*L);
    end
else
    % High gain: integrate coupled equations for each eleb iteratively
    % Note that only the sign of kappa changes domain-to-domain; e = const
    s = sqrt(bp^2*kappa.^2 - Dk.^2/4);
    A1i = exp(i*Dk*Ld(1)/2).*(cosh(s*Ld(1)) - i*Dk./(2*s).*sinh(s*Ld(1)));
    B1i = i*bp*kappa./s.*exp(i*Dk*(zdl(1) + Ld(1)/2)).*sinh(s*Ld(1));

```

```

for i1 = 2:length(Ld)
    A2i = exp(1*Dk*Ld(i1)/2).*(cosh(s*Ld(i1)) - i*Dk./(2*s).*sinh(s*Ld(i1)));
    B2i = i*bp*sgnd(i1)*kappa./s.*exp(i*Dk*(zdl(i1) + Ld(i1)/2)).*sinh(s*Ld(i1));

    A1in = A1i.*A2i + conj(B1i).*B2i;
    B1in = B1i.*A2i + conj(A1i).*B2i;

    A1i = A1in;
    B1i = B1in;
end
A1 = A1i.*exp(i*ks*L);
B1 = B1i.*exp(i*ks*L);
C1 = conj(B1i).*exp(-i*ki*L);
D1 = conj(A1i).*exp(-i*ki*L);
end

% Apply a band pass filter to the main spectrum
if(filter_main_spec == 1)
    HF = ones(1, length(ws)).*(ws > ws_low - dw/4 & ws < ws_high + dw/4);
    A1 = A1.*HF;
    B1 = B1.*HF;
    C1 = C1.*conj(HF);
    D1 = D1.*conj(HF);
end

%%%%%%%%%%%%%%%%%%%%%%%%%%%%%%%%%%%%%%%%%%%%%%%%%%%%%%%%%%%%%%%%%%%%%%%%%%%%%%
% Computes Transfer Function: Summing Crystal %
%%%%%%%%%%%%%%%%%%%%%%%%%%%%%%%%%%%%%%%%%%%%%%%%%%%%%%%%%%%%%%%%%%%%%%%%%%%%%%

% Assumes all frequency components confocally focused
Aps = 2*pi*c/wp*Lv/(4*nps(wp));
Ass = 2*pi*c./ws*Lv/(4*nse(ws));
Ais = 2*pi*c./wi*Lv/(4*nis(wi));

etaps = ets0/nps(wp);
staps = sts0./nse(ws);
etais = ets0./nis(wi);

% Compute gain constant
kappa = eps0*ds*sqrt(8*hb*wp*ws*wi*etaps.*staps.*etais*Aps.*Ass.*Ais ...
    ./((Aps*Ass + Aps*Ais + Ass.*Ais).^2);

% Compute overlap factors separately for reference
gs = 2*Aps.*Ais./((Aps.*Ass + Aps.*Ais + Ass.*Ais));
gis = 2*Aps.*Ass./((Aps.*Ass + Aps.*Ais + Ass.*Ais));
gps = 2*Ass.*Ais./((Aps.*Ass + Aps.*Ais + Ass.*Ais));

disp(sprintf('Computing transfer function (summing crystal)...'));

ESP = zeros(1, length(ws));
zdl = cumsum([0 Lds(1:end-1)]);
sgnds = 2*mod(1:length(Lds), 2) - 1;
for i1 = 1:length(ws)
    M12 = sum(sgnds*kappa(s(i1)/Dks(i1)).*(exp(-i*Dks(i1)*zdl) - exp(-i*Dks(i1)*(zdl + Lds))));
    ESP(i1) = M12*exp(i*kps*L);
end

%%%%%%%%%%%%%%%%%%%%%%%%%%%%%%%%%%%%%%%%%%%%%%%%%%%%%%%%%%%%%%%%%%%%%%%%%%%%%%
% PSD and Phase %
%%%%%%%%%%%%%%%%%%%%%%%%%%%%%%%%%%%%%%%%%%%%%%%%%%%%%%%%%%%%%%%%%%%%%%%%%%%%%%

% Compute signal power spectral density
Ss1 = 1/(2*pi)*abs(B1).^2;

% Calculate paired generation rates
R = simp(ws, Ss1);

% Plot signal power spectral density
figure;
plot(ws, Ss1, 'k-');
title(sprintf('Signal power spectral density (R = %.3e (s^{-1}))', R));
xlabel('\omega (rad/s)');
ylabel('S_s(\omega) (s^{-1}/rad)');

% Compute biphoton phase (signal + idler), relative delay, and GDD
phi = unwrap(angles(A1.*conj(C1)), pi);
dphi = der(phi, ws, 1);
d2phi = der(phi, ws, 2);

% Plot phase, delay, and GDD
figure;
subplot(311);
plot(ws(iwlh), phi(iwlh), 'k-');
axis tight;
title('Biphoton phase');
xlabel('\omega (rad/s)');
ylabel('Phase (rad)');
subplot(312);
plot(ws(iwlh), dphi(iwlh), 'k-');
axis tight;
title('Signal/idler relative group delay');

```

```

xlabel('\omega (rad/s)');
ylabel('Group delay (s)');
subplot(313);
plot(ws(iwlh), d2phi(iwlh), 'k-');
axis tight;
title('Biphoton GDD');
xlabel('\omega (rad/s)');
ylabel('GDD (s^2/rad)');

% Calculate average GDD and TDD based on nth order fit to phase in significant
% frequency region
P = polyfit(ws(iwlh) - ws0, phi(iwlh), 3);
GDD = 2*P(2);
TDD = 6*P(1);
%DSD = 120*P(1);

% Show fit in phase plot
%subplot(311);
%hold on;
%plot(ws(iwlh), polyval(P, ws(iwlh) - wsD), 'k--');

%%%%%%%%%%%%%%%%%%%%%%%%%%%%%%%%%%%%%%%%%%%%%%%%%%%%%%%%%%%%%%%%%%%%%%%%%%%%%%
% Specify Optical System and Compressor %
%%%%%%%%%%%%%%%%%%%%%%%%%%%%%%%%%%%%%%%%%%%%%%%%%%%%%%%%%%%%%%%%%%%%%%%%%%%%%%

% Signal optical system transfer function
H1 = 1;
% Idler optical system transfer function
G1 = 1;

% Compressor transfer function (signal path)
%HC = 1;
%HC = exp(-i*phi);

% Femtosecond costing
phic = -4.64e-42*ws.^3 + 2.552e-26*ws.^2 - 0.00225*sin(3.3333e-13*ws);
phic = phic - polyval(polyfit(ws, phic, 1), ws); % Remove time delay
phic = phic*i3; % Number of bounces
HC = exp(i*phic);

% Compressor transfer function (idler path)
GC = 1;

%%%%%%%%%%%%%%%%%%%%%%%%%%%%%%%%%%%%%%%%%%%%%%%%%%%%%%%%%%%%%%%%%%%%%%%%%%%%%%
% Uncompressed Correlations %
%%%%%%%%%%%%%%%%%%%%%%%%%%%%%%%%%%%%%%%%%%%%%%%%%%%%%%%%%%%%%%%%%%%%%%%%%%%%%%

disp(sprintf('Computing uncompressed correlations...'));

% Specify ABCD coefficients incident on the summing crystal (i.e. after the
% optical system)
A2 = A1.*H1;
B2 = B1.*H1;
C2 = C1.*conj(G1);
D2 = D1.*conj(G1);

% Use Fourier transform to compute wavefunction
Ws = FTCreate(ws(2) - ws(1), 2*pi/dw/NT);
tsu = FTDomain(Ws);

% Compute the wavefunction without summing
psi2 = 1/(2*pi)*exp(i*(vp - wsD)*tsu).*IFTC(interpi(ws - wsD, A2.*conj(C2), Ws, 'nearest', D), Ws);
fhi = abs(psi2).^2;

% Compute the uncompressed SFG rate
Rmq = 1/(4*pi^2).*abs(IFTC(interpi(ws - wsD, A2.*conj(C2).*ESP, Ws, 'nearest', 0), Ws)).^2;

% Plot wavefunction amplitude squared
figure;
plot(tau, fhi, 'k-');
V = axis([tsu1 tsu2 V(3) V(4)]);
title('Biphoton intensity (uncompressed) |<a_s(t) a_i(t - \tau)|^2');
xlabel('\tau (s)');

% Plot quantum sum photon rates for the non-chirped crystal
figure;
plot(tau, Rmq, 'k-', tau, fhi/max(fhi)*max(Rmq), 'k--');
V = axis([tsu1 tsu2 V(3) V(4)]);
title(sprintf('Non-chirped quantum sum photon rate (uncompressed, L_s = %.3f (mm))', Ls/1e-3));
xlabel('\tau (s)');
ylabel('R_{mq} (s^{-1})');
legend('R_{mq}', '\propto |<a_s(t) a_i(t - \tau)|^2', 'Location', 'Best');

%%%%%%%%%%%%%%%%%%%%%%%%%%%%%%%%%%%%%%%%%%%%%%%%%%%%%%%%%%%%%%%%%%%%%%%%%%%%%%
% Compressed Correlations %
%%%%%%%%%%%%%%%%%%%%%%%%%%%%%%%%%%%%%%%%%%%%%%%%%%%%%%%%%%%%%%%%%%%%%%%%%%%%%%

disp(sprintf('Computing compressed correlations...'));

% Specify ABCD coefficients incident on the summing crystal (i.e. after the
% optical system)

```



```

A2 = A1.*H1.*HC;
B2 = B1.*H1.*HC;
C2 = C1.*conj(G1).*conj(GC);
D2 = D1.*conj(G1).*conj(GC);

% Computes the wsvsfunction without summing
psi2h = 1/(2*pi)*exp(i*(wp - wsD)*tau).*IFTCP(intsrp1(ws - wsD, A2.*conj(C2), Ws, 'nearest', 0), We);
fbih = abs(psi2h).^2;

% Compute the uncompressed SFG rate
Rmqh = 1/(4*pi^2).*subs(IFTCP(interp1(ws - ws0, A2.*conj(C2).*ESP, Ws, 'nearest', D), We)).^2;

% Plot wavsfunction amplitude squared
figure;
plot(tau, fbih, 'k-');
V = axis; axis([tsuh1 tsuh2 V(3) V(4)]);
title('Biphoton intensity (compressed) |s_s(t) a_i(t - \tsu)|^2');
xlabel('\tau (s)');

% Plot quantum sum photon rsts for the non-chirped crystal
figure;
plot(tau, Rmqh, 'k-', tsu, fbih/max(fbih)*max(Rmqh), 'k--');
V = axis; axis([tsuh1 tsuh2 V(3) V(4)]);
title(sprintf('Non-chirped quantum sum photon rsts (compressed, L_s = %.3f (nm))', Ls/1e-3));
xlabel('\tau (s)');
ylabel('R_{mq} (s^{-1})');
legend('R_{mq}', '\propto |s_s(t) a_i(t - \tsu)|^2', 'Location', 'Best');

% Combine plots onto one figure
figure;
subplot(221);
plot(2*pi*c./ws*1e9, Ss1, 'k-');
V = axis; axis([2*pi*c./ws(snd)*1e9 2*pi*c./ws(1)*1e9 V(3) V(4)]);
title('Signal power spectral density; sprintf('R = %.3e (s^{-1})', R));
xlabel('\lambda (nm)');
ylabel('S_s(\lambda) (s^{-1}/rad)');
subplot(222);
plot(2*pi*c./ws(iwlh)*1e9, phi(iwlh), 'k-');
axis tight;
title('Biphoton phase spectrum');
xlabel('\lambda (nm)');
ylabel('Phase (rad)');
subplot(223);
plot(tau, Rmq, 'k-', tsu, fbih/max(fbih)*max(Rmq), 'k--');
V = axis; axis([tsu1 tsu2 V(3) V(4)]);
title('Quantum SFG rsts; sprintf('uncompressed, L_s = %.3f (nm))', Ls/1e-3));
xlabel('\tau (s)');
ylabel('R_{mq} (s^{-1})');
leg = legend('R_{mq}', '\propto |s_s(t) a_i(t - \tau)|^2', 'Location', 'Best');
set(leg, 'FontSize', 1D);
subplot(224);
plot(tau, Rmqh, 'k-', tsu, fbih/max(fbih)*max(Rmqh), 'k--');
V = axis; axis([tsuh1 tsuh2 V(3) V(4)]);
title('Quantum SFG rate; sprintf('compressed, L_s = %.3f (nm))', Ls/1e-3));
xlabel('\tau (s)');
ylabel('R_{mq} (s^{-1})');
leg = legend('R_{mq}', '\propto |s_s(t) a_i(t - \tsu)|^2', 'Location', 'Best');
set(leg, 'FontSize', 1D);

% Report
disp(sprintf('\nPaired rsts: %.3e (s^{-1})', R));
disp(sprintf('GDD (based on order (%.0f) fit): %.3e (fs^2)', length(P) - 1, GDD/1e-30));
disp(sprintf('TDD (based on order (%.0f) fit): %.3e (fs^3)', length(P) - 1, TOD/1e-45));
disp(sprintf('Non-chirped summing crystal length: %.3f (nm)', Ls/1e-3));

if(chirpedgc == 1)
    disp(sprintf('Poling period (generating crystal): Red: %.4f (um), Blue: %.4f (um)', ...
        2*pi/spline(ws, Dk, ws_low)*qpm_order/1e-6, 2*pi/spline(ws, Dk, ws_high)*qpm_order/1e-6));
else
    disp(sprintf('Poling period (generating crystal): %.4f (um)', 2*pi./Dk0*qpm_order/1e-6));
end
disp(sprintf('Poling period (summing crystal): %.3f (um)', 2*pi./DksD*qpm_order/1e-6));

% Display poling periods for SLT at 25 C
TexpanDSL = 1 + 1.6e-5*(40 - 25) + 7e-9*(40 - 25)^2;
if(chirpedgc == 1)
    disp(sprintf('Poling period (generating crystal) at 25 C (SLT): Red: %.4f (um), Blue: %.4f (um)', ...
        2*pi/spline(ws, Dk, ws_low)/TexpanDSL*qpm_order/1e-6, 2*pi/spline(ws, Dk, ws_high)/TexpanDSL*qpm_order/1e-6));
else
    disp(sprintf('Poling period (generating crystal) at 25 C (SLT): %.4f (um)', 2*pi./Dk0/TexpanDSL*qpm_order/1e-6));
end

% Display poling periods for CLN at 25 C
TexpanCLN = 1 + 14.8e-6;
disp(sprintf('Poling period (summing crystal) at 25 C (CLN): %.4f (um)', 2*pi./Dk0/TexpanCLN*qpm_order/1e-6));

elapsedtime = toc;
disp(sprintf('\nElapsed time: %.1f (s)', elapsedtime));

```

## C Chapter 4 of Kolchin's Dissertation

4.1	Theory of paired photon generation . . . . .	30
4.2	Heisenberg-Langevin description . . . . .	32
4.3	Solution of Coupled Equations . . . . .	34
4.4	Characteristics of generated photons . . . . .	36
4.5	Ideal Spontaneous Parametric Down Converter . . . . .	39
4.6	EIT based Paired Photon Generator . . . . .	41
4.7	Mathematical Apparatus . . . . .	51

---

The original dissertation pp. 29 - 56 are included after this page.

## Chapter 4

# Theory of EIT based Paired Photon Generation

Correlated and entangled photon pairs are widely used in quantum communication, quantum cryptography [31] and quantum imaging [32, 33]. These photon pairs are usually produced via spontaneous parametric down conversion in nonlinear crystals. A few years ago a new approach to the generation of paired photons has been experimentally demonstrated by two groups, both use electromagnetically induced transparency (EIT) to generate paired photons in an otherwise opaque atomic medium. Working with hot atoms, Lukin and colleagues have demonstrated correlation between generated pulses of light, as well as storage and delayed extraction [34]. Working with a MOT, Kimble and colleagues have shown the generation of nonclassical photon pairs with a programmable delay [35]. Recently, the Harris research group at Stanford has demonstrated generation and rudimentary waveform control of narrow band biphotons [36]. More recently, Kolchin and colleagues have shown paired photon generation with a single pump beam in a right angle geometry and paired photon generation in the ensemble of cold two-level atoms [37]. A long coherence length and a controllable bandwidth of the generated paired photons are the advantages of the new approach, which might be useful for such applications as long distance quantum

communication [38] as well as biphoton waveform control and shaping <sup>1</sup>.

## 4.1 Theory of paired photon generation

This chapter describes the theory of correlated paired photon generation in a collection of double  $\Lambda$ -type atoms [39]. Using the Heisenberg-Langevin method we evaluate and analyze spectral characteristics of the generated Stokes and anti-Stokes photons and their time-correlation properties. Of importance, we predict the regime when the correlation time of generated photons is determined by the group delay caused by EIT. This theoretical prediction as well as some theoretical aspects of this work has been outlined in Ref. [36]. The complete theoretical treatment of paired photon generation with and without the approximation, that the atomic population remains in the ground state, has been given in Ref. [39].

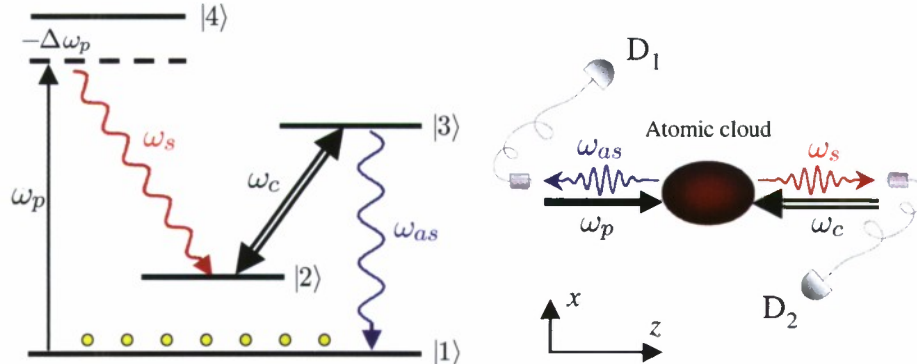


Figure 4.1: Energy level diagram and schematic for spontaneous backward-wave paired photon generation in an atomic cloud formed by double- $\Lambda$  type atoms. In the presence of the pump and coupling lasers phase-matched, counter-propagating Stokes and anti-Stokes photons are generated into opposite directions.

The schematic of the process considered here is shown in Fig. 5.7. In the presence two cw beams termed as the pump and coupling lasers with frequencies  $\omega_p$  and  $\omega_c$ ,

<sup>1</sup>In a right-angle geometry, where Stokes and anti-Stokes photons are generated and collected at right angles from the direction of the pump-coupling axis, applying the absorption mask on the pump beam allows us to create a biphoton with a prescribed waveform.

paired spontaneous photons termed as Stokes and anti-Stokes are generated in the atomic cloud and propagate in opposite directions along the  $z$  axis. In order to keep the parametric gain small we choose the pump beam to be weak and detuned from the resonance transition  $|1\rangle \rightarrow |4\rangle$ . The intense coupling beam is tuned to resonance with the  $|2\rangle \rightarrow |3\rangle$  transition to enhance the atom-field interaction and provide EIT for the generated anti-Stokes photon. Under such conditions we expect a small fraction of the atomic population to be in the excited states while most of it remains in the ground state  $|1\rangle$ . The frequencies of the generated photons obey the energy conservation  $\omega_s + \omega_{as} = \omega_p + \omega_c$ . In the presence of EIT the anti-Stokes photon escapes out of the atomic cloud with very slow group velocity.

We note the connection to earlier work: Two-photon entanglement in type-II SPDC has been analyzed [40]. The possibility of quantum correlated and squeezed fields in backward wave EIT system has been predicted [41] and large parametric gain and oscillations have been observed [42]. Control of single photons has been discussed [43]. We also note the early studies on double- $\Lambda$  atomic systems [44].

In this chapter we review and discuss in detail the system dynamics putting emphasis on the influence of the EIT window on paired photon generation bandwidth. We show that at low parametric gain the atomic system can operate in two different regimes. In the first regime, where the group delay is small, the intensity correlation function shows Rabi oscillations. In the second regime, where the optical depth of the atomic sample and the group delay are large, phase-matching becomes the dominant process that controls the shape of the intensity correlation function. We examine the conditions required for the system to operate in the oscillatory and group delay regimes and discuss corresponding Stokes and anti-Stokes spectral generation rates. In particular, we predict that the group delay regime requires the optical depth much higher than 10. This point has been missed in our earlier publication [36].

We also extend our theoretical treatment of paired photon generation to go beyond the ground state approximation. This allows us to properly include and analyze the effect of Langevin noise fluctuation on the atomic system and solve the problem of its return to the ground state after the emission of Stokes and anti-Stokes photon pairs. We also address the important questions: 1) “What are the effects of the optical



thickness of the atomic sample on paired and single photon generation?” 2) “Does every Stokes photon have its paired anti-Stokes photon?”

We introduce and derive the biphoton wavefunction taking into account Langevin noise terms. We also derive and discuss the relation of the Stokes photon count rate to the classical gain coefficient in the Stokes channel.

## 4.2 Heisenberg-Langevin description of paired photon generation

We consider a collection of identical double  $\Lambda$ -type atoms uniformly distributed within a pencil-shaped volume with cross section  $S$  and length  $L$ . We assume that the atomic sample is optically thin in the transverse direction, so that there is no radiation trapping effect in this direction. No restrictions are imposed on the optical thickness of the atomic sample in the  $z$  direction. We also assume that the pump and the coupling beams counter-propagate undepleted through the atomic medium. Under these assumptions we consider propagation of a single transverse spatial mode of radiation along the  $z$  axis. The pump and coupling laser beams are treated as classical quantities and their interaction with the medium is described semi-classically. In order to allow for the spontaneous initiation of the parametric fluorescence process, the generated weak Stokes and anti-Stokes fields are described by quantum-mechanical operators, in slowly varying envelope approximation:

$$\hat{E}_j^{(+)} = \sqrt{\frac{\hbar\omega_j}{2\epsilon_0 V}} \hat{a}_j(z, t) \exp\left(-i\omega_j t + i\vec{k}_j \cdot \vec{z}\right), \quad (4.1)$$

where subscript  $j$  denotes either Stokes or anti-Stokes photon,  $\omega_s = \omega_4 - \omega_2 + \Delta\omega_{14}$ ,  $\omega_{as} = \omega_3 - \omega_1$ ,  $V = L \times S$  is the interaction volume.

Adopting the notations of Lukin and Fleischhauer [45, 46], in the rotating wave

approximation we write the interaction Hamiltonian in continuous form as

$$\begin{aligned} \hat{V} = -\frac{\hbar N}{L} \int_0^L dz \Big( & \Delta\omega_{14}\tilde{\sigma}_{44}(z, t) + g_{31}\hat{a}_{as}(z, t)\tilde{\sigma}_{31}(z, t) \\ & + \frac{\Omega_c}{2}\tilde{\sigma}_{32}(z, t) + \frac{\Omega_p}{2}\tilde{\sigma}_{41}(z, t) + g_{42}\hat{a}_s(z, t)\tilde{\sigma}_{42}(z, t) + h.c. \Big), \end{aligned} \quad (4.2)$$

where  $\tilde{\sigma}_{jk}(z, t)$  are the collective slowly varying atomic operators, defined in the Appendix 4.7.1,  $N$  is the total number of atoms in the atomic ensemble,  $\Delta\omega_{14}$  is the detuning of the pump laser from the  $|1\rangle \rightarrow |4\rangle$  transition,  $\Omega_c = \frac{2\wp_{23}E_c}{\hbar}$ ,  $\Omega_p = \frac{2\wp_{41}E_p}{\hbar}$  are pump and coupling laser Rabi frequencies with  $E_p, E_c$  as the complex amplitudes of the electric fields,  $g_s = \frac{\wp_{42}\mathcal{E}_s}{\hbar}$  and  $g_{as} = \frac{\wp_{31}\mathcal{E}_{as}}{\hbar}$  are the coupling constants with  $\wp_{jk}$  as the dipole moment for the  $|j\rangle \rightarrow |k\rangle$  transition and  $\mathcal{E}_j = \sqrt{\frac{\hbar\omega_j}{2\epsilon_0 V}}$  as the electric field of a single photon.

The propagation of the Stokes and anti-Stokes fields and their interaction with the atoms are described by the set of Maxwell and Heisenberg-Langevin equations. The Heisenberg-Langevin equations are responsible for the atomic evolution:

$$\frac{\partial}{\partial t}\tilde{\sigma}_{jk} = \frac{i}{\hbar}[\hat{V}, \tilde{\sigma}_{jk}] - \gamma_{jk}\tilde{\sigma}_{jk} + r_{jk}^A + \tilde{F}_{jk}, \quad (4.3)$$

where  $\gamma_{jk}$  are the dephasing rates,  $r_{jk}^A$  are the spontaneous emission rates,  $\tilde{F}_{jk}(z, t)$  are the collective atomic  $\delta$ -correlated Langevin noise operators. The full set of the Heisenberg-Langevin equations is shown explicitly in Sec. 4.7.2

The fluctuations of  $\delta$ -correlated collective Langevin noise operators  $\tilde{F}_{jk}(z, t)$  is given by

$$\langle \tilde{F}_{jk}(z, t)\tilde{F}_{j'k'}(z', t') \rangle = \frac{L}{N}\mathcal{D}_{jk,j'k'}(z, t)\delta(t - t')\delta(z - z'), \quad (4.4)$$

where  $\mathcal{D}_{jk,j'k'}$  is a Langevin diffusion coefficient. The derivation of Eq.(4.4) and relevant diffusion coefficients is shown in Sec. 4.7.4.

The evolution of the annihilation  $a_s$  and creation  $a_{as}^\dagger$  operators for the slowly varying Stokes and anti-Stokes fields is described by the coupled propagation equations

$$\begin{aligned} \left( \frac{\partial}{\partial t} + c \frac{\partial}{\partial z} \right) \hat{a}_s(z, t) &= ig_s N \tilde{\sigma}_{24}(z, t) \\ \left( \frac{\partial}{\partial t} - c \frac{\partial}{\partial z} \right) \hat{a}_{as}^\dagger(z, t) &= -ig_{as} N \tilde{\sigma}_{31}(z, t). \end{aligned} \quad (4.5)$$

The following analysis of the system involves calculation of the expected values of quantum field operators and their combinations. We note that in the Heisenberg picture operators evolve and the system is always in its initial state, which in our case corresponds to no Stokes and anti-Stokes input beams at the left and right boundaries.

### 4.3 Solution of Coupled Equations

Due to complexity and nonlinearity it is not possible to obtain an analytic solution for the combined set of the field propagation equations and Heisenberg-Langevin equations. Nevertheless, under the condition that Stokes and anti-Stokes fields are much weaker than the coupling and pump fields, and Stokes and anti-Stokes photon densities are much smaller than the atomic density  $N/V$  [45], the Heisenberg-Langevin equations can be linearized with Stokes  $\hat{a}_s$  and anti-Stokes  $\hat{a}_{as}$  fields as perturbation parameters. The linearization procedure is described in detail in the Appendix 4.7.3.

In order to solve the set of the linearized Heisenberg-Langevin Eq. (4.35) and coupled propagation Eq. (4.5), we first Fourier transform them. Then, extracting the solutions for  $\tilde{\sigma}_{24}(\omega)$ ,  $\tilde{\sigma}_{31}(\omega)$  and substituting them into Fourier transformed Eq.(4.5), we obtain the coupled equations for  $\hat{a}_s(z, \omega)$  and  $\hat{a}_{as}^\dagger(z, -\omega)$  in the form

$$\begin{aligned} \frac{\partial \hat{a}_s}{\partial z} + g_R \hat{a}_s + \kappa_s \hat{a}_{as}^\dagger &= \sum_{\alpha_i} \xi_{\alpha_i}^s \tilde{f}_{\alpha_i} \\ \frac{\partial \hat{a}_{as}^\dagger}{\partial z} + \Gamma_{as} \hat{a}_{as}^\dagger + \kappa_{as} \hat{a}_s &= \sum_{\alpha_i} \xi_{\alpha_i}^{as} \tilde{f}_{\alpha_i} \end{aligned} \quad (4.6)$$

where  $g_R(\omega)$ ,  $\Gamma_{as}(\omega)$  are the Raman gain, EIT profile coefficients respectively,  $\kappa_s(\omega)$  and  $\kappa_{as}(\omega)$  are Stokes and anti-Stokes mode coupling coefficients. In Eq. 4.6  $\tilde{f}_{\alpha_i}(z, \omega)$  are the renormalized Langevin noise operators:  $\tilde{f}_{\alpha_i}(z, \omega) = \sqrt{N/c} \times \tilde{F}_{\alpha_i}(z, \omega)$ . The sum is taken over the relevant Langevin noise operators  $\{\tilde{f}_{21}, \tilde{f}_{24}, \tilde{f}_{31}, \tilde{f}_{34}\}$ .

The general solution of Eq. (4.6) can be written as

$$\begin{pmatrix} \hat{a}_s(L) \\ \hat{a}_{as}^\dagger(L) \end{pmatrix} = e^{-\tilde{M}L} \begin{pmatrix} \hat{a}_s(0) \\ \hat{a}_{as}^\dagger(0) \end{pmatrix} + \sum_{\alpha_i} \int_0^L dz e^{\tilde{M}(z-L)} \begin{pmatrix} \xi_{\alpha_i}^s \\ \xi_{\alpha_i}^{as} \end{pmatrix} \tilde{f}_{\alpha_i} \quad (4.7)$$

where  $\tilde{M} = \begin{pmatrix} g_R & \kappa_s \\ \kappa_{as} & \Gamma \end{pmatrix}$

For the following derivation, let us define the coefficients of matrix  $e^{-\tilde{M}L}$  as

$$\begin{pmatrix} A_1 & B_1 \\ C_1 & D_1 \end{pmatrix} = e^{-\tilde{M}L} \quad (4.8)$$

Due to the linearity of Eq. (4.7), the unknown variables  $\hat{a}_s^\dagger(L)$  and  $\hat{a}_{as}(0)$  of the backward wave problem can be written as a linear combination of the initial boundary values and the noise terms:

$$\begin{pmatrix} \hat{a}_s(L) \\ \hat{a}_{as}^\dagger(0) \end{pmatrix} = \begin{pmatrix} A & B \\ C & D \end{pmatrix} \begin{pmatrix} \hat{a}_s(0) \\ \hat{a}_{as}^\dagger(L) \end{pmatrix} + \sum_{\alpha_i} \int_0^L dz \begin{pmatrix} P_{\alpha_i} \\ Q_{\alpha_i} \end{pmatrix} \tilde{f}_{\alpha_i} \quad (4.9)$$

where

$$\begin{pmatrix} A & B \\ C & D \end{pmatrix} = \begin{pmatrix} A_1 - \frac{B_1 C_1}{D_1} & \frac{B_1}{D_1} \\ -\frac{C_1}{D_1} & \frac{1}{D_1} \end{pmatrix} \quad (4.10)$$

$$\begin{pmatrix} P_{\alpha_i} \\ Q_{\alpha_i} \end{pmatrix} = \begin{pmatrix} 1 & -\frac{B_1}{D_1} \\ 0 & -\frac{1}{D_1} \end{pmatrix} e^{\tilde{M}(z-L)} \begin{pmatrix} \xi_{\alpha_i}^s \\ \xi_{\alpha_i}^{as} \end{pmatrix}. \quad (4.11)$$

The coefficients  $A, B, C$  and  $D$  are the functions of  $\omega$ , whereas  $P_{\alpha_i}, Q_{\alpha_i}$  are the functions of  $\omega$  and  $z$ .

## 4.4 Characteristics of generated photons

### 4.4.1 Stokes and Anti-Stokes photon generation rates

We evaluate the output generation rates of Stokes and anti-Stokes photons into a single transverse mode, for example, into a pair of mode-matched optical fibers. The generation rates at the corresponding boundaries  $z_j$  are

$$R_j = \frac{c}{L} \langle \hat{a}_j^\dagger(z_j, t) \hat{a}_j(z_j, t) \rangle, \quad (4.12)$$

where subscript  $j$  denotes either Stokes or anti-Stokes photon,  $z_s = L$  and  $z_{as} = 0$ .

Of importance are the spectral properties of the generated photons. The power spectrum of the output Stokes and anti-Stokes fields are related to their first order coherence functions  $G_j^{(1)}(\tau) = \langle a_j^\dagger(z_j, t) a_j(z_j, t + \tau) \rangle$  as

$$R_j(\omega) = \frac{c}{L} \int_{-\infty}^{+\infty} d\tau e^{i\omega\tau} G_j^{(1)}(\tau) \quad (4.13)$$

We use the solutions for  $a_s(L, \omega)$  and  $a_{as}^\dagger(0, -\omega)$  field operators, given by Eq. (4.9), the commutation relations for the input field operators  $[a_j(z_j, \omega), a_j^\dagger(z_j, -\omega')] = L/(2\pi c) \delta(\omega + \omega')$  and Eq. (4.41). We apply inverse Fourier transformation  $a(t) = \int d\omega e^{-i\omega t} a(\omega)$  and  $a^\dagger(t) = \int d\omega e^{-i\omega t} a^\dagger(-\omega)$  and obtain the Stokes and anti-Stokes generation rates from Eq. (4.12) in the form

$$R_s = \int \frac{d\omega}{2\pi} \left( |B|^2 + \sum_{\alpha_i, \alpha_j} \int_0^L dz P_{\alpha_i}^* \mathcal{D}_{\alpha_i, \alpha_j} P_{\alpha_j} \right) \quad (4.14)$$

$$R_{as} = \int \frac{d\omega}{2\pi} \left( |C|^2 + \sum_{\alpha_i, \alpha_j} \int_0^L dz Q_{\alpha_i} \mathcal{D}_{\alpha_i, \alpha_j} Q_{\alpha_j}^* \right) \quad (4.15)$$

The integrands of Eq. (4.14) and Eq. (4.15) are Stokes and anti-Stokes spectral generation rates respectively.

As seen from Eq. (4.14) and Eq. (4.15), Stokes and anti-Stokes spectral generation



rates consist of parametric counts, characterized by the transfer functions  $C(\omega)$  and  $B(\omega)$ , and of noise counts, that originate from Langevin noise fluctuations. If the pump is weak and far detuned,  $B(\omega) = -C(\omega)$ , and therefore the parametric terms in Stokes and anti-Stokes rates are equal. We also note that the contribution of Langevin noise fluctuations to spectral generation rates can not be neglected and becomes dominant at low optical depth of the atomic sample.

Using the commutator conservation relation for the Stokes field at the right boundary  $z = L$ , obtained from Eq. (4.9), the Stokes spectral generation rate can be expressed as

$$R_s(\omega) = |A|^2 - 1 + \sum_{\alpha_i, \alpha_j} \int_0^L dz P_{\alpha_i} \mathcal{D}_{\alpha_i, \alpha_j^\dagger} P_{\alpha_j}^* \quad (4.16)$$

When the pump is far detuned from the atomic transition and Stokes photon losses are small, the contribution of Langevin noise fluctuation in Eq. (4.16) is negligible. Thus, the Stokes spectral generation rate can be written as

$$R_s(\omega) \approx |A|^2 - 1 \quad (4.17)$$

Eq. (4.17) can be interpreted in terms of the quantum theory of linear amplification [47]: in the absence of the Stokes input beam and losses for the Stokes photon, the Stokes generation rate is just the additive noise caused by the amplification process, that is characterized by the gain coefficient  $A(\omega)$ .

#### 4.4.2 Two-photon intensity correlation function and biphoton wave-function

In order to address another important issue - the time correlation properties of the generated photons, we calculate the Glauber two-photon correlation function of time delay  $\tau$  between Stokes and anti-Stokes photons:

$$G_{s-as}^{(2)}(\tau) = \langle \hat{a}_s^\dagger(L, t) \hat{a}_{as}^\dagger(0, t + \tau) \hat{a}_{as}(0, t + \tau) \hat{a}_s(L, t) \rangle \quad (4.18)$$

Using the Stokes and anti-Stokes operators at the boundaries derived earlier [Eq. (4.9)] and the commutator relations for the input fields, we obtain the intensity correlation function as

$$G_{s-as}^{(2)}(\tau) = \iiint d\omega_1 d\omega_2 d\omega_3 d\omega_4 e^{-i\omega_1 t - i\omega_2(t+\tau) - i\omega_3(t+\tau) - i\omega_4 t} \times \langle \hat{a}_s^\dagger(L, -\omega_1) \hat{a}_{as}^\dagger(0, -\omega_2) \hat{a}_{as}(0, \omega_3) \hat{a}_s(L, \omega_4) \rangle \quad (4.19)$$

The intensity correlation function contains the fourth-order Langevin noise correlations. According to Gaussian moment theorem [48, 49] they can be decomposed preserving the order into the sum of the products of second order Langevin noise correlations. As a result the intensity correlation function can be simplified to

$$G_{s-as}^{(2)}(\tau) = \langle a_{as}^\dagger(0, t+\tau) a_{as}(0, t+\tau) \rangle \langle a_s^\dagger(L, t) a_s(L, t) \rangle + |\langle a_{as}(0, t+\tau) a_s(L, t) \rangle|^2 \\ = G_s^{(1)}(0) \times G_{as}^{(1)}(0) + |\Phi_{s-as}(\tau)|^2 \quad (4.20)$$

The first term in Eq. (4.20) represents flat uncorrelated background, the second term, expressed through  $\Phi_{s-as}(\tau)$  function, describes the correlation part.  $\Phi_{s-as}(\tau)$  is equal to

$$\Phi_{s-as}(\tau) = \langle \hat{a}_{as}(0, t+\tau) \hat{a}_s(L, t) \rangle \quad (4.21) \\ = \frac{L}{2\pi c} \int d\omega e^{i\omega\tau} \left( BD^* + \sum_{\alpha_i, \alpha_j} \int_0^L dz Q_{\alpha_i}^* \mathcal{D}_{\alpha_i^\dagger, \alpha_j} P_{\alpha_j} \right)$$

We note that  $e^{-i\omega_s t - i\omega_{as}(t+\tau)} \Phi_{s-as}(\tau)$  represents a two photon wavefunction or a biphoton wavefunction on the condition that peak value of normalized  $g_{s-as}^{(2)} \gg 1$ , where  $g_{s-as}^{(2)}(\tau) = G_{s-as}^{(2)}(\tau) / (G_s^{(1)}(0) \times G_{as}^{(1)}(0))$ .

Similarly, we can define  $\Phi_{as-s}(\tau) = \langle \hat{a}_s(L, t) \hat{a}_{as}(0, t+\tau) \rangle$ . This function can be

obtained in the form

$$\Phi_{as-s}(\tau) = \frac{L}{2\pi c} \int d\omega e^{i\omega\tau} \left( AC^* + \sum_{\alpha_i, \alpha_j} \int_0^L dz P_{\alpha_i} \mathcal{D}_{\alpha_i, \alpha_j^\dagger} Q_{\alpha_j}^* \right) \quad (4.22)$$

For a wide range of input parameters we numerically verify that  $\Phi_{as-s}(\tau) = \Phi_{s-as}(\tau)$ .

For the case where  $\Omega_p/\Delta\omega_{14} \ll 1$  and  $\Delta\omega_{14}/\gamma_{14} \gg 1$ , we numerically verify that the contribution of Langevin noise fluctuations to  $\Phi_{as-s}(\tau)$  is negligible, therefore Eq. (4.22) can be simplified to

$$\Phi_{as-s}(\tau) = \frac{L}{2\pi c} \int d\omega e^{i\omega\tau} AC^* \quad (4.23)$$

## 4.5 Ideal Spontaneous Parametric Down Converter

Before we proceed to the discussion of the interesting cases of the atomic correlation functions and photon spectral densities, we want to make an analogy to the well-known parametric down converter in crystals [40]. We consider the ideal model - non-degenerate parametric down converter in which a generated signal photon has a very slow group velocity  $V_g$  as compared to an idler photon. We assume that both idler and signal photon escape SPDC without losses, therefore the Langevin noise terms in Eq. (4.6) can be neglected. In crystals the coupling coefficient can be approximated as a constant over the broad spectral range  $\kappa_s(\omega) = \kappa_{as}(\omega) = \kappa$ . We also neglect Raman gain  $g_R(\omega)$  and approximate EIT profile as  $\Gamma(\omega) = -i\omega/V_g$ . Under these assumptions the signal and idler photons have identical spectral characteristics and rates. Using the Eq. (4.14), we obtain the photon spectral density  $R(\omega)$  and spectrally integrated generation rate  $R = 1/(2\pi) \int d\omega R(\omega)$  in the form:

$$R(\omega) = |\kappa|^2 L^2 \text{sinc}^2 \left( \frac{\omega L}{2V_g} \right) \quad (4.24)$$

$$R = V_g |\kappa|^2 L.$$

As seen from Eq. (4.24), the spectral bandwidth of the SPDC in crystals is limited by  $\Delta\omega \sim 2\pi V_g/L$  due to the phase mismatch of the off-centered counts resulting from the group delay in the signal channel. In principle, the bandwidth can be made very small by making the group delay  $\tau_g = L/V_g$  large. For the atomic system  $\kappa$  is proportional to the atomic density  $\mathcal{N} = N/V$ , therefore the spectral density of the generated photons scales as  $(\mathcal{N}L)^2$ . Taking into account that the EIT induced group velocity of a wave is  $V_g = \Omega_c^2/(2\gamma_{13}\mathcal{N}\sigma_{13})$ , where  $\sigma_{13} = \wp_{13}^2\omega_{13}/(c\epsilon_0\hbar\gamma_{13})$  is the atomic cross section of the  $|1\rangle \rightarrow |3\rangle$  transition, the total count rate scales linearly with  $\mathcal{N}L$ .

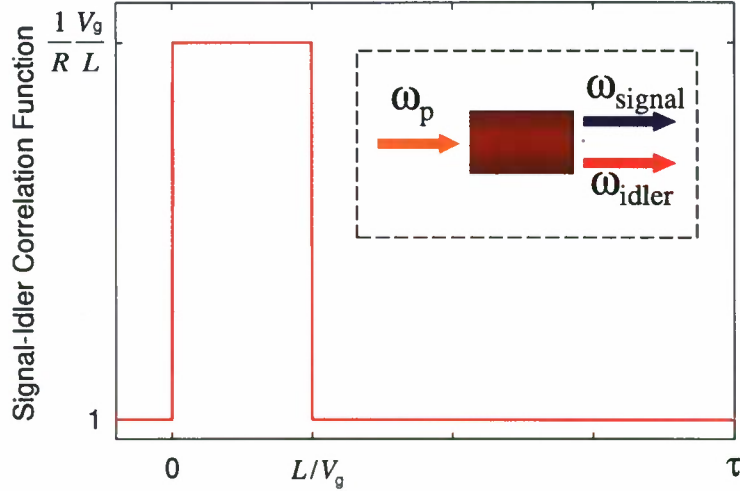


Figure 4.2: Normalized signal-idler intensity correlation function for the ideal SPDC with the condition of a large group delay  $L/V_g$  for a signal photon.  $R$  is the paired photon generation rate.

Fig. 4.2 shows the normalized signal idler intensity correlation function. Since the probability of emitting a photon pair is uniformly distributed along the crystal of length  $L$  and the signal photon has a group delay relative to the idler, the  $g_{s-i}^{(2)}(\tau)$

is expected to be the shifted rectangle with the width equal to the group delay  $\tau_g = L/V_g$ . By varying the group delay we can control the width of the waveform. The peak height of  $g_{s-i}^{(2)}$  is equal to  $1/(\kappa L)^2$  and can be interpreted as a duty ratio:  $g_{s-i}^{(2)} = 1/(R\tau_g)$ . In the regime of very small parametric gain  $\kappa L \ll 1$ , which can be achieved, for example, by lowering the intensity of the pump, the atomic system can produce highly correlated photon pairs  $g_{s-i}^{(2)} \gg 1$ .

## 4.6 EIT based Paired Photon Generator

Now we turn from the discussion of the ideal SPDC to the discussion of the EIT based paired photon generator. In the EIT based generator, coupling between Stokes and anti-Stokes modes is bandwidth limited. Moreover, the generated Stokes photon undergoes Raman gain  $g_R(\omega)$ , whereas a paired anti-Stokes photon propagates slowly and undergoes absorption at the poles of EIT profile  $\omega = \pm\Omega_c/2$ .

We first obtain the coefficients of Eq. (4.6) with the assumption that the pump is weak and far detuned from the  $|1\rangle \rightarrow |4\rangle$  transition and  $\Delta k = (\vec{k}_p + \vec{k}_c - \vec{k}_s - \vec{k}_{as}) \cdot \hat{z} = 0$ :



$$\Gamma_{as} = \frac{2i\mathcal{N}\sigma\gamma_{13}(\omega + i\gamma_{12})}{G(\omega)}, \quad (4.25a)$$

$$g_R = \left( \frac{\Omega_p^2}{2\Delta\omega_{14}^2} \right) \frac{i\mathcal{N}\sigma\gamma_{13}(\omega + i\gamma_{13})}{G(\omega)}, \quad (4.25b)$$

$$\kappa_s = \kappa_{as} = - \left( \frac{\Omega_p}{2\Delta\omega_{14}} \right) \frac{i\mathcal{N}\sigma\gamma_{13}\Omega_c}{G(\omega)}, \quad (4.25c)$$

$$\xi_{21}^s = - \left( \frac{\Omega_p}{\Delta\omega_{14}} \right) \frac{\sqrt{2}(\omega + i\gamma_{13})\sqrt{\mathcal{N}\sigma\gamma_{13}}}{G(\omega)}, \quad (4.25d)$$

$$\xi_{24}^s = - \frac{\sqrt{\mathcal{N}\sigma\gamma_{13}}}{\sqrt{2}\Delta\omega_{14}}, \quad (4.25e)$$

$$\xi_{31}^s = - \left( \frac{\Omega_p}{\Delta\omega_{14}} \right) \frac{\Omega_c\sqrt{\mathcal{N}\sigma\gamma_{13}}}{\sqrt{2}G(\omega)}, \quad (4.25f)$$

$$\xi_{34}^s = - \frac{\Omega_c\sqrt{\mathcal{N}\sigma\gamma_{13}}}{2\sqrt{2}\Delta\omega_{14}^2}, \quad (4.25g)$$

$$\xi_{21}^{as} = \frac{\sqrt{2}\Omega_c\sqrt{\mathcal{N}\sigma\gamma_{13}}}{G(\omega)}, \quad (4.25h)$$

$$\xi_{24}^{as} = - \left( \frac{\Omega_p}{\Delta\omega_{14}} \right) \frac{\Omega_c\sqrt{\mathcal{N}\sigma\gamma_{13}}}{\sqrt{2}G(\omega)}, \quad (4.25i)$$

$$\xi_{31}^{as} = \frac{2\sqrt{2}(\omega + i\gamma_{12})\sqrt{\mathcal{N}\sigma\gamma_{13}}}{G(\omega)}, \quad (4.25j)$$

$$\xi_{34}^{as} = - \left( \frac{\Omega_p}{\Delta\omega_{14}} \right) \frac{\sqrt{2}(\omega + i\gamma_{12})\sqrt{\mathcal{N}\sigma\gamma_{13}}}{G(\omega)}, \quad (4.25k)$$

where  $\mathcal{N}$  is an atom density,  $G(\omega) = |\Omega_c|^2 - 4(\omega + i\gamma_{12})(\omega + i\gamma_{13})$ ,  $\sigma$  is the absorption cross section for all allowed transitions:  $\sigma = \sigma_{14} = \sigma_{24} = \sigma_{23} = \sigma_{13}$ .

### 4.6.1 Ground state approximation

The approximation that the atomic population remains in the ground state  $\tilde{\sigma}_{11} = 1$  gives two significant diffusion coefficients  $\mathcal{D}_{12,21} = 2\gamma_{12}$  and  $\mathcal{D}_{13,31} = \Gamma_3$  corresponding to  $F_{21}, F_{31}$  Langevin noise operators. Due to small atomic population in the excited states, the rest of the diffusion coefficients are approximated as zeros and the corresponding Langevin noise operators are neglected [36].

We numerically examine the emission rates and intensity correlation function for the EIT based paired photon emitter. We take other parameters similar to those of a Rb MOT: atom density  $\mathcal{N} = 10^{11}$  atoms per  $\text{cm}^3$ , atomic cross sections  $\sigma = \sigma_{13} = \sigma_{14} = \sigma_{24} = 10^{-9} \text{ cm}^2$  and dephasing rates equal to one half of the Einstein A coefficient, i.e.,  $\gamma_{13} = \gamma_{14} = \gamma_{24} = \gamma_{23} = 1.79 \times 10^7$  radians. We choose the strength and the detuning of the pump laser from the  $|1\rangle \rightarrow |4\rangle$  transition as  $\Delta\omega_{14} = 24\gamma_{13}$  and  $\Omega_p/\Delta\omega_{14} = 0.1$ .

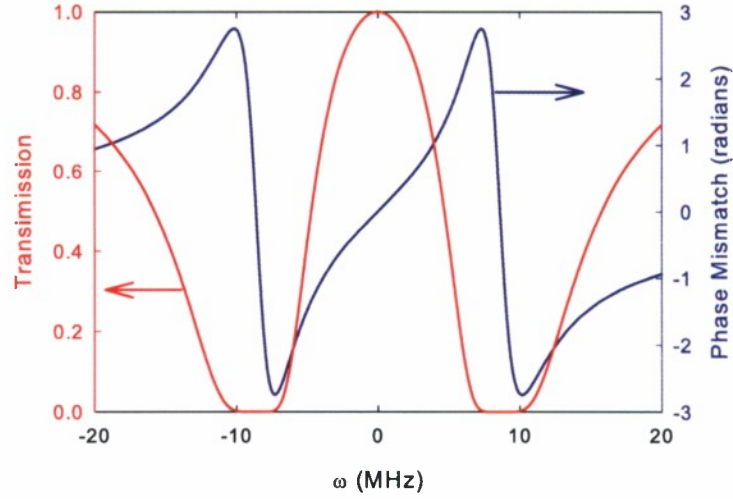


Figure 4.3: Transmission and phase mismatch as functions of detuning  $\omega$

Fig. 4.3 shows the EIT transmission profile and phase mismatch as a function of the detuning of the anti-Stokes frequency  $\omega$ . We take  $\Omega_c = 6\gamma_{13}$ ,  $\mathcal{N}\sigma L = 11$  and  $\gamma_{12} = 0$ . Fig. 4.4 shows the profiles of the coupling coefficient  $|\kappa(\omega)|$  and the Raman

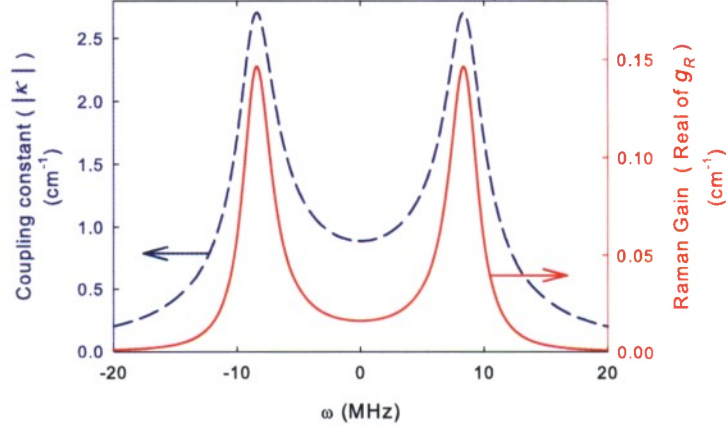


Figure 4.4: Coupling constant and Raman gain as functions of detuning  $\omega$ .

gain coefficient  $Re(g_R(\omega))$  for the same parameters as in Fig. 4.3.

EIT based spontaneous emitters allow a variable emission bandwidth. The bandwidth and profile of the spontaneous emission rates are controlled by the strength of the coupling laser  $\Omega_c$  and the optical depth of the atomic sample  $\mathcal{N}\sigma L$ . By reducing the strength of the coupling laser, the emission linewidth can be made much smaller than the natural linewidth, with the minimum width ultimately limited by the dephasing rate  $\gamma_{12}$  of the  $|1\rangle \rightarrow |2\rangle$  transition. At small optical depth  $\mathcal{N}\sigma L < 1$ , the Raman gain coefficient  $g_R(\omega)$  and the coupling coefficients  $\kappa_s(\omega)$ ,  $\kappa_{as}(\omega)$  determine the emission spectrum. At high optical depth  $\mathcal{N}\sigma L > 1$ , the EIT transmission window and the phase mismatch, introduced by a large group delay in the anti-Stokes channel, affect the spontaneous emission spectrum.

In Fig. 4.5, Fig. 4.6 and Fig. 4.7 we show the variations of the coincidence count rate  $R_c(\tau)$  in a 1 ns bin and the corresponding Stokes power spectral density depending on the optical depth. With a bin size  $\Delta T = 1$  ns much smaller than the correlation time, the coincidence count rate is obtained from the intensity correlation function as  $R_c(\tau) = \Delta T (c/L)^2 G_{as-s}^{(2)}(\tau)$ . Compared to the ideal case, described earlier, the intensity correlation function and the emission spectrum for the EIT based atomic SPDC show some interesting features. The shape of the intensity correlation function

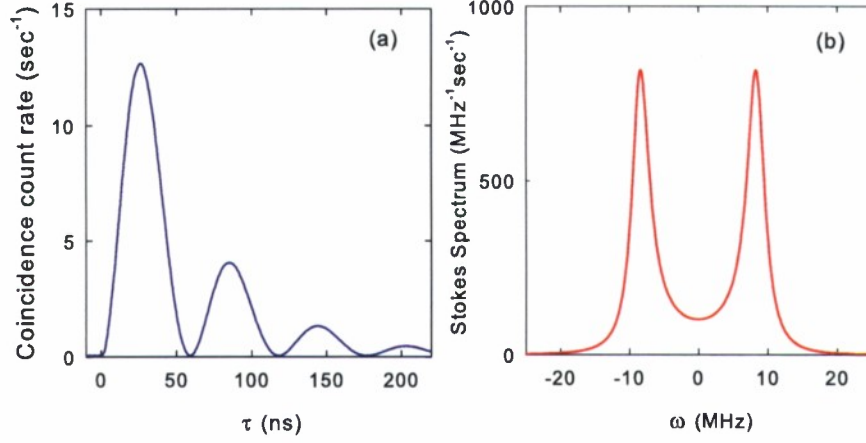


Figure 4.5: The oscillatory regime: (a) Coincidence count rate in a 1 ns bin and (b) Stokes spectral generation rate.  $\mathcal{N}\sigma L = 0.3$ ,  $\Omega_c = 6\gamma_{13}$  and  $\gamma_{12} = 0$ .

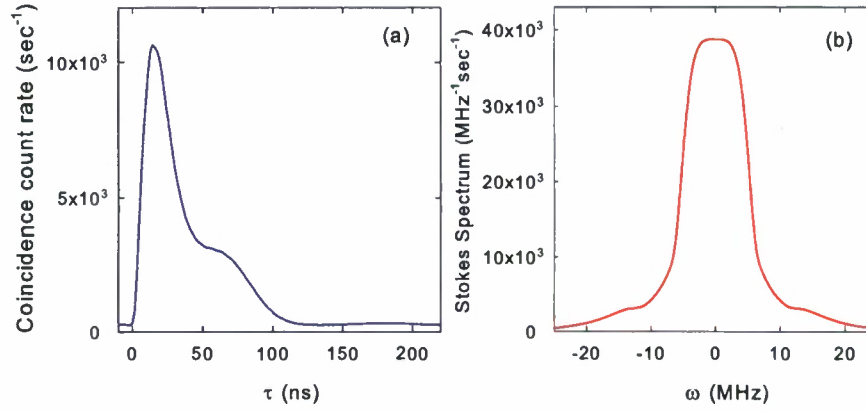


Figure 4.6: The group delay regime: (a) Coincidence count rate in a 1 ns bin and (b) Stokes spectral generation rate.  $\mathcal{N}\sigma L = 20$ ,  $\Omega_c = 6\gamma_{13}$  and  $\gamma_{12} = 0$ .

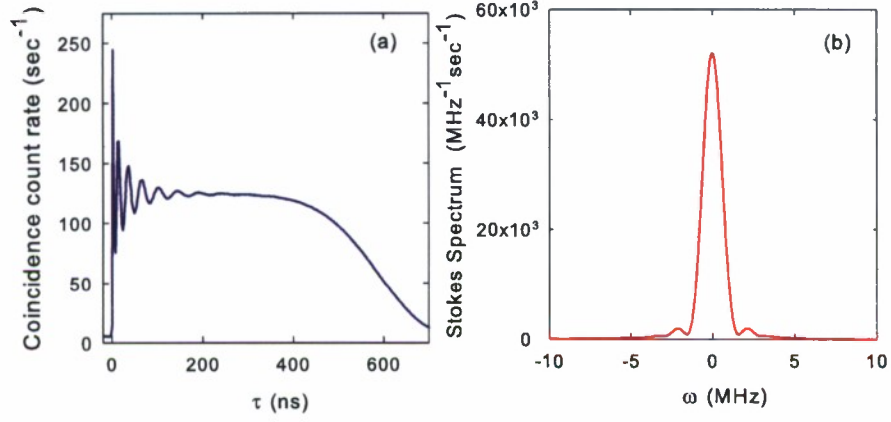


Figure 4.7: The group delay regime: (a) Coincidence count rate in a 1 ns bin and (b) Stokes spectral generation rate.  $\mathcal{N}\sigma L = 200$ ,  $\Omega_c = 6\gamma_{13}$ ,  $\Omega_p = 0.3\gamma_{13}$  and  $\gamma_{12} = 0$ .

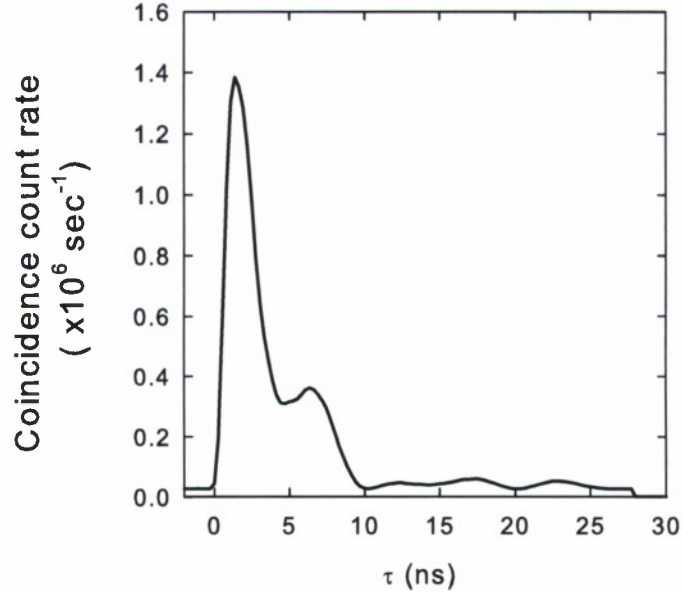


Figure 4.8: Intensity correlation function with the correlation time smaller than the spontaneous decay time,  $\tau_r < \tau_g < 1/(2\gamma_{13})$ .  $\mathcal{N}\sigma L = 200$ ,  $\Omega_c = 65\gamma_{13}$ ,  $\gamma_{12} = 0$  and  $1/(2\gamma_{13}) = 25$  ns.



and the emission profile depend on the relation of three characteristic times. The first is the inverse Rabi frequency of the coupling laser  $\tau_r = 2\pi/\sqrt{\Omega_c^2 - \gamma_{13}^2}$ , the second is the group delay between Stokes and anti-Stokes photons  $\tau_g = L/V_g = 2\gamma_{13}\mathcal{N}\sigma L/\Omega_c^2$  and the third is a minimal pulse length required to pass through EIT medium [50]  $\tau_{p(min)} = 8\ln(2)\gamma_{13}\sqrt{\mathcal{N}\sigma L}/\Omega_c^2$ .

When the EIT effect is small, which occurs, for example, at low optical depth, the atomic system behaves like a single atom [51]. In such a regime the intensity correlation function reveals the damped Rabi oscillations (Fig. 4.5). The oscillations observed in the intensity correlation function have the time period of  $\tau_r = 2\pi/\sqrt{\Omega_c^2 - \gamma_{13}^2}$  and occur on the condition that  $\tau_r > \tau_g, \tau_{p(min)}$  and the coupling laser is strong enough to force the oscillations to overcome damping  $\Omega_c > \gamma_{13}$ . Once the metastable state  $|2\rangle$  is excited by the Raman process  $|1\rangle \rightarrow |4\rangle \rightarrow |2\rangle$ , the probability amplitude between  $|2\rangle$  and  $|3\rangle$  oscillates due to the strong interaction of the atoms with the resonant coupling beam.

In Fig. 4.6 we show the intensity correlation function and Stokes emission spectrum in the group delay regime, where  $\tau_g > \tau_r$  and  $\tau_g > \tau_{p(min)}$ . In this regime the width of the intensity correlation function is approximated by  $\tau_g$ . Moreover, the frequency range over which the spontaneous generation occurs is filtered by the EIT window and mostly controlled by the phase-matching in the presence of large group delay in the anti-Stokes channel. A sufficiently wide EIT window  $\tau_g > \tau_{p(min)}$  requires high optical depth  $\mathcal{N}\sigma L > 10$ . In the presence of the non-zero dephasing  $\gamma_{12}$ , the maximum group delay and therefore the maximum width of the correlation function is limited by  $\sim 1/\gamma_{12}$ .

By increasing the optical depth of the atomic sample, the EIT window can be made substantially larger than the emission bandwidth. A large EIT window might be very useful for such applications as bi-photon waveform control and shaping. Fig. 4.7 shows the intensity correlation function and the Stokes emission spectrum under such a condition, where  $\mathcal{N}\sigma L = 200$ . The tail of the correlation function decays on the time scale of  $\tau_{p(min)}$ .

We also note that at high optical depth it becomes possible to achieve the Stokes–anti-Stokes correlation function with the width shorter than the spontaneous decay

time  $1/(2\gamma_{13})$ . Fig. 4.8 shows such a correlation function that is obtained for  $N\sigma L = 200$  and  $\Omega_c = 65\gamma_{13}$ , where  $\tau_r < \tau_g < 1/(2\gamma_{13})$ .

We turn next to the sharp peak at the leading edge of the correlation function of Fig. 4.7. This sharp peak is Sommerfeld-Brillouin precursor [52]. It has been observed in our theoretical plots for a long time. But only recently, when it was experimentally measured, we got interested in its nature. We thank Daniel J. Gauthier who suggested that this peak is the result of simultaneously generated Stokes and anti-Stokes photons that travel at nearly the speed of light in vacuum and arrive near-simultaneously at the photodetectors. He also pointed out to the similarity of this peak to precursors which have been extensively studied [52, 53, 54]. A precursor has an approximate width that is equal to the opacity width of the atomic transition in the optically thick medium. Similar to precursors, the sharp leading edge peak has a opacity width of the EIT profile [55].

#### 4.6.2 No ground state approximation

If the pump is weak and far detuned and therefore most of the atomic population is in the ground state, we verify that the ground state approximation gives a correct prediction for the Bi-photon function and the Stokes generation rate. Nevertheless it does not properly account for an atom return to the ground state  $|1\rangle$ . Ideally one would expect the Stokes and anti-Stokes rates to be equal, since an atom, making a complete cycle on the energy level diagram (Fig. 5.7), returns to the ground state. Even at zero dephasing rate  $\gamma_{12} = 0$  of the  $|1\rangle \rightarrow |2\rangle$  transition, the ground state approximation predicts the anti-Stokes generation rate to be smaller than the Stokes generation rate. For example,  $R_{as}/R_s = 0.65$  for  $N\sigma L = 10$ ,  $\Omega_p/\Delta\omega_{14} = 0.1$  and  $\Omega_c = 6\gamma_{13}$ .

In order to treat properly an atom's return to the ground state we will retain in Eq. (4.6) all four Langevin noise operators  $\{\tilde{f}_{21}, \tilde{f}_{24}, \tilde{f}_{31}, \tilde{f}_{34}\}$  and take into account small incoherent population in excited states, resulting from the steady state solutions of Eqs. (4.27a)-(4.27f). With these inclusions the solution of Eq. (4.6) predicts the Stokes and anti-Stokes spectral generation rates to be equal at a zero dephasing rate

$\gamma_{12} = 0$  [Fig. 4.9(a)]. A non-zero dephasing rate  $\gamma_{12} \neq 0$  reduces EIT and therefore introduces additional losses for anti-Stokes photons. As a result the output Stokes rate exceeds the anti-Stokes rate. For example, for  $\mathcal{N}\sigma L = 10$ ,  $\Omega_p/\Delta\omega_{14} = 0.1$ ,  $\Omega_c = 6\gamma_{13}$  and  $\gamma_{12} = 0.6\gamma_{13}$  we obtain  $R_{as}/R_s \approx 0.8$ . The corresponding Stokes and anti-Stokes spectral generation rates are shown in Fig. 4.9(b). We believe that the “missing” anti-Stokes photons are absorbed and are then reemitted in a solid angle of  $4\pi$ . The atomic sample is assumed to be optically thin in the radial direction.

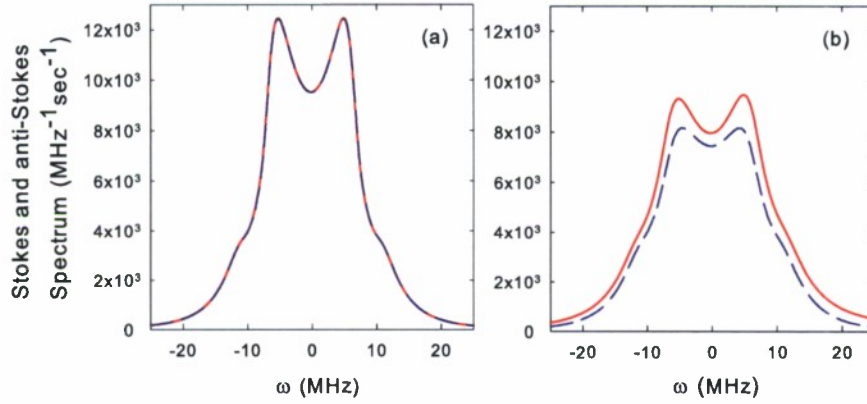


Figure 4.9: Stokes (solid curve) and anti-Stokes (dash curve) spectral generation rates at (a) zero dephasing  $\gamma_{12} = 0$  and (b) non zero dephasing  $\gamma_{12} = 0.6\gamma_{13}$ .  $\mathcal{N}\sigma L = 10$ ,  $\Omega_c = 6\gamma_{13}$   $\Omega_p = 2.4\gamma_{13}$ ,  $\Delta\omega_{14} = 24\gamma_{13}$

Compared to the ideal SPDC, where each generated signal photon has its paired idler photon, the real atomic system has uncorrelated noise counts in both Stokes and anti-Stokes channels that result from Langevin noise fluctuations. In Fig. 4.10 we examine the dependence of the Stokes (anti-Stokes) and paired count rates on the optical depth  $\mathcal{N}\sigma L$ . The parameters for the curves are  $\gamma_{12} = 0$ ,  $\Omega_c = 5\gamma_{13}$ ,  $\Delta\omega_{14} = 24\gamma_{13}$  and  $\Omega_p/\Delta\omega_{14} = 0.1$ . The paired count rate ( $R_p$ ) is defined as the area under the Stokes–anti-Stokes coincidence count rate function minus the area under the uncorrelated background. One may show that  $R_p \approx 1/(2\pi) \int d\omega |AC^*|^2$ . At small optical depth the paired rate scales quadratically with the optical depth and is much smaller than the Stokes rate. At high optical depth the paired rate varies linearly

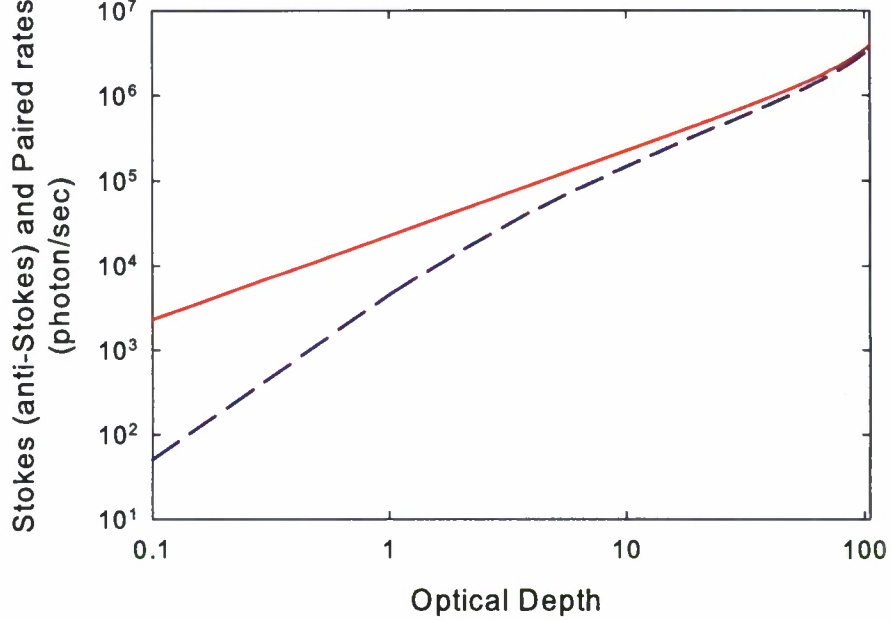


Figure 4.10: Stokes, anti-Stokes (solid curve) and Paired (dashed curve) photon generation rates as a function of the optical depth.  $\Omega_c = 5\gamma_{13}$ ,  $\gamma_{12} = 0$ ,  $\Delta\omega_{14} = 24\gamma_{13}$  and  $\Omega_p/\Delta\omega_{14} = 0.1$ . At optical depth of 100, the paired rate reaches 90% of the Stokes rate.

with  $\mathcal{N}\sigma L$  and converges logarithmically to the Stokes emission rate.

In this chapter we describe the theory of paired photon generation in double- $\Lambda$  atomic system. With low parametric gain and high optical depth we show that the system can produce highly correlated photon pairs. The shape of the intensity correlation function and the emission bandwidth depend on the coupling laser Rabi frequency and the optical depth of the atomic sample. Compared to the ideal SPDC, paired photon generation in the double- $\Lambda$  atomic system is affected by Raman gain in the Stokes channel and EIT in the anti-Stokes channel. EIT, through the absorption at the poles, cuts the emission bandwidth. In order to enter a regime where the EIT

window is sufficiently large and therefore the emission bandwidth is controlled to a large extent by the phase-matching process in the presence of large group delay, the optical depth of the atomic sample has to be large  $\mathcal{N}\sigma L > 10$ . High optical depth substantially reduces the influence of Langevin noise fluctuations on paired photon generation so that the Stokes and anti-Stokes photons are generated mostly in pairs. We therefore suggest the use of a cigar shaped atomic cloud with high optical depth in the longitudinal direction.

## 4.7 Mathematical Apparatus

### 4.7.1 Collective slowly varying atomic operators

To describe the quantum properties of the atomic system we use the collective slowly varying atomic operators [56, 57, 58, 46, 59]  $\hat{\sigma}_{jk}(z, t)$ , defined as

$$\tilde{\sigma}_{jk}(z, t) = \frac{1}{N_z} \sum_{i \in N_z} |j\rangle_i \langle k| \exp(-i\nu_{jk}t + ik_{jk}z), \quad (4.26)$$

where the averaging is done over each atom  $i$  in a small interval  $\Delta z$  that contains large number of atoms  $N_z \gg 1$ . The slowly varying variables are assumed to stay unchanged over  $\Delta z$ .  $\nu_{41} = \omega_4 - \omega_1 + \Delta\omega_{14}$ ,  $\nu_{42} = \omega_4 - \omega_2 + \Delta\omega_{14}$ ,  $\nu_{14} = -\nu_{41}$ ,  $\nu_{24} = -\nu_{42}$ , the rest of  $\nu_{jk} = \omega_j - \omega_k$ .  $k_{31} = \vec{k}_{as} \cdot \hat{z}$ ,  $k_{42} = \vec{k}_s \cdot \hat{z}$ ,  $k_{41} = \vec{k}_p \cdot \hat{z}$ ,  $k_{32} = \vec{k}_c \cdot \hat{z}$  are the projections of the anti-Stokes, Stokes, pump and coupling  $k$ -vectors on the  $z$  axis,  $k_{43} = k_{41} - k_{31}$ ,  $k_{21} = -k_{24} + k_{41}$ , the rest of  $k_{jk} = -k_{kj}$ .

### 4.7.2 Heisenberg-Langevin equations

The full set of Heisenberg-Langevin equations for the four state system consists of 16 equations. Here, we show explicitly 10 of them, the other 6 for the adjoint off-diagonal



atomic operators are not shown.

$$\begin{aligned} \frac{\partial}{\partial t} \tilde{\sigma}_{44} &= \tilde{F}_{44} - \Gamma_4 \tilde{\sigma}_{44} \\ &+ i \left( \frac{\Omega_p}{2} \tilde{\sigma}_{41} + g_s \hat{a}_s \tilde{\sigma}_{42} - g_s \hat{a}_s^\dagger \tilde{\sigma}_{24} - \frac{\Omega_p^*}{2} \tilde{\sigma}_{14} \right) \end{aligned} \quad (4.27a)$$

$$\begin{aligned} \frac{\partial}{\partial t} \tilde{\sigma}_{41} &= \tilde{F}_{41} - (\gamma_{41} + i\Delta\omega_{14}) \tilde{\sigma}_{41} \\ &+ i \left( -g_{as} \hat{a}_{as}^\dagger \tilde{\sigma}_{43} + g_s \hat{a}_s^\dagger \tilde{\sigma}_{21} + \frac{\Omega_p^*}{2} (\tilde{\sigma}_{11} - \tilde{\sigma}_{44}) \right) \end{aligned} \quad (4.27b)$$

$$\begin{aligned} \frac{\partial}{\partial t} \tilde{\sigma}_{33} &= \tilde{F}_{33} - \Gamma_3 \tilde{\sigma}_{33} \\ &+ i \left( g_{as} \hat{a}_{as} \tilde{\sigma}_{31} + \frac{\Omega_c}{2} \tilde{\sigma}_{32} - g_{as} \hat{a}_{as}^\dagger \tilde{\sigma}_{13} - \frac{\Omega_c^*}{2} \tilde{\sigma}_{23} \right) \end{aligned} \quad (4.27c)$$

$$\begin{aligned} \frac{\partial}{\partial t} \tilde{\sigma}_{32} &= \tilde{F}_{32} - \gamma_{32} \tilde{\sigma}_{32} \\ &+ i \left( -g_{as} \hat{a}_{as}^\dagger \tilde{\sigma}_{12} + g_s \hat{a}_s^\dagger \tilde{\sigma}_{34} + \frac{\Omega_c^*}{2} (\tilde{\sigma}_{33} - \tilde{\sigma}_{22}) \right) \end{aligned} \quad (4.27d)$$

$$\begin{aligned} \frac{\partial}{\partial t} \tilde{\sigma}_{22} &= \tilde{F}_{22} + \Gamma_{32} \tilde{\sigma}_{33} + \Gamma_{42} \tilde{\sigma}_{44} \\ &+ i \left( -\frac{\Omega_c}{2} \tilde{\sigma}_{32} - g_s \hat{a}_s \tilde{\sigma}_{42} + g_s \hat{a}_s^\dagger \tilde{\sigma}_{24} + \frac{\Omega_c^*}{2} \tilde{\sigma}_{23} \right) \end{aligned} \quad (4.27e)$$

$$\begin{aligned} \frac{\partial}{\partial t} \tilde{\sigma}_{11} &= \tilde{F}_{11} + \Gamma_{31} \tilde{\sigma}_{33} + \Gamma_{41} \tilde{\sigma}_{44} \\ &+ i \left( -g_{as} \hat{a}_{as} \tilde{\sigma}_{31} - \frac{\Omega_p}{2} \tilde{\sigma}_{41} + g_{as} \hat{a}_{as}^\dagger \tilde{\sigma}_{13} + \frac{\Omega_p^*}{2} \tilde{\sigma}_{14} \right) \end{aligned} \quad (4.27f)$$

$$\begin{aligned} \frac{\partial}{\partial t} \tilde{\sigma}_{34} = & \tilde{F}_{34} - (\gamma_{34} - i\Delta\omega_{14}) \tilde{\sigma}_{34} \\ & + i \left( \frac{\Omega_p}{2} \tilde{\sigma}_{31} + g_s \hat{a}_s \tilde{\sigma}_{32} - g_{as} \hat{a}_{as}^\dagger \tilde{\sigma}_{14} - \frac{\Omega_c^*}{2} \tilde{\sigma}_{24} \right) \end{aligned} \quad (4.28a)$$

$$\begin{aligned} \frac{\partial}{\partial t} \tilde{\sigma}_{31} = & \tilde{F}_{31} - \gamma_{31} \tilde{\sigma}_{31} \\ & + i \left( g_{as} \hat{a}_{as}^\dagger (\tilde{\sigma}_{33} - \tilde{\sigma}_{11}) - \frac{\Omega_c^*}{2} \tilde{\sigma}_{21} + \frac{\Omega_p^*}{2} \tilde{\sigma}_{34} \right) \end{aligned} \quad (4.28b)$$

$$\begin{aligned} \frac{\partial}{\partial t} \tilde{\sigma}_{24} = & \tilde{F}_{24} - (\gamma_{24} - i\Delta\omega_{14}) \tilde{\sigma}_{24} \\ & + i \left( \frac{\Omega_p}{2} \tilde{\sigma}_{21} - \frac{\Omega_c}{2} \tilde{\sigma}_{34} + g_s \hat{a}_s (\tilde{\sigma}_{22} - \tilde{\sigma}_{44}) \right) \end{aligned} \quad (4.28c)$$

$$\begin{aligned} \frac{\partial}{\partial t} \tilde{\sigma}_{21} = & \tilde{F}_{21} - \gamma_{21} \tilde{\sigma}_{21} \\ & + i \left( -\frac{\Omega_c}{2} \tilde{\sigma}_{31} - g_s \hat{a}_s \tilde{\sigma}_{41} + g_{as} \hat{a}_{as}^\dagger \tilde{\sigma}_{23} + \frac{\Omega_p^*}{2} \tilde{\sigma}_{24} \right) \end{aligned} \quad (4.28d)$$

Here, for simplicity, we assume that  $\Delta k = (\vec{k}_p + \vec{k}_c - \vec{k}_s - \vec{k}_{as}) \cdot \hat{z} = 0$ . In Eq. (4.27a)-Eq. (4.28d)  $\Gamma_i$  is the total decay rate from state  $|i\rangle$ ,  $\Gamma_{ij}$  is the decay rate from state  $|i\rangle$  to state  $|j\rangle$  and  $\gamma_{ij}$  is the dephasing rate between state  $|i\rangle$  and state  $|j\rangle$ . The dephasing rates for the double- $\Lambda$  system in the absence of the collisional dephasing can be obtained from total decay rates  $\Gamma_3$  and  $\Gamma_4$  from state  $|3\rangle$  and  $|4\rangle$  to two ground states  $|1\rangle$  and  $|2\rangle$  as

$$\gamma_{31} = \gamma_{32} = \frac{\Gamma_3}{2} \quad (4.29)$$

$$\gamma_{41} = \gamma_{42} = \frac{\Gamma_4}{2} \quad (4.30)$$

$$\gamma_{43} = \frac{\Gamma_3 + \Gamma_4}{2} \quad (4.31)$$

### 4.7.3 Linearization procedure

In zeroth order perturbation expansion, in which  $\hat{a}_s$  and  $\hat{a}_{as}$  go to zero, the Heisenberg-Langevin equations for  $\tilde{\sigma}_{11}, \tilde{\sigma}_{14}, \tilde{\sigma}_{22}, \tilde{\sigma}_{23}, \tilde{\sigma}_{32}, \tilde{\sigma}_{33}, \tilde{\sigma}_{41}, \tilde{\sigma}_{44}$  atomic operators are decoupled. Under the assumption that pump and coupling beams propagate without depletion, we obtain the steady state solution for Eqs. (4.27a)-(4.27f) in form

$$\tilde{\sigma}_{jk}^0 = \langle \tilde{\sigma}_{jk}^0 \rangle + \sum \epsilon_{mn} \tilde{F}_{mn} \quad (4.32)$$

With the definition of the denominator as

$$T = \Gamma_{31} (\Gamma_4^2 + 4\Delta\omega_{14}^2 + 2|\Omega_p|^2) |\Omega_c|^2 + \Gamma_{42} (\Gamma_3^2 + 2|\Omega_c|^2) |\Omega_p|^2, \quad (4.33)$$

the steady state expectation values for the zeroth order atomic operators are equal to

$$\langle \tilde{\sigma}_{11}^0 \rangle = \frac{\Gamma_{31} |\Omega_c|^2 (\Gamma_4^2 + 4\Delta\omega_{14}^2 + |\Omega_p|^2)}{T} \quad (4.34a)$$

$$\langle \tilde{\sigma}_{22}^0 \rangle = \frac{\Gamma_{42} (\Gamma_3^2 + |\Omega_c|^2) |\Omega_p|^2}{T} \quad (4.34b)$$

$$\langle \tilde{\sigma}_{33}^0 \rangle = \frac{\Gamma_{42} |\Omega_c \Omega_p|^2}{T} \quad (4.34c)$$

$$\langle \tilde{\sigma}_{44}^0 \rangle = \frac{\Gamma_{31} |\Omega_c \Omega_p|^2}{T} \quad (4.34d)$$

$$\langle \tilde{\sigma}_{14}^0 \rangle = -\frac{\Gamma_{31} (2\Delta\omega_{14} - i\Gamma_4) |\Omega_c|^2 \Omega_p}{T} \quad (4.34e)$$

$$\langle \tilde{\sigma}_{23}^0 \rangle = \frac{i\Gamma_3 \Gamma_{42} \Omega_c |\Omega_p|^2}{T}, \quad (4.34f)$$

In the first order expansion, we substitute the zeroth order solution for the atomic operators Eq. (4.32) into the remaining Heisenberg-Langevin equations for  $\tilde{\sigma}_{21}, \tilde{\sigma}_{24}, \tilde{\sigma}_{31}, \tilde{\sigma}_{34}$  and their adjoint. Neglecting higher order terms like  $\epsilon_{mn} \tilde{F}_{mn} \hat{a}_s$  or  $\epsilon_{mn} \tilde{F}_{mn} \hat{a}_{as}^\dagger$  we obtain the linearized equations. We note that the linearized Eqs.(4.28a)-(4.28d) for  $\tilde{\sigma}_{21}, \tilde{\sigma}_{24}, \tilde{\sigma}_{31}, \tilde{\sigma}_{34}$  represent an independent set of equations and can be decoupled.

For clarity we write them in vector form

$$\frac{\partial}{\partial t} \tilde{\sigma}_1 = \mathcal{A} \tilde{\sigma}_1 + \mathcal{M} \hat{\mathbf{a}} + \tilde{\mathbf{F}}_1 \quad (4.35)$$

where  $\tilde{\sigma}_1 = \{\tilde{\sigma}_{21}, \tilde{\sigma}_{24}, \tilde{\sigma}_{31}, \tilde{\sigma}_{34}\}$ ,  $\tilde{\mathbf{F}}_1 = \{\tilde{F}_{21}, \tilde{F}_{24}, \tilde{F}_{31}, \tilde{F}_{34}\}$ ,  $\hat{\mathbf{a}} = \{\hat{a}_s, \hat{a}_{as}^\dagger\}$ , matrix  $\mathcal{A}$  depends on the dephasing rates  $\gamma_{jk}$  and pump and coupling laser rabi frequencies  $\Omega_p, \Omega_c$ , matrix  $\mathcal{M}$  depends on the zeroth order solution for the atomic operators  $\langle \tilde{\sigma}_{jk}^0 \rangle$ .

#### 4.7.4 Langevin noise operators and their diffusion coefficients

By analogy with the collective slowly varying atomic operators  $\tilde{\sigma}_{jk}(z, t)$ , the collective Langevin noise operators are defined as

$$\tilde{F}_{jk}(z, t) = \frac{1}{N_z} \sum_{z_i \in N_z} \tilde{F}_{jk}^{(i)}(t) \quad (4.36)$$

We assume that a Langevin noise operator for a single atom is  $\delta$ -correlated so that

$$\langle \tilde{F}_{jk}^{(i)}(t) \tilde{F}_{j'k'}^{(j)}(t') \rangle = \mathcal{D}_{jk,j'k'}^{(i)}(t) \delta(t - t') \delta_{ij} \quad (4.37)$$

where  $\langle \dots \rangle$  denotes the average over the reservoir,  $\mathcal{D}_{jk,j'k'}^{(i)}(t)$  is the atomic diffusion coefficient for an  $i_{th}$  atom.

Now we consider the second order correlations for the collective Langevin noise operators

$$\langle \tilde{F}_{jk}(t, z) \tilde{F}_{j'k'}(t', z') \rangle = \frac{1}{N_z^2} \sum_{z_i \in N_z} \langle \tilde{F}_{jk}^{(i)}(t) \tilde{F}_{j'k'}^{(i)}(t') \rangle \delta_{zz'} \quad (4.38)$$

Introducing the average atomic diffusion coefficient

$$\mathcal{D}_{jk,j'k'}(t, z) = \frac{1}{N_z} \sum_{z_i \in N_z} \mathcal{D}_{jk,j'k'}^{(i)}(t) \quad (4.39)$$

the noise correlations can be expressed as

$$\langle \tilde{F}_{jk}(t, z) \tilde{F}_{j'k'}(t', z') \rangle = \frac{L}{N} \mathcal{D}_{jk,j'k'}(t, z) \delta(t - t') \delta(z - z') \quad (4.40)$$

In case  $\mathcal{D}_{jk,j'k'}(t, z)$  is independent of  $t$ , in frequency domain the noise correlations are

$$\langle \tilde{F}_{jk}(\omega, z) \tilde{F}_{j'k'}(\omega', z') \rangle = \frac{L}{2\pi N} \mathcal{D}_{jk,j'k'} \delta(\omega + \omega') \delta(z - z') \quad (4.41)$$

The diffusion coefficients  $\mathcal{D}_{jk,j'k'}$  can be obtained from the Heisenberg-Langevin equations (4.27a)-(4.28d) using the generalized fluctuation-dissipation theorem [60, 61]. Here we show the diffusion coefficients for the Langevin noise operators of interest  $\tilde{F}_{21}, \tilde{F}_{24}, \tilde{F}_{31}, \tilde{F}_{34}$  and their adjoint  $\tilde{F}_{12}, \tilde{F}_{42}, \tilde{F}_{13}, \tilde{F}_{43}$

$$\mathcal{D}_{\alpha_i, \alpha_j^\dagger} = \begin{pmatrix} 2 \langle \tilde{\sigma}_{22} \rangle \gamma_{12} + \langle \tilde{\sigma}_{33} \rangle \Gamma_{32} + \langle \tilde{\sigma}_{44} \rangle \Gamma_{42} & 0 & \langle \tilde{\sigma}_{23} \rangle \gamma_{12} & 0 \\ 0 & \langle \tilde{\sigma}_{22} \rangle \Gamma_4 + \langle \tilde{\sigma}_{33} \rangle \Gamma_{32} + \langle \tilde{\sigma}_{44} \rangle \Gamma_{42} & 0 & \langle \tilde{\sigma}_{23} \rangle \Gamma_4 \\ \langle \tilde{\sigma}_{32} \rangle \gamma_{12} & 0 & 0 & 0 \\ 0 & \langle \tilde{\sigma}_{32} \rangle \Gamma_4 & 0 & \langle \tilde{\sigma}_{33} \rangle \Gamma_4 \end{pmatrix}, \quad (4.42)$$

$$\mathcal{D}_{\alpha_i^\dagger, \alpha_j} = \begin{pmatrix} 2 \langle \tilde{\sigma}_{11} \rangle \gamma_{12} + \langle \tilde{\sigma}_{33} \rangle \Gamma_{31} + \langle \tilde{\sigma}_{44} \rangle \Gamma_{41} & \langle \tilde{\sigma}_{14} \rangle \gamma_{12} & 0 & 0 \\ \langle \tilde{\sigma}_{41} \rangle \gamma_{12} & 0 & 0 & 0 \\ 0 & 0 & \langle \tilde{\sigma}_{11} \rangle \Gamma_3 + \langle \tilde{\sigma}_{33} \rangle \Gamma_{31} + \langle \tilde{\sigma}_{44} \rangle \Gamma_{41} & \langle \tilde{\sigma}_{14} \rangle \Gamma_3 \\ 0 & 0 & \langle \tilde{\sigma}_{41} \rangle \Gamma_3 & \langle \tilde{\sigma}_{44} \rangle \Gamma_3 \end{pmatrix}, \quad (4.43)$$

where  $\alpha_i$  denotes  $\{21, 24, 31, 34\}$  subspace for the atomic operators,  $\alpha_i^\dagger$  denotes  $\{12, 42, 13, 43\}$  subspace for the adjoint atomic operators.